

Electrolyte development based on ionic liquids for Eco-friendly Sodium ion battery

Submitted in partial fulfillment of the requirements
of the degree of

Doctor of Philosophy
of the

Indian Institute of Technology, Bombay, India
and

Monash University, Australia

by

Manohar Chinnareddy Venkateswarlu

Supervisors:

Prof Sagar Mitra (IIT Bombay)

Prof Douglas R Macfarlane (Monash University)



*The course of study for this award was developed jointly by
Monash University, Australia and the Indian Institute of Technology, Bombay
and was given academic recognition by each of them.
The programme was administrated by The IITB-Monash Research Academy*

(Year 2018)

Dedicated

To My parents

Mr. & Mrs. Venkateswarlu and Jayalakshmi

And

To my siblings

Dhakshayani and Janardhan

This Humble work is a sign of my love to you

Declaration

I declare that this written submission represents my ideas in my own words and where others' ideas or words have been included, I have adequately cited and referenced the original sources. I also declare that I have adhered to all principles of academic honesty and integrity and have not misrepresented or fabricated or falsified any idea/data/fact/source in my submission. I understand

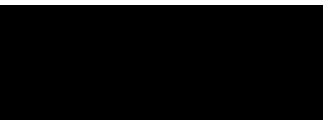
that any violation of the above will be cause for disciplinary action by the Institute and can also evoke penal action from the sources which have thus not been properly cited or from whom proper permission has not been taken when needed.

Notice 1

Under the Copyright Act 1968, this thesis must be used only under the normal conditions of scholarly fair dealing. In particular no results or conclusions should be extracted from it, nor should it be copied or closely paraphrased in whole or in part without the written consent of the author. Proper written acknowledgement should be made for any assistance obtained from this thesis.

Notice 2

I certify that I have made all reasonable efforts to secure copyright permissions for third-party content included in this thesis and have not knowingly added copyright content to my work without the owner's permission.



Student Name: Manohar Chinnareddy Venkateswarlu

IITB ID: 

Monash ID: 

Abstract

Energy production and storage have become major challenges in our day to day life. Zero emission vehicles and portable electronics require high-energy and high-power density systems. Li-ion batteries have high volumetric energy density, and have been widely explored and used in portable electronics. They are also used to power plug-in hybrid electric vehicles and electric vehicles. As well as “mobile” applications, low cost batteries are required for smarter electric grids that integrate discontinuous energy flow from renewable sources, optimizing the performance of clean energy sources. Energy density is not as critical for these applications and given the likely increasing price and decreasing supply of Li, Na-ion batteries are a very promising alternative. Elemental Na exhibits similar chemistry to Li, and therefore should be able to be used in batteries. However, a commercially-realistic focus on exploring cathode materials, anode materials and electrolytes for Na-ion batteries is needed to bring these batteries to market. The electrolyte plays a major role in transporting the sodium ions between cathode and anode in a Na-ion battery, as well as in intercalation of Na ions into the electrodes. So far, there are no commercialized electrolytes for Na-ion batteries which operate at room temperature to give stable electrochemical performance, safety and a wide potential window.

Organic electrolytes do not have high thermal stability in Na-ion batteries. Thermal stability may be improved by using new electrolyte solvents, such as ionic liquids. Ionic liquids have significant properties of increased safety (wide potential window), high electrochemical stability, good ionic conductivity and wide liquid temperature range in Na-ion batteries. This work aims to develop ionic-liquid based electrolytes for high energy density sodium ion battery by using different synthesis of sodium vanadium phosphate cathode material, commercial hard carbon anode material with 1M NaFSI salt dissolved in different organic solvents (Ethylene carbonate and Propylene carbonate), N-methyl N-pyrrolidinium

bis(trifluoromethanesulfonyl)imide (C₃mpyrTFSI), and N-methyl N-pyrrolidinium bis(fluoromethanesulfonyl)imide (C₃mpyrFSI) based electrolyte for sodium ion battery. The hybrid electrolyte and ionic liquid electrolytes showed excellent cycling performance with high rate capability for NVP@C and Hard carbon electrodes in sodium ion batteries. These electrolytes formed a more stable passivation layer on the surface of NVP@C, Hard carbon and sodium metal surfaces in sodium ion batteries. Further, studied the organic, hybrid and ionic liquid electrolytes thermal decomposition reaction mechanism in sodium ion batteries. Finally, Developed the low-cost bioderived hard carbon as anode material and NVP@C cathode material for Sodium ion battery. It shows excellent cycling performance with high safety batteries for large scale grid storage applications. C₃mpyrTFSI and C₃mpyrFSI ionic liquid- based electrolytes enhanced the electrochemical performance, and safety of the full cell sodium ion batteries.

Keywords: Sodium ion battery, NVP@C, Hard carbon, Ionic liquid, Electrolyte, Solid electrolyte interface.

Table of Contents

List of Figures.....	i
List of Tables	v
Abbreviations	vi
Nomenclature	viii
Chapter 1	1
1.1 Motivation.....	1
1.2 Batteries:.....	1
1.3 Lithium-ion battery:	3
1.4 Sodium-ion battery:	4
1.5 Sodium-ion battery components:.....	5
1.5.1 Anode materials:	6
1.5.2 Cathode materials:.....	10
1.5.3 Electrolytes:	15
1.5.4 Binders for sodium-ion batteries:	22
1.5.5 Current collectors:	23
1.5.6 Separators for sodium-ion batteries:.....	23
1.6 Scope of the work:.....	24
1.6.1 Outline of thesis:	26
Chapter 2	27
Experimental and methods	27
2.1 Chemicals:	27
2.1.1 Chemical for synthesis:.....	27
2.1.2 Chemicals for cell and electrolyte preparation:	27
2.1.3 Chemical for electrode preparations:.....	28
2.2 Material synthesis:	28
2.2.1 Synthesis of carbon coated sodium vanadium phosphate (NVP/C):	28
2.2.2 Synthesis of carbon encapsulated sodium vanadium phosphate (NVP@C):.....	28
2.2.3 Synthesis of composite of sodium vanadium phosphate material (NVP@C):	29
2.2.4 Synthesis of Bio derived Hard carbon:	29
2.3 Preparation of organic, additive, hybrid and ionic liquid electrolytes:.....	30
2.3.1 Organic electrolytes:	30
2.3.2 Additive electrolyte:	30
2.3.3 Hybrid electrolytes:.....	30
2.3.4 Ionic liquid electrolytes:	31
2.4. Materials Characterization:.....	31
2.4.1 X-ray diffraction analysis:.....	31
2.4.2 Scanning electron microscopy:	32
2.4.3 Transmission electron microscopy:	32
2.4.4. Fourier transform infrared spectroscopy (FT-IR):	32

2.4.5 Thermogravimetric analysis (TGA):.....	33
2.4.6 Thermogravimetric analysis- Infrared (TGA-IR):	33
2.5 Electrode and cell fabrication:.....	33
2.6 Electro chemical characterization:.....	35
2.6.1 Cyclic voltammetry:.....	35
2.6.2 Galvanometric charge-discharge cycling:.....	35
2.6.3 Electrochemical impedance spectroscopy:.....	36
2.7 AC Impedance Ionic conductivity:	36
2.8 Viscosity Measurement:.....	36
Chapter 3	37
Role of N-Propyl-N-Methyl Pyrrolidinium bis (trifluoro methanesulfonyl) imide as an Electrolyte Additive in Sodium Battery Electrochemistry	37
3.1 Introduction.....	37
3.2 NVP/C characterization:	38
3.3 NVP/C cathode material comparison with previous studies:.....	39
3.4 Organic and additive electrolyte electrochemical performance with NVP/C and Na metal:.....	39
3.5. SEI characterization studies on NVP/C cathode material with organic and organic + IL electrolyte:	43
3.6 Summary:	50
Chapter 4	51
Stability-enhancing ionic liquid based hybrid electrolyte for NVP@C cathode based sodium-ion batteries	51
4.1 Introduction:	51
4.2 Synthesis and Characterization of NVP@C electrodes:.....	52
4.3 Characterization of hybrid electrolytes:	55
4.4 NVP@C combined with hybrid electrolytes:	57
4.4.1 Characterization of Na metal and NVP@C SEI layers:.....	58
4.5 Summary:	67
Chapter 5	68
Pure ionic liquid electrolytes development in high energy density sodium-ion batteries.....	68
5.1 Introduction:	68
5.2 Hard carbon material characterization:.....	68
5.3 Characterization of organic and ionic liquid electrolyte:.....	69
5.4 Electrochemical performance of NVP@C and hard carbon with Na metal:	71
5.5 Electrochemical performance of NVP@C Hard carbon full cell:.....	73
5.6 SEI characterization of NVP@C and Hard carbon:	74
5.7 Summary:	82
Chapter 6	83
Ionic liquid added electrolytes improve the physio-chemical properties and stabilize the SEI layer in sodium batteries	83
6.1 Introduction.....	83
6.2 TGA-IR studies of organic, hybrid and ionic liquid electrolytes:.....	84

6.3 Characterization of SEI layers on NVP@C and Sodium metal surfaces:	90
6.4 Summary:	94
Chapter 7	95
Low-cost sodium-ion battery using almond-shell based hard carbon anode and NVP@C cathode...	95
7.1 Introduction.....	95
7.2 Characterization of Bioderived Hard carbon and NVP@C materials:	97
7.3 Electrochemical characterization of NVP@C IL HC full cell sodium ion battery:	102
7.4 Summary:	105
Chapter 8	106
Concluding remarks and Future scope	106
8.1 Concluding Remarks:.....	106
8.2 Future scope:	108
References:	109
Publications:	117
Conferences:	117
Awards:	118
Acknowledgements	119

List of Figures

Figure 1. 1: Comparison plot of energy density and power density of different energy storage devices ²	2
Figure 1. 2: The abundance of chemical elements in Earth's crust ¹⁰	3
Figure 1. 3: Schematic diagram of sodium-ion battery working mechanism ¹²	4
Figure 1. 4: Potential versus Specific capacity plots for different (a) cathode, (b) anode materials studied for their applications in sodium-ion batteries ¹³	5
Figure 1. 5: "House of cards model" for sodium-filled hard carbon anode materials for sodium-ion batteries ¹⁴	6
Figure 1. 6: Alloying reaction mechanism in the sodium-ion battery ²⁰	7
Figure 1. 7: Conversion reaction mechanism in sodium-ion batteries ²⁰	9
Figure 1. 8: Sodium host layered oxide (Na _x TMO ₂) schematic crystal structures for a) P2-type, b) O2-type, c) O3-type, and d) P3-type stacking cathode materials for sodium-ion batteries. In the crystal structure, blue and yellow balls represent the transition-metal and Na ions in the O-type frameworks ⁴⁰	11
Figure 1. 9: NASICON-type crystal structure of Na ₃ V ₂ (PO ₄) ₃ cathode material ⁴⁶	13
Figure 1. 10: Crystal structures of NaFePO ₄ cathode material in Triphylite and Maricite phases for sodium-ion battery, FeO ₆ octahedra and PO ₄ tetrahedra are shown in green and blue, respectively. Na atoms are shown as yellow spheres ⁴⁷	14
Figure 1. 11: Molecular structures of different IL cations and anions ⁸⁶	21
Figure 2. 1: Schematic diagram of lignin extraction process from almond shell	29
Figure 2. 2: Experimental setup of sodiation of hard carbon electrode by sodium metal with ionic liquid electrolyte.	34
Figure 3. 1: NVP/C characterization. (a) Powder XRD pattern, (b) Raman spectrum, (c) FEG-SEM image, and (d) HR-TEM images.	38
Figure 3. 2: (a) CV curves for NVP/C, (b) Cycling performance of NVP/C at various C-rates with organic and organic+IL electrolytes.	40
Figure 3. 3: (a) Charge-discharge cycling performance and (b) Coulombic efficiency of NVP/C in organic and organic+IL electrolytes at C/2 rate, with potential ranging from 2.5 to 3.8 V (vs Na/Na+), (c) Potential vs. Capacity plot of NVP/C cathodes with organic elect electrolyte, and (d) with organic+IL electrolyte. All cells used sodium metal anodes.	41
Figure 3. 4: (a) Charge-discharge cycling performance, and (b) Coulombic efficiency of NVP/C in 1M NaClO ₄ in PC with FEC and different amounts of [C3mpyr] [NTf ₂] IL added. C/2 rate, with potential ranging from 2.5 to 3.8 V (vs Na/Na+).	42
Figure 3. 5: Specific capacity vs. cycle number for 5th, 20th and 50th cycles for different amounts of IL in 1M NaClO ₄ in PC electrolyte. SD values are based on measurements of at least five separate cells.	43
Figure 3. 6: XPS C1s Peaks for NVP/C cathodes. (a) Pristine, and after 50 cycles with (b) Organic, (c) Organic+IL electrolytes	44
Figure 3. 7: Raman spectra of NVP/C cathode electrode for pristine and after 50 cycles with Organic and ionic liquid added electrolyte	45
Figure 3. 8: FEG-SEM-EDS images of NVP/C electrodes. (a) pristine, (b) after 50 cycles with organic electrolyte, and (c) after 50 cycles with organic+IL electrolyte	46
Figure 3. 9: HR-TEM images of NVP/C electrodes after 50 cycles with (a) organic electrolyte (b) organic+IL electrolyte	47
Figure 3. 10: Nyquist plots of NVP/C Na Cells (a) after aging the cell for one day; then after (b) 1st cycle, (c) 10th cycle, and (d) 50th cycle with organic and organic+IL electrolytes	48

Figure 3. 11: Diffusion coefficient (as evaluated from Warburg impedance) for NVP/C material at different potentials during first discharging cycle in inorganic and organic +IL electrolytes.49

Figure 4. 1: Schematic representation of NVP@C synthesis	52
Figure 4. 2: Characterization of NVP@C: (a) Powder XRD pattern (red is experimental, black is literature); (b) Raman spectrum; (c) FE-SEM image; and (d) HR-TEM images.....	53
Figure 4. 3: Electrochemical performance of NVP@C: (a) CV curve measured from 2.5 to 3.8 V vs. Na/Na ⁺ , scan rate 0.05 mVs ⁻¹ in organic electrolyte (b) Cycling performance at various C-rates (c) Cycling performance at 0.5C rate; potential range from 2.5 to 3.8 V vs. Na/Na ⁺ with 1M NaClO ₄ in a EC: PC electrolyte at 20 ⁰ C.....	54
Figure 4. 4: (a) Ionic conductivity (b) viscosity and (c) TGA measurements for organic and hybrid electrolytes.....	55
Figure 4. 5: Electrochemical oxidative stability tests (by cyclic voltammetry) in three electrode Swagelok cells at 10mVs ⁻¹ scan rate.....	56
Figure 4. 6: (a) CVs for NVP@C, at a scan rate of 0.05 mVs ⁻¹ , (b) Cycling performance of NVP@C at various C-rates (c) Cycling performance of NVP@C with organic electrolyte and hybrid electrolytes at 0.5C; (d) Coulombic efficiency of NVP@C with organic and hybrid electrolytes at 0.5C; potential range from 2.5 to 3.8 V vs Na/Na ⁺	57
Figure 4. 7: Electrochemical impedance measurements for Na//Na symmetrical cells at (a) OCV, (b) after 50 cycles, and (c) after 100 cycles with organic and hybrid electrolytes.	59
Figure 4. 8: Electrochemical impedance measurements for NVP@C at (a) OCV, (b) after 1 cycles, (c) after 50 cycles, (d) after 100 cycles with organic and hybrid electrolytes.	60
Figure 4. 9: FEG-SEM images of NVP@C electrodes: pristine and after 100 cycles with organic and hybrid electrolytes.	62
Figure 4. 10: EDX analysis of NVP@C electrode cycled with organic and hybrid electrolytes.	63
Figure 4. 11: HR-TEM images of NVP@C electrodes after cycling with (a) organic, and (b) hybrid-2 electrolyte.	63
Figure 4. 12: HR-TEM images of Passivation layer on the surface of NVP@C electrode after cycling with (a) Organic, (b) Hybrid-1, (c) Hybrid-2 and (d) Hybrid-3 electrolyte.	64
Figure 4. 13: XPS spectra of NVP@C cycled electrode with organic and hybrid electrolytes.	66

Figure 5. 1: Commercial hard carbon anode material morphology and structural information by (a) XRD, (b) Raman and (c) SEM.	69
Figure 5. 2: TGA measurements for organic and ionic liquid electrolytes.	70
Figure 5. 3: Electrochemical oxidative stability tests were performed in three electrode swagelok cells at 10 mVs ⁻¹ scan rate.	70
Figure 5. 4: Electrochemical characterization of NVP@C Na metal cell with ionic liquid electrolyte: (a) Cyclic Voltammogram, (b) Potential vs. Specific capacity curves obtained at different rates for NVP@C Na cell, (c) Charge-discharge cycling performance at C/2 r	71
Figure 5. 5: Electrochemical performance of hard carbon Na cell with ionic liquid electrolyte (a) Cyclic voltammetry performed at a scan rate of 0.1 mVs ⁻¹ , (b) The charge-discharge cycling performance of hard carbon at different rates in the potential range of 0.0.....	72
Figure 5. 6: Electrochemical characterization of NVP@C hard carbon cell with IL electrolyte for (a) Cyclic voltammogram, (b) Charge-discharge cycling performance of full cell with IL electrolyte at different current density rates, (c) Potential vs. specific capaci.....	73
Figure 5. 7: Electrochemical impedance measurements for NVP@C Na, Hard carbon Na, and NVP@C Sodiated Hard carbon cell at (a) OCV, (b) after 5 cycles, (c) after 50 cycles, (d) after	

100 cycles with ionic liquid electrolyte.	75
Figure 5. 8:Ex situ FTIR spectra of electrodes extracted from NVP@C Sodiated Hard carbon cells. (a) NVP@C, pristine and after 100 cycles; (b) hard carbon, pristine (not sodiated) and after 100 cycles.	76
Figure 5. 9:Raman spectra of electrodes from NVP@C sodiated hard carbon cells. (a) NVP@C, pristine and after 100 cycles, (b) hard carbon, pristine (not sodiated) and after 100 cycles.....	77
Figure 5. 10:XPS spectra for pristine and after 100 cycles with organic and ionic liquid electrolytes for (a) NVP@C and (b) HC electrodes.	78
Figure 5. 11:FEG-SEM of hard carbon (a) in pristine state, (b) Sodiated Hard carbon (i.e. after 30 minutes in contact with Na metal wet with IL electrolyte), and (c) after 100 cycles in a cell comprising NVP@C Sodiated hard carbon.	79
Figure 5. 12:HR-TEM images of (a) Pristine NVP@C, (b) Pristine Hard carbon (not sodiated), (c) NVP@C electrode after 100 cycles, and (d) Hard carbon electrode after 100 cycles.	80
Figure 5. 13:NVP@C Pre-sodiated hard carbon full sodium-ion battery prototype demonstration video, showing an LED study lamp with a 2032 coin cell.	81
Figure 6. 1:TGA curves of (a) organic, (b) hybrid, and (c) ionic liquid electrolytes.....	84
Figure 6. 2:: Gaseous thermal decomposition products detected by FTIR spectra for (a) organic, (b) hybrid, and (c) ionic liquid electrolytes.	85
Figure 6. 3: Charge-discharge cycling performance of NVP@C /electrolyte/Na-foil cell using (a) organic, (b) hybrid and (c) ionic liquid electrolytes.	87
Figure 6. 4:Plating and stripping cycles of Na Na symmetrical cells with organic, hybrid and ionic liquid electrolytes at 0.1 mAcm ⁻²	88
Figure 6. 5:First cycle plating and stripping reaction of Na Na symmetrical cells with organic, hybrid and ionic liquid electrolytes.....	89
Figure 6. 6:Ex-situ FTIR spectra of NVP@C cathode material: pristine and after 100 cycles with organic, hybrid and ionic liquid electrolytes.....	90
Figure 6. 7:Ex-situ FTIR spectra of sodium metal extracted from Na Electrolyte NVP@C cells after 100 cycles with organic, hybrid or ionic liquid electrolytes.....	91
Figure 6. 8:SEM images of Sodium metal and separator after 100 cycles with (a) & (d) organic electrolyte, (b) & (e) hybrid electrolyte and (c) & (f) ionic liquid electrolyte.....	92
Figure 6. 9:EDX analysis of sodium metal surface with (a) organic, (b) hybrid, and (c) ionic liquid electrolytes.	93
Figure 7. 1:Characterization of bioderived hard carbon: (a) Powder XRD pattern and (b) Raman spectrum.	97
Figure 7. 2: Bioderived hard carbon anode material morphology and structural information: (a) SEM, and (b) TEM images.	97
Figure 7. 3:Electrochemical performance of bioderived hard carbon with ionic liquid electrolyte (a) Cyclic voltammetry performed at a scan rate of 0.1 mVs ⁻¹ , (b) The charge-discharge cycling performance of hard carbon at different current rates in the potential ran .	98
Figure 7. 4:(a) Potential versus Capacity plot of hard carbon anode material for first and 1000th cycles, (b) Charge-discharge cycling performance of hard carbon for 1000 cycles at 1C rate in the potential range of 0.01 to 2V vs Na/Na ⁺	99
Figure 7. 5:: NVP@C cathode material structural and morphology analysis by: (a) XRD, (b) SEM, and (c) TEM.....	100
Figure 7. 6:Electrochemical characterization of NVP@C cathode material with ionic liquid electrolyte (a) Cyclic voltammetry performed at a scan rate of 0.05 mVs ⁻¹ , (b) Potential vs. Specific capacity curves obtained at different current density rates for NVP@C/IL/N	101

Figure 7. 7:Electrochemical characterization of NVP@C/IL/HC cell (a) Charge-discharge cycling performance at the 0.5C rate for 350 cycles, and (b) Potential vs. specific capacity curves at second and 350th cycles, at the 0.5C-rate.	102
Figure 7. 8:Potential vs Specific capacity curve for (HC 1M NaFSI in C3mpyrFSI NVP@C) cell at first cycle with 0.5 C current rate.	103
Figure 7. 9:Cycling performance of (HC 1M NaFSI in C3mpyrFSI NVP@C) cell with organic and ionic liquid electrolyte for 100 cycles at 0.5C rate.	104

List of Tables

Table 1. 1: Basic characteristics of Sodium-ion and Lithium-ion batteries ¹¹	4
Table 1. 2: Structures and properties of sodium salts used in sodium-ion battery electrolytes ⁵⁷	16
Table 1. 3: Chemical structures and properties of organic solvents used in sodium-ion battery electrolytes ⁵⁷	17
Table 2. 1 : Organic, hybrid and ionic liquid electrolyte compositions.	31
Table 3. 1: NVP/C electrochemical performance in 1M NaClO ₄ in PC electrolyte with different additives.	42
Table 3. 2 : Listing of Raman peaks and their assignments for the spectra of the SEI layers on NVP@C electrodes after cycling with organic and ionic liquid added electrolyte.	45
Table 4. 1: RC Circuit and resistance values for hybrid electrolytes in sodium ion battery.	61
Table 4. 2: Different electrolyte compositions in sodium and lithium ion battery literature. ..	64
Table 5. 1: Listing of Raman peaks and their assignments for the spectra of the SEI layers on NVP@C and hard carbon electrodes after cycling with IL electrolyte.	77
Table 5. 2 : Summary of electrochemical performance of various sodium-ion batteries.	81

Abbreviations

NaClO ₄	Sodium perchlorate
NaTFSI	Sodium bis(trifluoromethanesulfonyl) imide
NaFSI	Sodium bis(fluoromethanesulfonyl)imide
NaPF ₆	Sodium hexafluorophosphate
NaBF ₄	Sodium tetrafluoroborate
PC	Propylene carbonate
EC	Ethylene carbonate
DMC	Di methyl carbonate
DEC	Di ethylene carbonate
FEC	Fluoroethylene Carbonate
EMC	Ethyl methylene carbonate
Na	Sodium
Li	Lithium
HC	Hard carbon
NVP	Sodium vanadium phosphate
NVP@C	Sodium vanadium phosphate with carbon composite
Na ₃ V ₂ (PO ₄) ₃	Sodium vanadium phosphate
Na ₃ V ₂ (PO ₄) ₃ /C	Sodium vanadium phosphate with carbon composite
C ₃ mpyrTFSI	N-propyl-N-methyl-pyrrolidinium bis(trifluoromethanesulfonyl)imide
C ₃ mpyrFSI	N-propyl-N-methyl-pyrrolidinium bis(fluoromethanesulfonyl)imide
C ₄ mpyrTFSI	N-butyl-N-methyl-pyrrolidinium bis(trifluoromethanesulfonyl)imide
C ₄ mpyrFSI	N-butyl-N-methyl-pyrrolidinium bis(fluoromethanesulfonyl)imide
FEG-SEM	Field Emission Gun Scanning Electron Microscope

FEG-TEM	Field Emission Gun Transmission Electron Microscope
HR-TEM	High Resolution Transmission Electron Microscope
TGA	Thermal Gravimetric Analysis
FT-IR	Fourier Transform InfraRed
ATR	Attenuated Total Reflectance
XPS	X-ray Photo Electron Spectroscopy
IR	InfraRed
EIS	Electrochemical impedance spectroscopy
SEI	Solid electrolyte interface
CV	Cyclic Voltammetry
LSV	Linear Sweep Voltammetry
IL	Ionic liquid
ILs	Ionic liquids
XRD	X-ray Diffraction
PVDF	Polyvinylidene difluoride
CMC	Carboxy methyl cellulose
PAA	Polyacrylic Acid
NMP	N-methyl Pyrrolidine
SIB	Sodium ion battery

Nomenclature

R_{Sol}	Solution resistance, Ω
R_{SEI}	Solid electrolyte interface resistance, Ω
R_{ct}	Charge transfer resistance, Ω
CPE_{dl}	Constant phase element for double layer
CPE_{SEI}	Constant phase element for solid electrolyte interface
W	Warburg Impedance
Θ	Angle between incident beam and atomic planes
λ	Wavelength of the incident beam, nm
Z	Impedance
Z_{re}	Real part of impedance
Z_{Im}	Imaginary part of impedance

Chapter 1

1.1 Motivation

Climate change caused by consumption of fossil fuels and emission of greenhouse gases has increased the CO₂ levels in the atmosphere¹. In order to control the CO₂ levels, energy production must use renewable and sustainable energy sources. In these cases, the power system must have some energy storage capability to overcome the fluctuations in the energy supply. Renewable sources such as solar and wind are not continuously available, so efficient energy storage technologies are needed to level the peak load² and allow the electricity grid to work effectively³.⁴ Energy storage technologies can be divided into four categories: mechanical, electrical, chemical and electrochemical for large-scale applications⁵.

Batteries are used as storage devices in domestic life and have good efficiency, stability, and greater reliability than other energy storage devices⁵. Energy storage is defined in terms of energy density and chemical energy¹. Batteries store chemical energy and produce electricity with high conversion and without polluting the environment. Researchers are interested in developing low cost, highly safe, rechargeable batteries, which can supply adequate voltage and high capacity for many cycles.

1.2 Batteries:

The battery is a device that generates electrical energy from electrochemical oxidation and reduction reactions. Batteries may be single-use (primary), or rechargeable (secondary). The electrochemical reactions in primary batteries are not reversible. Examples of primary batteries are zinc-carbon, mercury, alkaline, lithium, and sodium batteries. These batteries can be used in limited capacity applications, due to their lower self-discharge rate. Secondary batteries have reversible electrochemical reactions. Examples of secondary batteries are lead-acid, nickel-metal hydride, nickel-cadmium, lithium-ion, and sodium-ion batteries.

Batteries can be characterized in terms of energy and power density. Energy densities may be given relative to the mass of the device (gravimetric energy density, Wh.kg^{-1}) or its volume (volumetric energy density, Wh.l^{-1}) for energy storage devices.

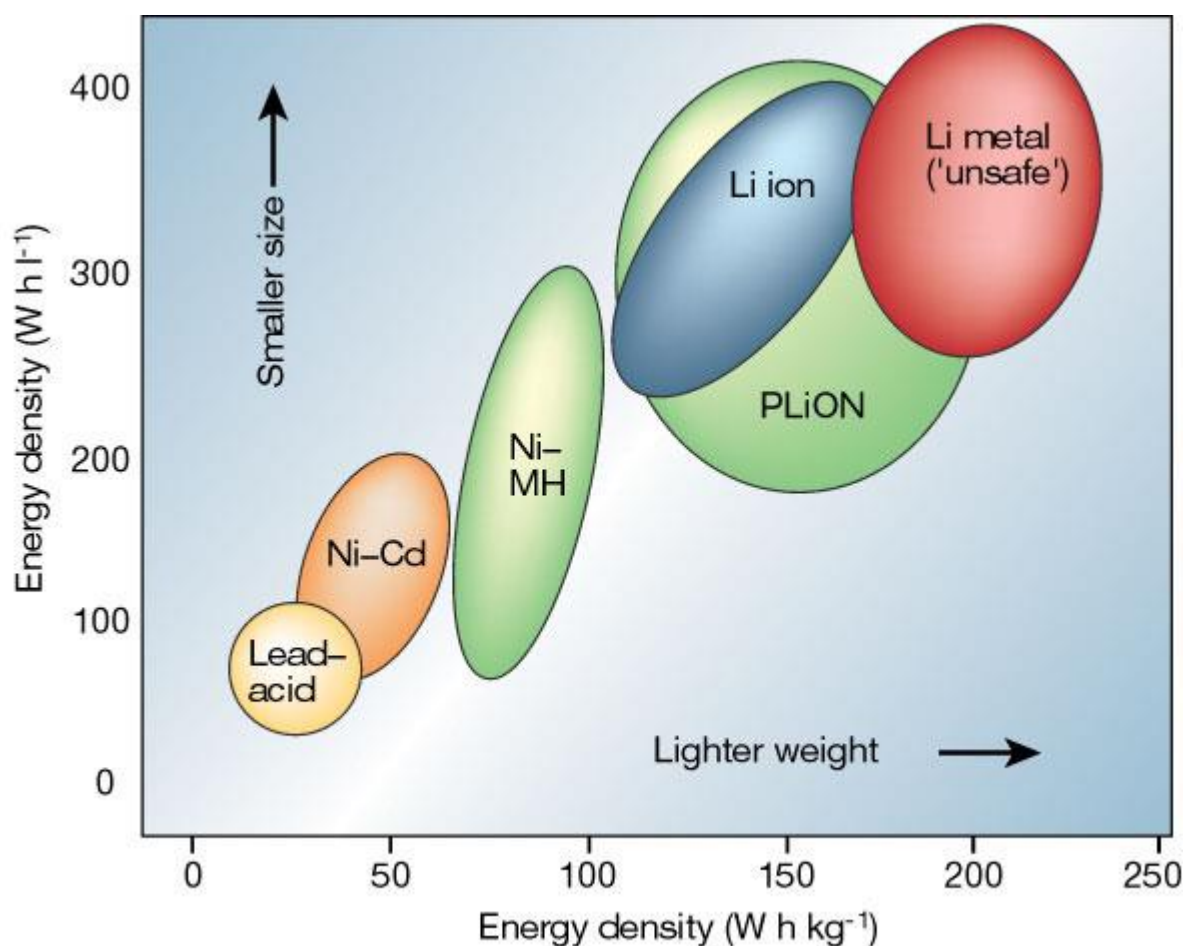


Figure 1. 1: Comparison plot of energy density and power density of different energy storage devices².

Power densities describe the rate of discharge in batteries. Usually, batteries should possess a higher energy density and power density for large-scale energy storage applications. Energy and power density values for typical batteries are shown in Figure 1.1. Battery charge-discharge rates are measured in the units of mill ampere-hour or ampere-hour and denoted by C-rates, which are related to the theoretical capacity of the lithium or sodium reversible electrode

materials. For example, the capacity of a battery is commonly rated at 1C, meaning that a fully charged battery rated at 1Ah should provide 1A for one hour.

1.3 Lithium-ion battery:

Li-ion battery energy storage systems are successfully used in the portable electronics, and are becoming popular for powering automobile applications in the electric vehicle market². However, there may be an issue with the scarcity and price of lithium in the future⁶. Sodium may be an alternative to lithium for sustainable energy storage; sodium is abundant (Figure 1.2), cheap, recyclable⁷, and allows copper anode current collectors to be replaced with cheaper aluminum⁸. These advantages of sodium-ion batteries (SIBs) suggest that they could be competitive with lithium-ion batteries for large-scale applications, where weight is not the primary consideration⁹. Nowadays, researchers focus on developing a low cost and high-performance sodium-ion battery to replace the lithium-ion battery.

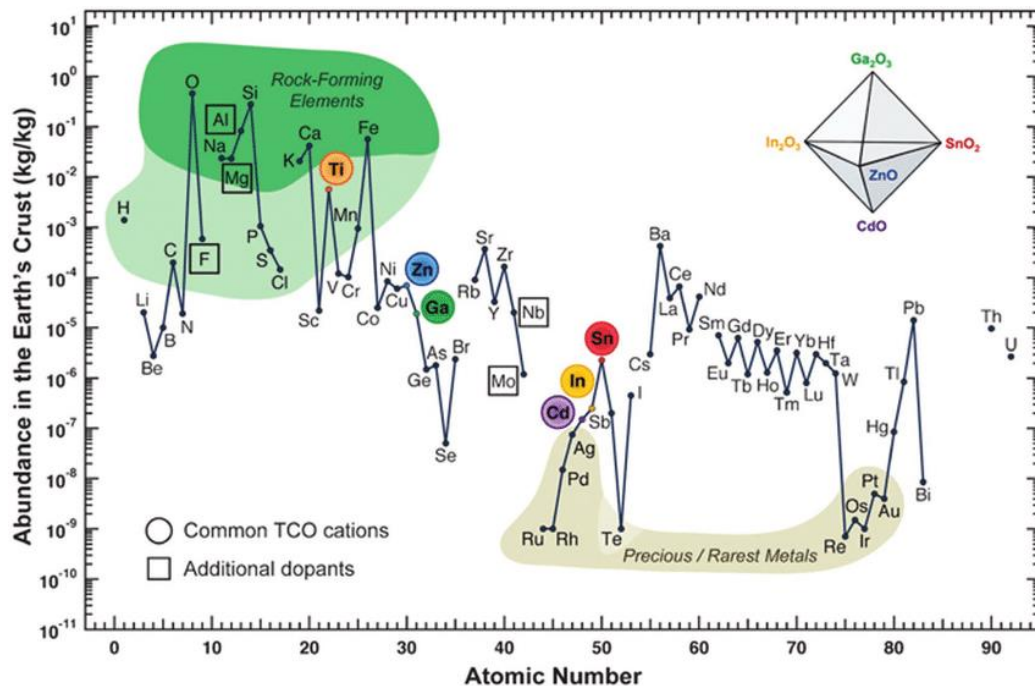


Figure 1. 2:The abundance of chemical elements in Earth's crust¹⁰.

Some of the important characteristics of sodium and lithium ions are given in Table 1.1.

Table 1. 1: Basic characteristics of Sodium-ion and Lithium-ion batteries¹¹.

Characteristics	Na	Li
Price (for carbonates) ⁴	0.07–0.37 ^a € kg ⁻¹	4.11–4.49 ^b € kg ⁻¹
Capacity density	1.16 A h g ⁻¹	3.86 A h g ⁻¹
Voltage vs. S.H.E. ^c	–2.7 V	–3.0 V
Ionic radius	0.98 Å	0.69 Å
Melting point	97.7 °C	180.5 °C

^a Purity: 98.8–99.2% min. ^b Battery grade: 99.9%. ^c S.H.E.: Standard Hydrogen Electrode.

1.4 Sodium-ion battery:

Sodium-ion batteries have similar intercalation chemistry to that of lithium-ion batteries¹¹. Sodium-ion batteries have lower energy density than lithium-ion batteries, due to the higher equivalent weight and higher ionization potential of sodium. In sodium-ion batteries, sodium-ion transport between cathode and anode occurs through the electrolyte, as shown in Figure 1.3. Reported literature data of cathode and anode materials for sodium-ion batteries are shown in Figure 1.4.

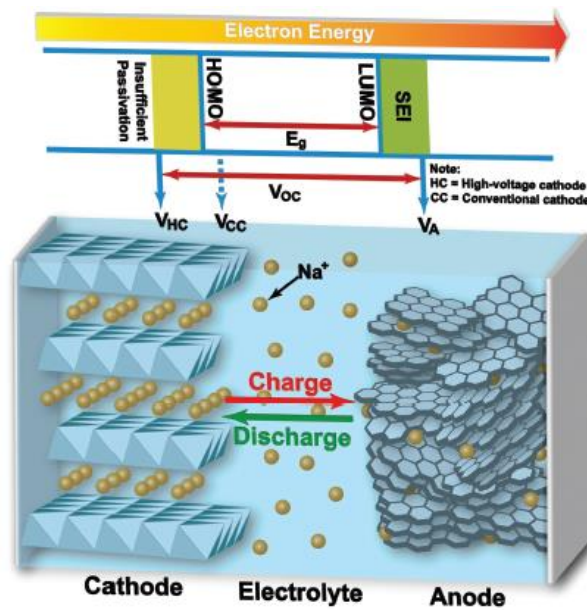


Figure 1. 3:Schematic diagram of sodium-ion battery working mechanism¹².

and are generated/consumed by oxidation/reduction reactions of the active electrode materials. The active electrode materials are cast onto the current collectors, which pass the electrons to the external circuit. The positive and negative electrodes are separated by a membrane-type separator, to prevent their direct contact and avoid a short circuit.

1.5.1 Anode materials:

Anode materials have a lower operating potential window, and the anode potential must be above the potential at which sodium metal deposits in sodium batteries.

This material is used as a cathode material and sodium foil as an anode material in half-cell configuration of sodium metal batteries. It is used as negative electrode material opposite with sodium host cathode material in full cell sodium-ion batteries for different applications. Anode materials are classified on the basis of electrochemical reaction kinetics of sodium ion in sodium-ion batteries.

1.5.1.1 Carbonaceous anode material for sodium-ion battery:

Carbonaceous materials are important anode materials for sodium-ion batteries. Graphite is well known as an anode material for lithium-ion batteries, where it demonstrates an appropriately low operating potential, good reversible capacity, high rate capability and good long-term cycling stability. However, this material cannot be used as an anode material in a sodium-ion battery, because the large sodium ion cannot easily enter graphite.

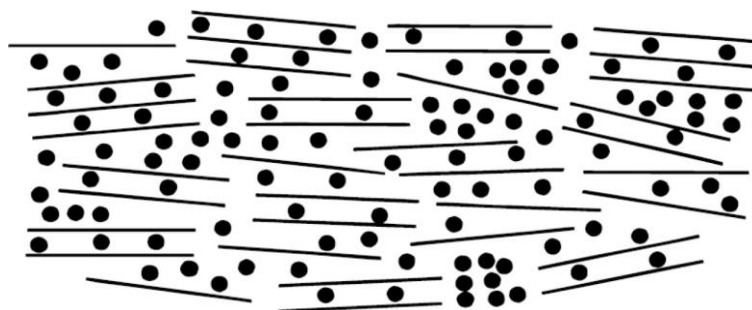


Figure 1. 5:“House of cards model” for sodium-filled hard carbon anode materials for sodium-ion batteries ¹⁴.

Doeff et al. successfully reversible sodium intercalation and deintercalation in soft carbon anode materials in sodium metal batteries¹⁵. In 2003, Dahn et al. synthesized a hard carbon for sodium-ion battery anodes from glucose using a high-temperature pyrolysis process¹⁴. Sodium inserts easily between the graphene layers and in the nanopores in the disordered hard carbon material, shown schematically in the “house of cards” model of Figure 1.8. Further, Komaba et al. stabilized and enhanced the capacity and initial coulombic efficiency and controlled the solid electrolyte interface layer formation by optimizing the electrolyte composition through selection of additive and binders¹⁶. Recently, bioderived hard carbon materials were synthesized from biomass waste precursors¹⁷⁻¹⁹. Ionic liquid derived N-doped carbon materials has been synthesized and used as electrode materials in lithium and sodium ion batteries. It acts a pseudo capacity behavior type material for lithium and sodium ion batteries²⁰. These materials are likely to reduce the cost of production and improve the sustainability of sodium-ion batteries.

1.5.1.2 Alloying type anode materials for sodium-ion batteries:

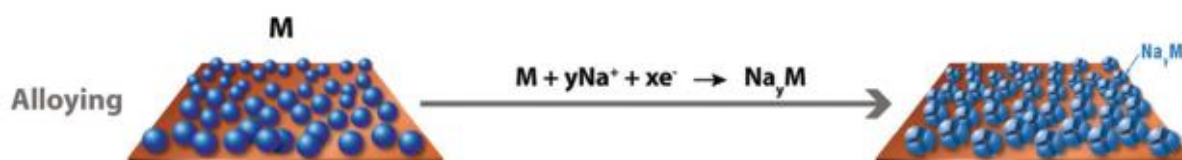


Figure 1. 6:Alloying reaction mechanism in the sodium-ion battery²¹.

Some materials (including both metals and non-metals: tin, antimony, bismuth, lead, germanium, and phosphorus) exhibit a reversible alloying reaction with sodium, and are able to act as high energy density anode materials for sodium-ion batteries (Figure 1.9). For example, metallic tin has been proposed as an anode material for room temperature sodium-ion batteries,^{22, 23} Tin anodes have a theoretical capacity of 847 mAhg^{-1} and can store 3.75Na per Sn. Ellis et al. examined the electrochemical activity of Sn versus sodium in sodium-metal batteries²⁴, and found that alloying between sodium and tin has a four step reaction mechanism:

NaSn₃, NaSn, Na₉Sn₄, and Na₁₅Sn₄. However, this volume of this anode changes drastically with cycling, and the anode is also unstable in contact with many electrolytes. The electrochemical performance of Sn can be improved by doping with inactive elements (Cu) and the volume expansion can be suppressed by optimizing the binder and the electrolyte additives²⁵. Binary (Sn-Ge)²⁶, and ternary (Sn-Ge-Sb²⁷ & Sn-Bi-Sb²⁸) Sn alloys have also been examined as anode materials for sodium-ion batteries. Chen and co-workers successfully synthesized Sn nanodots encapsulated with N-doped carbon nanofiber by an electrospinning and thermal reduction method to give a sodium battery anode material which showed excellent electrochemical performance with a good reversible capacity of 450 mAhg⁻¹ with 10 Ag⁻¹ current density rates for 1300 cycles with organic electrolytes²⁹. Yang et al. demonstrated an Sb/C composite anode for room-temperature sodium batteries³⁰, and found excellent electrochemical performance, with a specific capacity of 600 mAhg⁻¹ for 100 cycles with an organic electrolyte containing added FEC (Fluoroethylene carbonate). Nithya and Gopukumar successfully synthesized a reduced graphene oxide (rGO)/Sb nanocomposite as an alloying anode material, and found excellent reversibility of sodium alloying reactions and a specific capacity of 452 mAhg⁻¹ at a current density of 100mA g⁻¹³¹. Song et al. made a nanocomposite sodium-ion battery anode by combining graphene nanosheets with red phosphorous nanoparticles. This anode showed a high reversible specific capacity of 2077 mAhg⁻¹ with a current density of 260 mA g⁻¹ for 60 cycles in sodium metal batteries³². Several other red phosphorous nanocomposite anode materials have been synthesized, based on rGO, CNT, graphene nanosheets and N-doped carbon nanofiber hybrid systems for sodium batteries²¹.

1.5.1.3 Conversion type anode materials for sodium-ion batteries:

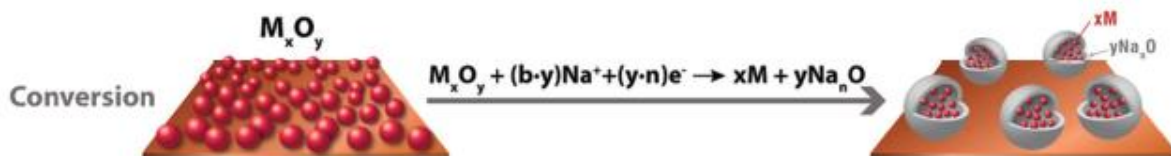


Figure 1. 7:Conversion reaction mechanism in sodium-ion batteries²¹.

Tirado and co-workers first proposed $NiCo_2O_4$ as a TMO (Transition-metal oxide) based conversion-anode material for sodium-ion batteries (Figure 1.10). This material shows a reversible capacity of 200 mAhg^{-1} by forming Na_2O , Ni, and Co in the sodiation process in batteries³³. However, cells show poor sodium kinetics, structural instability and low energy efficiency (as demonstrated by high voltage hysteresis). Among TMO materials, iron oxides, particularly Fe_2O_3 , and Fe_3O_4 are more promising anode materials for sodium batteries, because they use abundant resources, are low cost, non-toxic and highly resistant to corrosion^{34, 35}. Chen and co-workers synthesized a 3D porous γ - Fe_3O_4/C nanocomposite by an aerogel-assisted method. It showed good reversible capacity of 740 mAhg^{-1} for 200 cycles at a 200 mA g^{-1} current rates for high-performance anode material for sodium batteries³⁶. Wang et al. synthesized a porous Co_3O_4 / N-doped Carbon composite with a MOF (Metal Organic Framework) nanostructure by templating around ZIF-67. This material showed excellent specific capacities of 506 mAhg^{-1} at 100 mA g^{-1} and 263 mAhg^{-1} at 1 Ag^{-1} for 1000 cycles with only 0.01% capacity loss for each cycle in sodium batteries³⁷. Liu et al. proposed transition metal chalcogenide FeS_2/C with a yolk-shell nanostructure as a conversion-reaction based anode material. This material was synthesized by a facile method involving etching, followed by “sulfidation-in-nano box”. The material exhibited specific capacities of 511 mAhg^{-1} at 100 mA g^{-1} and 330 mAhg^{-1} at 2 Ag^{-1} for 800 cycles with ultra long cycling stability, and appears suitable for high rate capability sodium batteries³⁸. Chen et al. prepared a MOF-structured anode by combining an N-doped carbon nanostructure host with ultrathin MoS_2 nanosheets, grown within the host by a hydrothermal method. This material showed good reversible

specific capacities of 660 mAhg⁻¹ at 100 mA g⁻¹ and 306 mAhg⁻¹ at 1 Ag⁻¹ for 1000 cycles with excellent rate capacity and long cycling life³⁹. Similar hybrid, layered TMC materials, such as VS₂ and WS₂ have been proposed as anode materials for sodium batteries⁴⁰.

1.5.2 Cathode materials:

In sodium-ion batteries, the cathode material acts as the initial sodium source and sodium ions are transported from the cathode to anode material (generally a “hard” carbon) when the battery is charged. During the discharge process, sodium ions return to the cathode. Cathode materials are categorized based on their crystal structure.

1.5.2.1 Oxide compounds:

Layered transition-metal oxide (TMO) materials are promising cathode materials for high energy density sodium-ion batteries. After commercialization of the lithium-ion battery with a LiCoO₂ cathode, initial studies were pursued on single, and multiple TMO cathode materials for sodium-ion batteries. Sodium ions can be inserted and removed from many 3d transition-metal (Mn, V, Ni, Fe, Ti, Co, Cr) oxides, as shown in Figure 1.5.

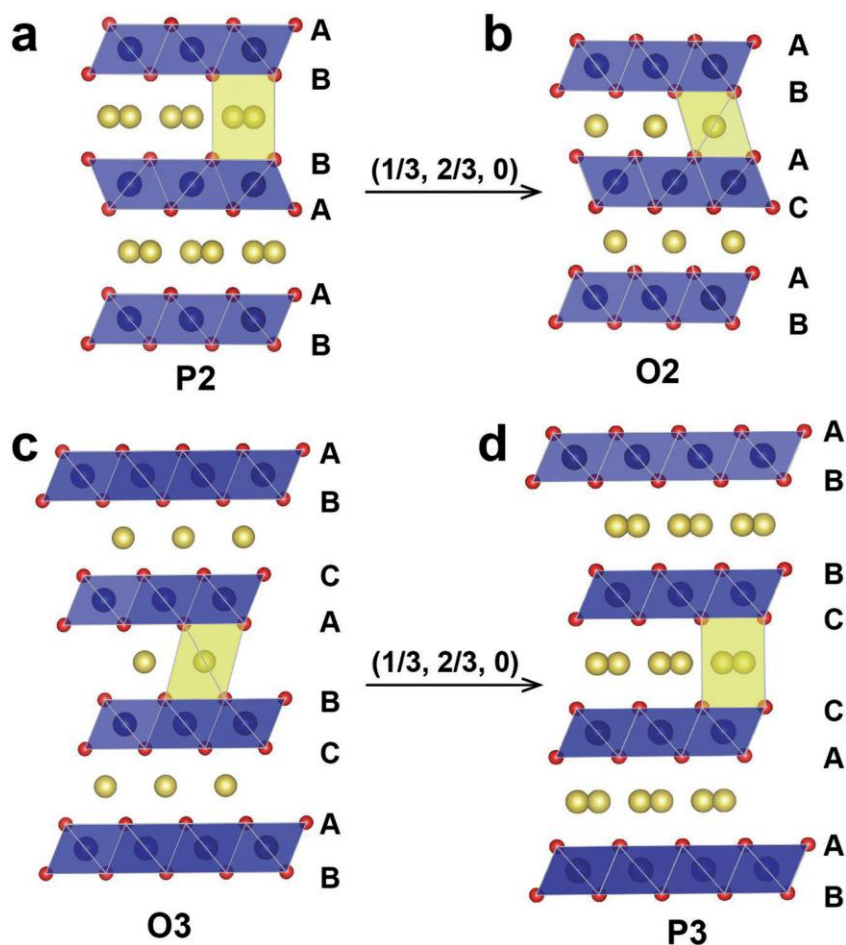


Figure 1. 8: Sodium host layered oxide (Na_xTMO₂) schematic crystal structures for a) P2-type, b) O2-type, c) O3-type, and d) P3-type stacking cathode materials for sodium-ion batteries. In the crystal structure, blue and yellow balls represent the transition-metal and Na ions in the O-type frameworks⁴¹.

Manganese-based layered oxides are of particular research interest because they are non-toxic, inexpensive, and have more sites in their structures which can accommodate sodium ions. These materials have an orthorhombic structure; the unit cell includes MnO₅ square pyramids and MnO₆ octahedra, which are organized to form two types of tunnels; large S-shaped tunnels and smaller pentagon tunnels. There are three Na-sites: Na₁ site is within a small tunnel, and is occupied completely; the other sites, Na₂ and Na₃, are half occupied in the large S-shaped tunnel and are sites for “reversible” electrochemical reactions in a sodium-ion battery. This material shows a theoretical capacity is 121 mAhg⁻¹ based on two sodium transfer (Na₂ and Na₃) in large S-shaped tunnels sites in the material structure. Cao et al. synthesized the Na₄Mn₉O₁₈ cathode material with nanowire morphology by a polymer-pyrolysis process and

found a high reversible capacity (128 mAhg^{-1}), excellent rate capability and long cycling stability for a high-performance sodium-ion battery⁴². Delmas et al. were the first to report the P2 and O3 type NaCoO_2 material electrochemical studies. P2 phase NaCoO_2 material shows excellent electrochemical performance, good structural stability and high reversible capacity as compared to other types of sodium-ion battery⁴³. Yu et al. synthesized carbon-coated NaCrO_2 cathode material, which also showed excellent electrochemical performance for sodium-ion battery applications⁷. This material delivered an initial discharge capacity of about $100\text{--}110 \text{ mAhg}^{-1}$ (based on 0.5 mol of Na^+) related to $\text{Cr}^{3+}/\text{Cr}^{4+}$ redox couple with good rate capability up to 150 C-rate. While the above cathode materials showed good electrochemical performance, they have some drawbacks, mostly related to instability (either in contact with air, or as a result of phase transitions, or major volume changes during intercalation). To overcome such above issues, $\text{NaNi}_{1/3}\text{Fe}_{1/3}\text{Mn}_{1/3}\text{O}_2$ ⁴⁴, $\text{Na}_{0.9}\text{Cu}_{0.22}\text{Fe}_{0.30}\text{Mn}_{0.48}\text{O}_2$ ⁴⁵, and $\text{NaNi}_{0.5}\text{Mn}_{0.2}\text{Ti}_{0.3}\text{O}_2$ ⁴⁶ layered TMOs are more promising for practical, commercial sodium-ion batteries.

Wang et al. successfully synthesized $\text{NaNi}_{1/3}\text{Fe}_{1/3}\text{Mn}_{1/3}\text{O}_2$ cathode material by a large-scale process combining hydroxide co-precipitation with solid-state reaction⁴⁴. Their cathode showed good reversible capacity of 125 mAhg^{-1} at a 1C rate for 500 cycles, this also demonstrated its good rate capability and long-term cycling stability. Li et al. synthesized $\text{Na}_{0.9}\text{Cu}_{0.22}\text{Fe}_{0.30}\text{Mn}_{0.48}\text{O}_2$ cathode material by solid-state reaction⁴⁵. This material exhibited a reversible capacity of 89 mAhg^{-1} at a 0.1C rate and good rate capability with capacity retention of 85% for 150 cycles at a 1C rate. Wang et al. also synthesized the $\text{NaNi}_{0.5}\text{Mn}_{0.2}\text{Ti}_{0.3}\text{O}_2$ cathode material by conventional solid-state reaction⁴⁶. This material exhibited an initial discharge capacity of 135 mAhg^{-1} with good capacity retention of 85% at a 1C rate for 200 cycles. Above mentioned the three-layered TMO cathode materials ($\text{NaNi}_{1/3}\text{Fe}_{1/3}\text{Mn}_{1/3}\text{O}_2$, $\text{Na}_{0.9}\text{Cu}_{0.22}\text{Fe}_{0.30}\text{Mn}_{0.48}\text{O}_2$, and $\text{NaNi}_{0.5}\text{Mn}_{0.2}\text{Ti}_{0.3}\text{O}_2$) are more reliable to use for commercial application of sodium-ion batteries as compared to other layered materials.

1.5.2.2 Polyanion compound-based cathode material:

Phosphate-(PO₄) based systems have similar structures to that of Na⁺ Super Ionic CONductor (NASICON) compounds, such as Na_{1+x}Zr₂P_{3-x}Si_xO₁₂.

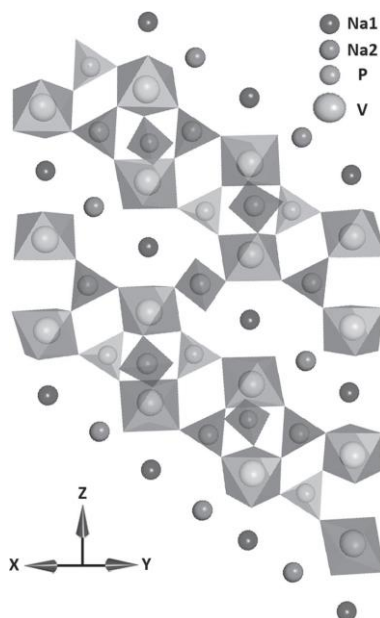


Figure 1. 9: NASICON-type crystal structure of Na₃V₂(PO₄)₃ cathode material⁴⁷.

Na₃V₂(PO₄)₃ is a NASICON-type compound with a 3D rhombohedral framework (symmetry $R\bar{3}c$) consisting of isolated VO₆ octahedra and PO₄ tetrahedra inter connected via corners to form the framework anion [V₂(PO₄)₃]³⁻, and Na occupies two distinct sites within open channels (Figure 1.6). Na₃V₂(PO₄)₃ cathode material has three sodium sources, in that two sodium ions can intercalate through the electrolyte while the charge-discharge process in the sodium-ion battery. Saravanan et al. synthesized a carbon-coated porous Na₃V₂(PO₄)₃ cathode material by a soft template method⁴⁷. This material exhibited excellent electrochemical performance, high rate capability, and good long-term cycling stability with 50% capacity retention at a 40C rate for 30000 cycles in a sodium-ion battery.

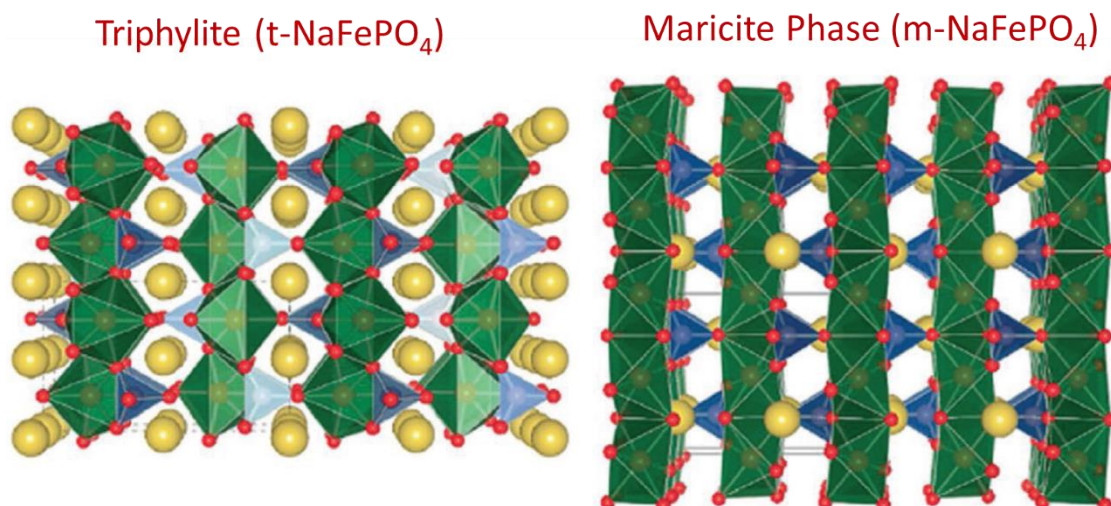


Figure 1. 10: Crystal structures of NaFePO_4 cathode material in Triphylite and Maricite phases for sodium-ion battery, FeO_6 octahedra and PO_4 tetrahedra are shown in green and blue, respectively. Na atoms are shown as yellow spheres⁴⁸.

Olivine-type NaFePO_4 cathode materials may be either triphylite- NaFePO_4 or Maricite- NaFePO_4 phases, as shown in Figure 1.7. Maricite- NaFePO_4 phase was obtained by a simple solid-state reaction method, but this material is not electrochemically active in a sodium-ion battery⁴⁹. Triphylite- NaFePO_4 phase cathode material was synthesized via electrochemical or chemical de-lithiation and subsequent sodium-ion insertion of LiFePO_4 . It has a theoretical capacity value of 154 mAhg^{-1} and shows good reversible capacity of 120 mAhg^{-1} with a two-step voltage profile of $\text{Fe}^{3+}/\text{Fe}^{2+}$ versus. Na/Na^+ .⁵⁰ Pyrophosphate-based sodium host $\text{Na}_2\text{FeP}_2\text{O}_7$ cathode material has been synthesized by solid-state, solution combustion, and gas ceramic routes⁵¹⁻⁵³. This material exhibits an excellent reversible capacity of 85 mAhg^{-1} with one sodium extraction process in sodium-ion batteries. Na-rich $\text{Na}_{3.5}\text{V}_2(\text{PO}_4)_2\text{F}_3$ fluorophosphate compound cathode material was synthesized by simple ball milling of $\text{Na}_3\text{V}_2(\text{PO}_4)_2\text{F}_3$ and Na or Na_3P .⁵⁴ In sodium-ion batteries, NASICON-type $\text{Na}_3\text{V}_2(\text{PO}_4)_3$, pyrophosphate- $\text{Na}_2\text{FeP}_2\text{O}_7$, and fluorophosphate- Na-rich $\text{Na}_{3.5}\text{V}_2(\text{PO}_4)_2\text{F}_3$ cathode materials promising materials for commercial full-cell sodium-ion batteries.

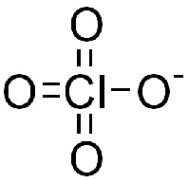
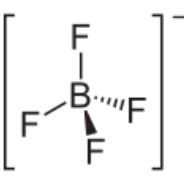
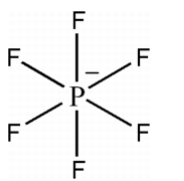
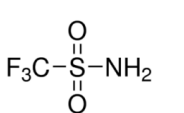
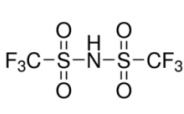
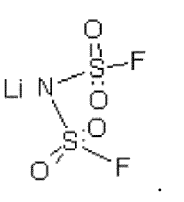
1.5.2.3 Other cathode materials for sodium-ion batteries:

Fluoride-based cathode materials are promising electrodes, which offer higher capacity values as compared to polyanion type cathode materials in sodium-ion battery. Badway et al. reported the carbon-metal fluoride nanocomposite (CMFNC)- based cathode material for sodium-ion battery⁵⁵. This material was synthesized by high energy mechanical ball milling and shows the huge reversible capacity of 200 mAhg⁻¹ with Fe³⁺/Fe²⁺ redox couple over a potential range of 2.8 to 3.5 V versus Na/Na⁺ for 50 cycles, with 10% capacity loss, in sodium batteries. However, the above fluoride-based materials are sensitive to moisture and damage the container of the ball mill. “Sodium host”, NaMF₃ materials were developed as an alternative to avoid the moisture sensitivity and reduce the damage to the ball mill container during mechanical milling. Goecheva et al. successfully synthesized sodium host NaMnF₃, NaNiF₃ and NaFeF₃ cathode materials by mechanical ball milling, and tested these for use in a sodium-ion battery⁵⁶. NaFeF₃ cathode material exhibited an initial discharge capacity of 130 mAhg⁻¹ at 0.2 mAcm⁻² current density with 2.7 V discharge potential against sodium.

1.5.3 Electrolytes:

In batteries, the electrolyte plays a major role by transporting the ions between cathode and anode. In a sodium-ion battery, electrolytes are usually sodium salts dissolved in aqueous or non-aqueous solvents⁵⁷. Some of the sodium salt in the electrolyte can be used as a sodium reservoir. Desirable electrolyte properties include a large potential window, high thermal stability, high chemical stability, being non-flammable, high ionic conductivity, and that the electrolyte forms a stable solid electrolyte interface when cycled in a sodium-ion battery.

Table 1. 2: Structures and properties of sodium salts used in sodium-ion battery electrolytes⁵⁸.

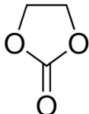
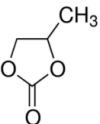
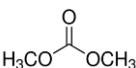
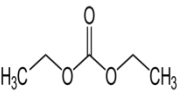
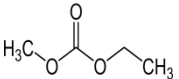
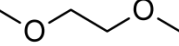
Salt	Anion Structure	M _w (g mol ⁻¹)	T(°C) (Li-salt)	σ(mS cm ⁻¹) (Li-salt)
NaClO ₄		122.4	468 (236)	6.4 (5.6)
NaBF ₄		109.8	384 (293)	(3.4)
NaPF ₆		167.9	300(200)	7.98 (5.8)
NaTf		172.1	248 (>300)	(1.7)
NaTFSI		303.1	257 (234)	6.2 (5.1)
NaFSI		203.3	118 (130)	--

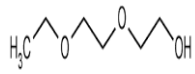
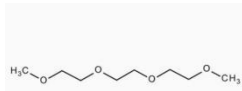
1.5.3.1 Conventional electrolytes for Sodium-ion batteries:

In sodium-ion batteries, organic-solvent based electrolytes are proposed for use with various cathode and anode materials systems. Most sodium-ion battery electrolytes contain sodium salts (such as NaClO₄, NaPF₆, NaFSI, NaTFSI or NaBF₄) dissolved in single molecule organic

solvents (PC), or in binary (EC-PC, EC-DEC, EC-DMC, and EC-EMC), or ternary (EC-PC-DMC)⁵⁹ mixtures of organic solvents, as listed in Table 1.2 and Table 1.3. The binary solvent mixtures are most widely used.

Table 1. 3: Chemical structures and properties of organic solvents used in sodium-ion battery electrolytes⁵⁸.

Solvent	T _m (°C)	T _b (°C)	T _f (°C)	η (cP) 25 °C	ε 25 °C	AN (DN)
 Ethylene Carbonate(EC)	36.4	248	160	1.9(40°C)	89.78	(16.4)
 Propylene carbonate(PC)	-48.8	242	132	2.53	64.92	18.3 (15.1)
 Di methyl carbonate (DMC)	4.6	91	18	0.59	3.107	
 Di ethyl carbonate (DEC)	-74.3	126	31	0.75	2.805	(16.0)
 Ethyl methyl carbonate (EMC)	-53	110		0.65	2.958	
 Dimethoxyethane (DME)	-58	84	0	0.46	7.18	10.9 (18.6)

 Diethyleneglycol dimethylether (Diglyme)	-64	162	57	1.06	7.4	9.9(19.2)
 Triethylene glycol dimethylether (Triglyme)	-46	216	111	3.39	7.53	10.5(14)

In a comparison study, Ponrouch et al. prepared different binary organic-solvent based electrolytes and tested their thermal stability, potential window, ionic conductivity and cycling feasibility properties for sodium-ion batteries. They recommended electrolytes consisting of EC-PC binary organic solvent with 1M NaClO₄ or 1M NaPF₆ as a good choice for sodium-ion batteries⁵⁷. These electrolytes were then studied with various cathode and anode materials in sodium batteries. The same research group proposed another electrolyte composition consisting of ternary organic solvent ((EC-PC-DMC) (0.45:0.45:0.1) v/v) with 1M NaClO₄ salt, and showed that this electrolyte has high ionic conductivity with low viscosity, low ion pairing and forms a stable SEI layer on electrode surfaces in sodium-ion batteries⁶⁰. Sankaranarayanan and co-workers studied the electrochemical performance of TiO₂ anode material with 1M NaClO₄ salt dissolved in different single and binary organic solvents for sodium-ion batteries⁶¹. Above literature studies concluded that EC-DMC and EC-EMC binary organic solvent electrolytes show better capacity retention, and high rate capability with stable SEI layer formation on electrode surfaces as compared to EC-DEC electrolytes for sodium-ion batteries.

1.5.3.2 Co-intercalating electrolytes for Sodium-ion batteries:

Conventional electrolytes do not participate in the sodium-ion storage process, and do not help

transport the sodium ions from the electrode surfaces into the storage sites within the electrode material (carbon, alloying or intercalated material). Instead, the sodium ion de-solvates from the electrolyte solvent, and transports to the storage sites by solid-state diffusion. In contrast, for co-intercalating electrolytes, the sodium ion doesn't completely de-solvate from the electrolyte solvent molecules, and these solvent molecules participate directly in the sodium-ion storage process.

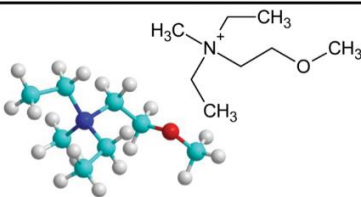

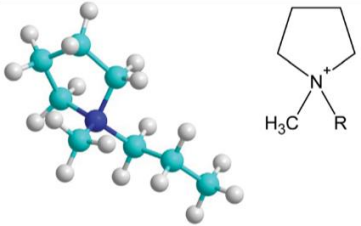
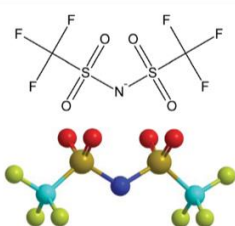
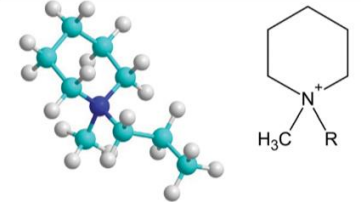
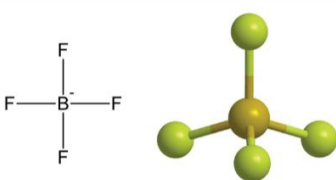
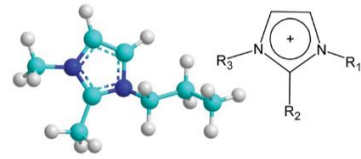
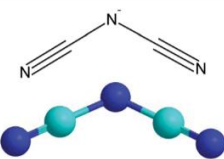
Adelhelm and co-workers closely examined intercalation of a graphite anode material by sodium ions from a 1M NaFSI in diglyme electrolyte⁶². Their x-ray diffraction (XRD) studies revealed significant increases in the d-spacing in the graphite anode material when the sodium intercalated – implying that diglyme had also been intercalated. The same research group then studied different solvents (triglyme, tetraglyme, di(propylene glycol)methyl ether, diethylene glycol dibutyl ether (Butyl-2G), and 1,5-dimethoxypentane (1,5-DMP))-based electrolytes, examining their electrochemical performance with graphite anodes in sodium-ion batteries⁶³. Kang and co-workers found good electrochemical performance of graphite with NaPF₆/diglyme electrolytes for sodium-ion batteries⁶⁴. Tarascon and co-workers explored a diglyme-based electrolyte with a Sn anode material for sodium-ion batteries⁶⁵, and found an excellent electrochemical performance with good capacity retention and extended cycling stability.

1.5.3.3 Ionic-liquid based electrolytes for sodium-ion batteries:

Organic electrolytes have problems associated with their high flammability and low thermal stability, which means that they can catch fire, particularly when sodium-metal dendrites form within the batteries. These problems can be overcome by using ionic liquids (ILs, which are far safer, since they are more thermally stable, non-flammable, and far less volatile) as solvents in the electrolytes. Such batteries may need to operate at higher temperatures to achieve excellent battery performance, because of the lower conductivity of IL-based electrolytes.

IL-based electrolytes have been proposed to enhance battery safety, and have been extensively studied for lithium-ion batteries over the past few years.⁶⁶⁻⁷⁰ Some work suggests that ILs may also be suitable electrolytes for sodium-ion batteries.⁷¹⁻⁷⁶ In particular, pyrrolidinium-based ILs display a large electrochemical window and good cycling stability with sodium.^{72, 73, 75} For example, 1-methyl 1-propyl pyrrolidinium bis (fluorosulfonyl)imide (C₃mpyrFSI) has been used as an electrolyte with hard carbon and NaCrO₂ electrodes and cycled for 500 times in a sodium-ion battery.⁷⁴ Imidazolium-based ILs have also been used as electrolytes for different sodium-ion battery systems, but the acidic proton on the imidazolium ring leads to decomposition of the electrolyte at relatively high voltages.⁷⁷⁻⁸¹ Some IL structures are shown in Figure 1.5.

ILs generally display higher viscosity and lower ionic conductivity than those of conventional organic electrolytes at room temperature. Therefore in order to reduce their viscosity, “hybrid electrolytes” — mixtures of IL and organic electrolyte — were developed to improve the electrochemical performance and safety of lithium- and sodium-ion batteries.⁸²⁻⁸⁶

Cations	Anions
 <p><i>N,N</i>-diethyl-<i>N</i>-methyl-<i>N</i>-(2-methoxyethyl) ammonium, [DEME]⁺</p>	 <p>Bis(fluorosulfonyl)imide, [FSI]⁻</p>
 <p><i>N</i>-methyl-<i>N</i>-alkyl pyrrolidinium, [C_nmpyr]⁺</p>	 <p>Bis(trifluoromethanesulfonyl)amide, [NTf₂]⁻</p>
 <p><i>N</i>-methyl-<i>N</i>-alkyl piperidinium, [C_nmpip]⁺</p>	 <p>Tetrafluoroborate, [BF₄]⁻</p>
 <p>1,2-dialkyl methylimidazolium, C_nC_nmim⁺</p>	 <p>Dicyanamide, [dca]⁻</p>

* R groups – typically ethyl, propyl, butyl.

this compound (along with many other nitrogen centred anions) is described as an “amide” in the inorganic literature, but incorrectly as an “imide” in the materials and electrochemical literature. FSI should also be described as an amide (ie FSA) but that is so uncommon in this field that we have retained FSI in this article.

Figure 1. 11: Molecular structures of different IL cations and anions⁸⁷.

1.5.3.4 Aqueous electrolytes:

Aqueous electrolytes showed a significant property such as low cost, high safe, and abundant resources with eco-friendliness. This electrolyte brings the aqueous sodium-ion batteries (ASIB) more attention in the large-scale energy storage applications as compared to other batteries. In ASIB's, Na₂SO₄ salt dissolved in various concentration with deionized water most widely used as an aqueous electrolyte in sodium ion batteries. Whitacre et al constructed the 80V ASIB by using the λ-MnO₂ as a cathode and activated carbon as anode material with 1M Na₂SO₄ aqueous electrolyte. Zhang et al assembled the full cell ASIB' consist of Na_{0.58}MnO₂·0.48H₂O as a cathode, NaTi₂(PO₄)₃ as an anode, and 1M Na₂SO₄/H₂O as an

electrolyte. this battery showed a high rate of performance of 39mAhg^{-1} at a 10C rate with a stable long cycle life of 94% capacity retention for 1000 cycles. In aqueous electrolytes, changing the pH of electrolyte sodium intercalation and deintercalation kinetics improves in the ASIB's. Want et al successfully constructed the full cell of ASIB with promising cathode material of $\text{Na}_{0.66}[\text{Mn}_{0.66}\text{Ti}_{0.34}]\text{O}_2$, and $\text{NaTi}_2(\text{PO}_4)_3/\text{C}$ as anode material with 1M Na_2SO_4 aqueous electrolyte (pH=7). It showed an excellent cycling performance with a specific capacity of 54mAhg^{-1} at the 10C rate for 300 cycles.

1.5.4 Binders for sodium-ion batteries:

The binder plays an important role to enhance the electrochemical performance by ensuring that the active materials are retained on the surfaces of the current collectors as the battery is charged and discharged. Typical sodium-ion battery electrodes include 5-10 wt. % of binders, along with the active material and conductive carbon⁸⁸.

PVDF (Polyvinylidene fluoride) is the most common binder for a wide range of cathode and anode materials. Generally, PVDF binder is dissolved in an *N*-methyl-2-pyrrolidone solvent to and added to the conductive carbon and active material to form an “electrode slurry”, from which electrodes are cast. However, PVDF leads to poor electrochemical performance with capacity fading when used with carbon, insertion, alloying or conversion anode materials in sodium-ion batteries. PVDF binders react with electrolytes to form more SEI layer in the initial cycles, lowering the lower coulombic efficiency of the anode materials in sodium-ion batteries⁸⁹. To overcome such issues in batteries, aqueous binders were introduced, and enhanced the electrochemical performance and cycling stability in sodium-ion batteries. CMC (Carboxy methyl cellulose) and Na-Alginate binders are easily soluble in water and are non-toxic, and have been shown to improve performance of carbon, insertion, alloying and conversion anode materials⁹⁰. PAA (Poly Acrylic Acid) has also been used as a binder for various anode materials, resulting in more stable electrochemical performance in sodium-ion

batteries. Komaba and coworkers used PAA binder in a Sn anode material and found excellent cycling performance, good rate capability and stable SEI formation on the anode surface as compared to the results obtained with PVDF binder in sodium-ion batteries⁹¹. Liu et al. observed significant changes in electrochemical performance of Sn anode material with PFM (poly (9,9-dioctylfluorene-*co*-fluorenone-*co*-methyl benzoic ester) as compared to CMC and PVDF binders for sodium-ion batteries⁹². Sun and co-workers improved the electrochemical performance of conversion type-Fe₂O₃, and NiO anode materials by using CMC binders⁹³.

1.5.5 Current collectors:

Current collectors transfer electrons to the external circuit within the potential window. The working electrodes for sodium-ion batteries are prepared by coating each current collector with an appropriate electrode slurry and drying. Aluminum foil and copper foils are used as cathode and anode current collectors in batteries. Sodium doesn't have an alloying reaction with aluminum foil, so aluminum foil (which is stable across a voltage range of 0 to 5.5 V vs. Na/Na⁺)^{6, 94, 95} can be used as an anodic current collector in sodium-ion batteries. This reduces both the weight and cost of the battery. Copper current collectors have an electrochemical stability range of 0-3 V versus Na/Na⁺. Stainless steel and nickel foam have also been used as current collectors for several anode and cathode materials⁹⁶.

1.5.6 Separators for sodium-ion batteries:

Separators are used to prevent the direct contact of cathode and anode and shorting the batteries. It acts as a porous membrane to passivate the charge carrier ions between the cathode and anode materials in batteries. Battery electrochemistry and their safety depends on thickness, porosity, chemically and electrochemically inert behavior and a melting point of the separator. Most of the sodium-ion batteries have semi-crystalline polyolefin-based polymer such as borosilicate, polypropylene, polyethylene, and solupor are used as separators with the different cathode and

anode materials in batteries^{97, 98}.

1.6 Scope of the work:

Commercialized sodium technologies include a high temperature Na/S cells for MW energy storage and Na-NiCl₂ ZEBRA-type cells for electric vehicles.⁹⁹ Both sodium cells consist a highly conducting beta-alumina ceramic electrolyte, and operate above 300 °C.⁹⁹ Room-temperature sodium-ion batteries are more attractive due to their safety and more reliable than high-temperature batteries.¹⁰⁰⁻¹⁰²

Sodium ions are larger, and diffuse more slowly, than lithium ions.¹⁰³ This presents a tremendous challenge for the development of reversible intercalation electrodes that can deliver charge quickly. Commercialization of sodium on battery research has begun by many companies, including Faradion, Aquion, Samsung, Sharp and Toyota, to produce high energy-density batteries¹⁰⁴⁻¹¹⁰. Rapid progress is occurring in many areas — especially the synthesis of cathode and anode materials^{6, 111}. However, the electrolyte is critical for a high-performance SIB and should provide a wide potential window, be safe and allow consistent, efficient cycling of the electrode materials in batteries.

Aqueous-electrolyte based SIBs are limited by lower power and energy densities, making them unsuitable for large-scale energy storage applications¹¹². Nonaqueous electrolytes are used in high energy-density SIBs. The currently-explored electrolytes consist of a Na⁺ salt (often NaClO₄, NaFSI, NaTFSI, or NaPF₆) in a mixture of organic solvents (such as DEC, DMC, EC, PC, FEC, and EMC)^{58, 113}. Organic electrolytes have some significant drawbacks: low thermal stability, and relatively high volatility and flammability. These issues can become even more important when building large-scale SIBs. To overcome such issues in sodium-ion batteries, ILs are introduced as alternative solvents in the electrolytes.

ILs have physio-chemical properties which make them promising for electrolytes in different battery systems, including high thermal stability, wide potential window, low volatility and

generally high safety^{68, 87}. Imidazolium- and pyrrolidinium-cation based ionic liquids were developed to increase the operating temperature of batteries^{71, 72, 114, 115}. However, the IL electrolytes showed poor cycling performance compared to that obtained with conventional organic electrolytes, due to the high viscosity and low conductivity of ILs. Literature studies show that IL-based electrolytes operated at 90 °C exhibit excellent cycling performance in sodium-ion batteries, in contrast to organic electrolytes, which have lower thermal stability, and do not show stable cycling performance at high temperature⁹⁴. This suggests that the IL would be better from the point of view of safety, but the cost of the batteries would be higher than for conventional organic electrolytes. ILs have high charge-transfer resistance with sodium metal, which means that they do not achieve the performance of organic electrolytes at 25 °C¹¹⁶. This means that appropriate anode materials with sodium reversible electrochemistry are needed instead of sodium metal to avoid the high charge transfer resistance in sodium-ion batteries¹¹⁷.

NVP@C and hard carbon have been used as cathode and anode materials in sodium-ion batteries and studied thoroughly in several reports^{14, 118-123}. This thesis presents the synthesis of a cost-efficient NVP@C cathode material by a simple solid-state reaction. Also included are studies of the physio-chemical properties of organic, hybrid and IL electrolytes in sodium batteries. Compared to organic electrolytes, the hybrid electrolytes showed higher thermal stability, and stable SEI formation on the NVP@C cathode material, suggesting that they are suitable for safer sodium-ion batteries. Full-cell cycling performance tests of sodium-ion batteries with the NVP@C cathode and bio derived hard carbon anodes with organic, hybrid and ionic-liquid based electrolytes were then carried out. The hard carbon anode material has a major problem of initial capacity loss in a sodium-ion battery, because of the thick and uneven solid electrolyte interface (SEI) layer that forms and makes the sodium insertion and removal from the anode material less reversible. This work shows a way of reducing the initial

irreversible capacity loss by short-circuiting the hard carbon with sodium metal for 30 minutes prior to its use in a battery. Thermal decomposition of organic, hybrid and IL electrolytes are studied to understand the decomposition mechanism of electrolytes in sodium batteries.

1.6.1 Outline of thesis:

The present thesis work is structured into 8 chapters, which present an experimental investigation of IL formulation-based electrolytes for sodium-ion batteries, in particular their SEI formation on NVP@C, hard carbon and sodium metal surfaces.

Chapter 1 introduces sodium-ion batteries, their components and reviews literature on electrolytes for sodium-ion batteries and scope of the work.

Chapter 2 introduces the experiment methods and characterization of materials and electrolytes.

Chapter 3 examines the role of N-Propyl-N-Methyl Pyrrolidinium bis(trifluoromethane sulfonyl)imide as an Electrolyte Additive in Sodium Battery Electrochemistry.

Chapter 4 presents a new stability-enhancing IL-hybrid electrolyte for NVP@C cathode-based sodium batteries.

Chapter 5 shows how IL electrolytes support high energy density in sodium-ion batteries based on sodium vanadium phosphate composites (NVP@C).

Chapter 6 investigates the thermal decomposition of organic, hybrid and IL-based electrolytes and also examines the compositions of the SEIs that form on sodium metal when these electrolytes are used in sodium-metal batteries.

Chapter 7 presents a commercially-focused, cost effective full cell sodium-ion battery which uses an almond-shell based hard carbon anode and NVP@C cathode.

Chapter 8 recommends future directions for research into IL-based electrolytes for sodium-ion batteries.

Chapter 2

Experimental and methods

2.1 Chemicals:

2.1.1 Chemical for synthesis:

Ammonium vanadium oxide (NH_4VO_3) (Sigma-Aldrich, India) sodium dihydrogen phosphate dihydrate ($\text{NaH}_2\text{PO}_4 \cdot 2\text{H}_2\text{O}$) (Alfa-Aesar, India), oxalic acid dehydrate (Sigma-Aldrich, India), Vanadium oxide (Sigma-Aldrich, India), Glucose (Sigma-Aldrich, India), Sodium nitrate (NaNO_3) (Sigma Aldrich, India), Diammonium hydrogen phosphate (NH_4)₂HPO₄, Potassium hydroxide (KOH) (Merk, India), Hydrochloric acid (HCl) (Sigma-Aldrich, India), Ethanol ($\text{C}_2\text{H}_5\text{OH}$) (Merk, India).

2.1.2 Chemicals for cell and electrolyte preparation:

Sodium perchlorate (NaClO_4) (Sigma-Aldrich, 99%, India), Sodium bis(fluoromethanesulfonyl)imide (NaFSI) (Solvionic, 99%, France), Sodium bis(trifluoromethanesulfonyl) imide (NaTFSI) (Sigma-Aldrich, 99%, India), N-propyl-N-methyl-pyrrolidinium bis(trifluoromethanesulfonyl)imide ($\text{C}_3\text{mpyrTFSI}$) (Solvionic, 99%, France), N-propyl-N-methyl-pyrrolidinium bis(fluoromethanesulfonyl)imide ($\text{C}_3\text{mpyrFSI}$) (Solvionic, 99%, France), N-butyl-N-methyl-pyrrolidinium bis(trifluoromethanesulfonyl)imide ($\text{C}_4\text{mpyrTFSI}$) (Solvionic, 99%, France), N-butyl-N-methyl-pyrrolidinium bis(fluoromethanesulfonyl)imide ($\text{C}_4\text{mpyrFSI}$) (Solvoinic, 99%, France), Propylene carbonate (PC) (Sigma-Aldrich, 99%, India), Ethylene carbonate (EC) (Sigma-Aldrich, 99%, India), Di methyl carbonate (DMC) (Sigma-Aldrich, 99%, India), Fluoroethylene Carbonate (FEC) (Sigma-Alrich, 99%, India), sodium foil (99%, Alfa Aesar, USA) and borosilicate glass microfiber separator (GF/D) (Whatman, UK).

2.1.3 Chemicals for electrode preparations:

Carbon black (Super C-65, Timcal, Swizerland), polyvinylidene Fluoride (PVDF) (Avg Molecular wt.534000, Sigma-Aldrich, Germany), Sodium salt of carboxymethyl cellulose [CMC] (Sigma-Aldrich, India), N-methyl pyrrolidone [NMP] (C_4H_9NO) (99%, Merk, India), Aluminum foil [Al] (Thickness~15 μ m, MTI, USA).

All the chemical was used as without further treatment in applications. Sodium foil, separator, electrolyte were stored inside the glove box at inert atmosphere and kept moisture and oxygen levels \leq 1ppm.

2.2 Material synthesis:

Sodium vanadium phosphate (NVP) and Hard carbon (HC) material were synthesized from different standard approach to make the cathode and anode material for sodium ion battery.

2.2.1 Synthesis of carbon coated sodium vanadium phosphate (NVP/C):

Sodium vanadium phosphate ($Na_3V_2(PO_4)_3/C$) was synthesized using a carbothermal reduction method, based on the report by Yang *et al.*¹²⁴. In a typical procedure, ammonium vanadium oxide (NH_4VO_3) (Sigma-Aldrich) and sodium dihydrogen phosphate dihydrate ($NaH_2PO_4 \cdot 2H_2O$) (Alfa-Aesar) were mixed together in a 2:3 molar ratio along with 15 wt.% of glucose (Sigma-Aldrich) as the carbon source. The materials were ball milled for 24 h in alcohol. The obtained material was dried at 80 °C in a vacuum oven for 24 h and then calcined at 900 °C for 4 h in a tube furnace under argon.

2.2.2 Synthesis of carbon encapsulated sodium vanadium phosphate (NVP@C):

The NVP@C composite material was synthesized by a two-step, glucose-assisted solid -state reaction. The key to this facile synthesis is the use of oxalic acid to form vanadium oxalate as precursor. Firstly, 0.3 mol oxalic acid dihydrate was dissolved in 50 ml distilled water, and 0.1 mol vanadium oxide powder was added. The solution was stirred at 120°C for 5 hr to form a

sticky blue gel, which was then dried overnight under vacuum at 80°C. The obtained powder was ground and heated at 100°C in air for 1 hr to form vanadium oxalate. In the second step, sodium nitrate, as-prepared vanadium oxalate and diammonium hydrogen phosphate (to give a mole ratio of Na: V: P of 3:2:3) and the 17 wt% of glucose were dispersed in alcohol and ball milled at 300 rpm for 8 hr. The obtained solution was dried overnight under vacuum at 80°C. The obtained powder was ground for 1 hr in a mortar and pestle, and subjected to a two-stage calcination, at 350°C for 5 hr and 850°C for 8 hr in 5% H₂-95% N₂ atmosphere to obtain well-crystallized Na₃V₂(PO₄)₃/C.

2.2.3 Synthesis of composite of sodium vanadium phosphate material (NVP@C):

The NVP@C composite material was synthesized by a simple sonication method. The stoichiometric mole ratio of 3:2:3 precursors of sodium nitrate, vanadium oxide and diammonium hydrogen phosphate and 20 wt% glucose were dispersed in acetone and sonicated for 1hr. The obtained slurry was dried overnight under vacuum at 120°C, ground for 1 hr in a ball mill, and calcined at 800°C for 8 hr in 5% H₂-95% Ar atmosphere to obtain well-crystallized Na₃V₂(PO₄)₃/C.

2.2.4 Synthesis of Bio derived Hard carbon:

Extraction of Lignin from Almond shell by Alkaline-Hydrothermal method:

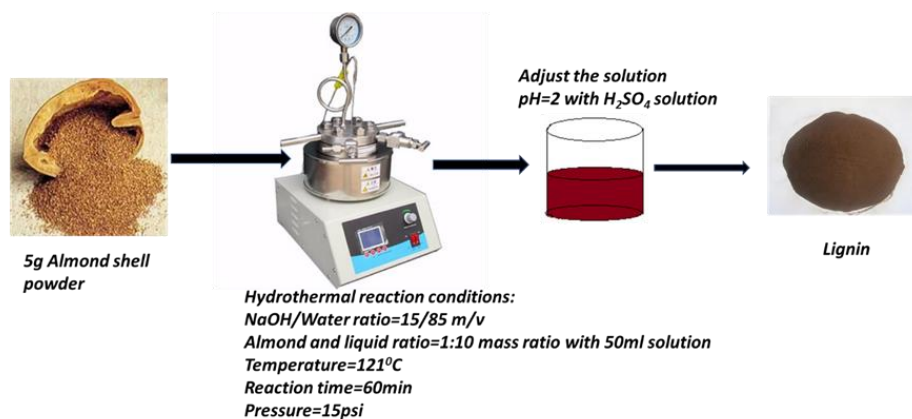


Figure 2. 1: Schematic diagram of lignin extraction process from almond shell.

Pure lignin was extracted from almond shell via a hydrothermally-assisted alkaline extraction method¹²⁵, a detailed procedure is provided in Figure 2.1. The obtained pure lignin was loaded in a tube furnace for the pyrolysis process (1100°C for 1h, heating rate: 5°C min⁻¹) under a flowing nitrogen atmosphere (100 cm³ min⁻¹). The obtained carbon was carefully washed in 20% KOH at 70°C for 2 h and 2 M HCl at 60°C for 15 h to remove the remaining impurities. The purified samples were collected by vacuum filtration after rinsing further with DI water and ethanol until the washing reached a pH value of 7. Then the carbon was dried at 110°C overnight in a vacuum oven. This carbon material was then activated at 300°C for 3 h (at a heating rate of 5°C min⁻¹ in the tube furnace) in a dry air flow of 50 cm³ min⁻¹. The obtained activated hard carbon was first ground and then washed with 2M HCl and DI water again before use.

2.3 Preparation of organic, additive, hybrid and ionic liquid electrolytes:

2.3.1 Organic electrolytes:

1.0 M NaFSI (99%, Solv ionic, France) or 1.0 M NaClO₄ (99%, Sigma Aldrich, India) were dissolved in 1:1, by volume, ethylene carbonate/propylene carbonate (EC: PC) (Sigma Aldrich, India).

2.3.2 Additive electrolyte:

N-propyl-N-methyl pyrrolidinium bis(trifluoromethanesulfonyl)imide ([C₃mpyr] [NTf₂]) IL was purchased from Solv ionic, France. The typical electrolyte composition employed in the current study was 1M sodium perchlorate (NaClO₄) in propylene carbonate (PC) solvent with 0, 3, 5, 7, 9, or 12 wt% IL added.

2.3.3 Hybrid electrolytes:

1.0 M NaFSI (99%, Solv ionic, France) was dissolved in a mixture of 50 vol.% ionic liquid (either C₃mpyrTFSI, C₃mpyrFSI, C₄mpyrTFSI or C₄mpyrFSI) (99%, Solv ionic, France) and

50 vol.% ethylene carbonate/propylene carbonate (EC/PC) (Sigma Aldrich, India). The volume ratio of EC and PC was 1:1.

2.3.4 Ionic liquid electrolytes:

1.0 M NaFSI (99%, Solv ionic, France) was dissolved in ionic liquid (C₃mpyrFSI or C₄mpyrFSI) (99%, Solv ionic, France).

All electrolyte preparation was carried out inside an argon-filled glove box. All hybrid electrolyte formulations are listed in Table 2.1.

Table 2. 1 : Organic, hybrid and ionic liquid electrolyte compositions.

S.No	Electrolyte Compositions	Sample Name
1	1M NaClO ₄ in EC:PC (50:50) v/v	Organic-NaClO ₄
2	1M NaFSI in EC:PC (50:50) v/v	Organic- NaFSI
3	1M NaFSI in EC:PC:P13TFSI(50:50)V/V	Hybrid-OG-C ₃ mpyrTFSI
4	1M NaFSI in EC:PC:P13FSI(50:50)V/V	Hybrid-OG-C ₃ mpyrFSI
5	1M NaFSI in EC:PC:P14TFSI(50:50)V/V	Hybrid-OG-C ₄ mpyrTFSI
6	1M NAFSI IN EC:PC:P14FSI(50:50)V/V	Hybrid-OG-C ₄ mpyrFSI
7	1M NAFSI IN P13FSI	IL-C ₃ mpyrFSI
8	1M NAFSI IN P14FSI	IL-C ₄ mpyrFSI

2.4. Materials Characterization:

2.4.1 X-ray diffraction analysis:

X-ray diffraction technique used to find the new material phase by incident of x-rays on samples and occurs a constructive interference in crystal material. It obeys the Bragg's law.

$$n\lambda = 2d \sin\theta \quad (2.1)$$

Where, n is the integer, λ is the wavelength, d is the distance between equivalent of atoms plans and θ is the angle between incident beam and these planes. The sample phase analysis and structural determination carried out by Rigaku X-ray diffraction with Cu-K α radiation at 40 kV

and 40 mA. The X-ray data were collected within the range of 2θ from 10° to 80° with scan rate of $0.5^\circ/\text{min}$ and dwell time of 0.02sec. In this thesis, X-ray diffraction (XRD) structural analysis fitted by ICSD standard database.

2.4.2 Scanning electron microscopy:

Scanning electron microscopy is technique in which topographical images of solid sample were obtained by scanning the sample's surface with a focused high energy electron beam. Surface images of samples were created by detecting the secondary electrons emitted. Field emission gun scanning electron microscopy (FEG-SEM, JSM-7600F, and Carl-Zeiss, Ultra-55) with energy dispersive X-ray spectroscopy (EDX) was used to study the microstructure and passivation layers on the electrode surfaces in this thesis. Samples were stick on the carbon tape and removed the free particles by purge of N_2 gas on tape. Further, we collected the images with best operating conditions.

2.4.3 Transmission electron microscopy:

Transmission electron microscopy is microscope technique and it passes the high energy beam of electrons through the ultra-thin specimen. Final images were created by interaction of the electrons through the specimen. TEM technique is capable to catch the high-resolution images and examine the fine details in single column atoms.

Microstructural analysis of synthesis samples were performed with a field emission transmission electron microscope (FE-TEM, JEOL, 2100F) in this thesis. TEM samples were prepared by dispersing a small quantity of solid powder in acetone and put the drop of dispersed sample on copper grid for the TEM analysis.

2.4.4. Fourier transform infrared spectroscopy (FT-IR):

Fourier transform infrared spectroscopy is technique which is used to obtain the infrared

spectrum of absorption or emission of solid, liquid and gas. ATR-FTIR analysis was carried out Argon-filled glove box on a Cary 640 FTIR spectrometer, Agilent. Powder samples were made into pellet in the KBr measurement for FTIR analysis throughout in this thesis. Thin films were performed through the ATR mode for our samples. SEI layer studies were performed on electrode surfaces by using the ATR-FTIR instrument and maintained inert atmosphere in the Argon filled glove box.

2.4.5 Thermogravimetric analysis (TGA):

Thermogravimetric analysis is technique to study the change of material phase in chemical and physical properties as a function of increasing temperature or function of increasing time with constant temperature. The sample was placed in alumina crucible, and heated in the furnace from 50 to 550 °C at 10 °C/min in TG analyzer (STA 8000, PerkinElmer) with N₂ purging.

2.4.6 Thermogravimetric analysis- Infrared (TGA-IR):

TGA-IR was performed to analyze the gaseous products of thermal decomposition of organic, hybrid, and ionic liquid electrolytes. The sample was placed in alumina crucible, and heated in the furnace of the TG analyzer (STA 8000, PerkinElmer) with N₂ purging. The exhausted gas was routed into a Frontier infrared spectrometer (FT-IR) by a heated transfer line. The temperature of the transfer line and gas cell in FT-IR were kept at 250 °C. Samples were heated from 50 to 550 °C at 10 °C/min. The FT-IR spectra were obtained by MCT detector (32 scans per each spectrum with 4 cm⁻¹ resolution).

2.5 Electrode and cell fabrication:

Electrodes were fabricated by making a slurry of NVP/C composite with Super P-65 conductive carbon (Timcal, Switzerland) and polyvinylidene fluoride (PVdF, Sigma-Aldrich) binder in NMP (N-Methyl-2-pyrrolidinone) solvent at a weight ratio of 75:15:10 [active material: conductive carbon: binder]. The mixed slurry was cast on Al foil by a doctor blade

technique and dried at 80 °C for 24 h under vacuum. The dried foil was cut into circular disks and used as working electrodes (active material mass loading is $\sim 2.5 \text{ mg/cm}^2$). Coin cells (C2032) were assembled in a NVP/C || Electrolyte || Na-metal configuration. Sodium-metal foil was used as both reference and counter electrodes, borosilicate glass fiber (GF/D) as the separator, and the electrolyte was 1M NaClO₄ dissolved in PC+(0–12 wt%) [C₃mpyr][NTf₂]. Electrodes were fabricated by making the slurry of NVP@C as 80% active material, 10% carbon (carbon black, C-65, Timcal), and 10% PVDF (Sigma–Aldrich) binder were blended with N-methyl-2-pyrrolidone solvent and cast onto aluminum foil. The solvent was removed under vacuum in an oven at 120 °C overnight, and the electrode was cut into circular discs (10 mm or 12 mm diameter, loading mass $\sim 1.12 \text{ mg}$) for further use. To prepare the hard carbon electrode slurry, 80% commercial active material (Kuraha, China), 10% carbon (carbon black, C-65, Timcal), and 10% CMC (Sigma-Aldrich) binder, by mass, were blended with distilled water and cast onto aluminum foil. The solvent was removed under vacuum in an oven at 120 °C overnight, and the electrode cut into circular discs (10 mm or 12 mm diameter) for further use. Above mentioned method followed for whole thesis for electrode fabrication for cathode and anode materials.

Sodiation of Hard carbon electrode experiment was performed by contacting the sodium metal for 30 minutes by wetting both electrodes with ionic liquid electrolyte; the experimental setup is shown in Figure 2.2

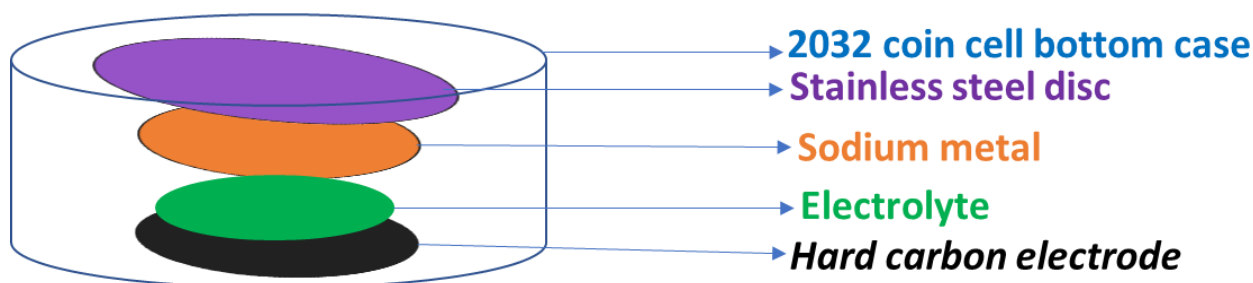


Figure 2. 2: Experimental setup of sodiation of hard carbon electrode by sodium metal with ionic liquid electrolyte.

2.6 Electro chemical characterization:

All assembled cells were characterized by using various electrochemical techniques - such as cyclic voltammetry, galvanostatic charge-discharge cycling, and electrochemical impedance spectroscopy. All electrochemical tests were carried out at $20^{\circ}\text{C} \pm 5^{\circ}\text{C}$.

2.6.1 Cyclic voltammetry:

Cyclic voltammetry is a technique to measure the current and voltage of the working electrode materials with reference electrode and counter electrodes in electro chemical cells. This technique gives the information of electro chemical reaction mechanism by doing the linear scan with potential limit of the cells. Results were plotted as voltage versus current to characterize working potential limits with produced currents of electrode materials. In this thesis, we have used VMP-3 potentiostat biologic instrument to do the cyclic voltammetry for half-cell and full cells to record the current and voltage data with EC-lab interface. Electrochemical stability window tests were performed in a three-electrode Swagelok cell using Na as the counter and reference electrodes and aluminium foil as the working electrodes in same instrument and technique.

2.6.2 Galvanometric charge-discharge cycling:

Galvanometric charge-discharge cycling technique is used to measure the capacity and life of the electrochemical cells. In this technique, constant current with constant voltage mode is used to do the charge and discharge cycling process in batteries. It gives the data in terms of capacity versus potential, cycle life versus capacity, and potential versus time. In this thesis, we performed the half cell and full cell galvanometric charge-discharge cycling in the range of C-rate of 0.02C to 10C with Arbin instrument. Plating and stripping reaction studies were performed in the same instrument by using constant current and constant voltage with 0.1mAcm^{-2} current density. Na|Na symmetrical cell experiments were performed with organic, hybrid and ionic liquid electrolytes at current density of 0.1mAcm^{-2} for 30 minutes of stripping

and plating reaction for each cycle for 100 cycles. To find the sodium deposition and dissolution of sodium to form the passivation film on the sodium metal surfaces.

2.6.3 Electrochemical impedance spectroscopy:

Electrochemical impedance spectroscopy is an important technique to find the electrochemical cell reaction kinetics, electrolyte reactions with electrode, separator reaction with ionic mobility studies, diffusion kinetics and thermodynamics of batteries. AC impedance (Z) contains a real part and imaginary part at given frequency.

$$Z = Z_{\text{Re}} - i Z_{\text{Im}} \quad (2.2)$$

EIS data's were extracted and plotted in the form of the Nyquist plot. In the plot, X-axis refers to Z_{re} and Y-axis refers to Z_{im} . In this thesis, we have used VMP-3 Biologic instrument to record the EIS spectrum in potentiostatic mode within the range of 1MHz to 100 mHz with amplitude of 10mV. In-situ EIS technique were performed and extracted the EIS spectrum in same instrument without interfering the cell by doing the charge and discharge cycling. EIS spectrum fitted in Randle's circuit by Z-fit analysis in EC- lab software.

2.7 AC Impedance Ionic conductivity:

AC-Impedance ionic conductivity is a technique to measure the ionic conductivity of electrolytes of organic, hybrid and pure ionic liquid by the dip cell method. In this thesis, we have measured the ionic conductivity of electrolytes with increasing the temperature from 20°C to 85°C in AC impedance in Biologic instrument.

2.8 Viscosity Measurement:

Viscosities were measured using a rolling ball viscometer (Anton Paar Lovis 2000ME) from 20°C to 90°C using 10°C interval steps, a 10mm long capillary with a diameter of 2.5 mm and a tilting angle of 60°(θ).

Chapter 3

Role of N-Propyl-N-Methyl Pyrrolidinium bis (trifluoro methanesulfonyl) imide as an Electrolyte Additive in Sodium Battery Electrochemistry

3.1 Introduction

Most current research targets suitable cathode and anode materials that operate via a rocking-chair mechanism, similar to that used in current lithium-ion technology^{126, 127}. However, there are few reports on electrolyte optimization, and most of these examine sodium perchlorate-alkyl carbonate-based non-aqueous electrolytes. In these electrolytes, successful operation is possible because a suitable solid electrolyte interphase (SEI) or surface passivation film forms^{59, 128, 129}. According to the literature, the passivation film should be electronically insulating, control electrolyte degradation and exhibit high stability with electrolytes at the electrode-electrolyte interface in batteries¹³⁰⁻¹³². Since these SEI layers are formed by the reaction of organic carbonate-based electrolytes on the surface of the electrodes, the electrolyte composition affects ionic conductivity and SEI layer thickness, and thus battery performance¹³³⁻¹³⁵.

Usually, additives control SEI formation and chemical stability in liquid electrolytes in batteries¹³⁶. Various additives, including ionic liquids (ILs), have been studied for lithium-ion battery electrolytes^{57, 137-140}. As neat electrolytes, ILs can offer advantages such as high thermal stability, high electrochemical stability, excellent ionic conductivity, and a wide liquid temperature range, and are generally eco-friendly^{95, 103, 141-146}. A small addition of IL to an organic electrolyte changes the electrochemical performance, and can control the side reactions of the electrolyte on the cathode surface in lithium-ion batteries¹⁴⁷.

Here, we report the use of [C₃mpyr] [NTf₂] as an electrolyte additive in sodium-based organic electrolytes to enhance the performance of sodium vanadium phosphate (Na₃V₂(PO₄)₃)/C

(NVP/C) cathodes, synthesized via a carbothermal reduction process. The electrochemical performance of NVP/C was systematically evaluated in both “organic electrolyte”, 1 M NaClO₄ in propylene carbonate (PC), and in organic electrolyte with various additions of IL. We found that adding 5 wt % [C₃mpyr] [NTf₂] to the organic electrolyte (“organic + IL”) led to better performance, with higher coulombic efficiency and electrochemical stability compared to that seen with the base organic electrolyte. The SEI layer was characterized by electrochemical impedance spectroscopy, surface analysis using XPS (X-ray photoelectron spectroscopy), and microscopy (FEG-SEM-EDX and FEG-TEM) to understand the role of the IL in the surface film formation.

3.2 NVP/C characterization:

Figure 3.1a shows the XRD pattern of the NVP/C composite material after calcining. The XRD pattern matched the standard data (ICSD No- 248140), corresponding to a R- $\overline{3}C$ space group, indicating the formation of NASICON-type NVP.

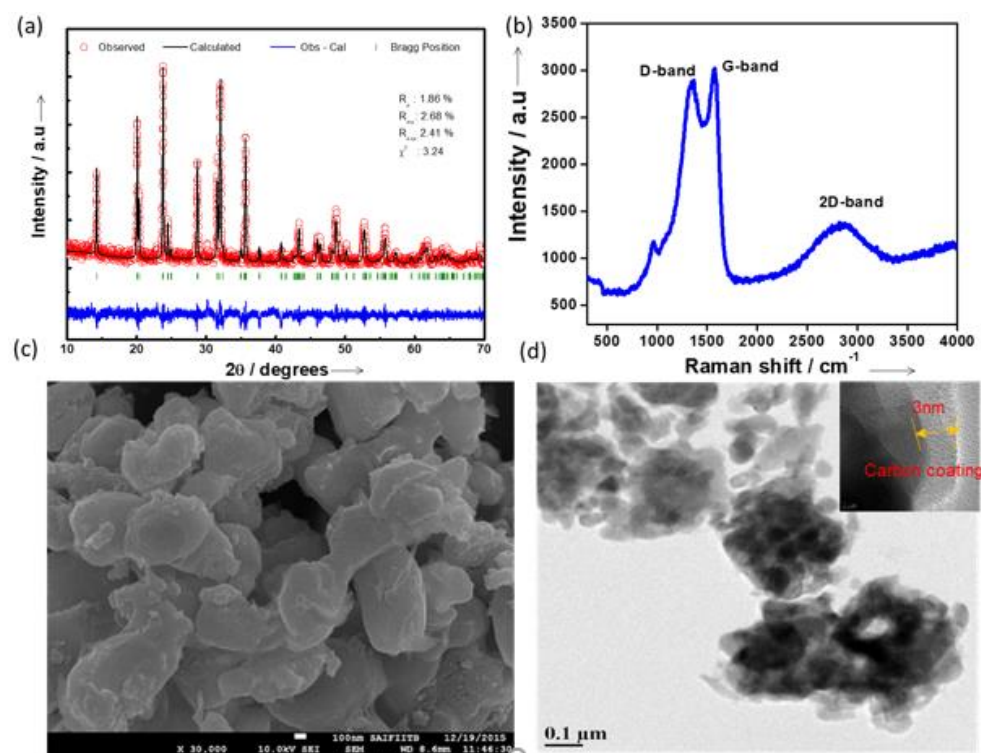


Figure 3. 1:NVP/C characterization. (a) Powder XRD pattern, (b) Raman spectrum, (c) FEG-SEM image, and (d) HR-TEM images.

A dispersive Raman spectrum (Figure 3.1b) confirmed the presence of the carbon coating; the carbon D band around 1346 cm^{-1} and G-band around 1583 cm^{-1} are clearly apparent. Figure 3.1c shows a FEG-SEM (Field Emission Gun-Scanning Electron Microscope) image of NVP/C; the average particle size is around $1\text{ }\mu\text{m}$, but the particles are agglomerated and non-uniform, as a result of the high-temperature calcination. Figure 3.1d shows the HR-TEM (High Resolution-Transmission Electron Microscope) image of NVP/C, and the inset indicates that there is a uniform amorphous carbon layer, around 3 nm thick, on the NVP/C particles. This is consistent with the elemental analysis, which found that NVP/C contains 7.5wt% carbon.

3.3 NVP/C cathode material comparison with previous studies:

As per the literature, NVP/C cathode material has previously been synthesized by an electro-spinning technique, and exhibited a capacity retention of 95.2% after 50 cycles at 0.2C rate¹⁴⁸. This electrode material showed lower capacity values during initial cycles, due to irreversible loss of sodium from the anode side and SEI formation on the electrode surface, which eventually stabilized the cycling performance, meaning that the capacity values were increased in subsequent cycles.¹⁴⁸ Yang *et al.* also synthesized NVP/C cathode material by using a self-combustion technique, and reported initial charge-discharge capacity values of 111.3 mAhg^{-1} and 100.7 mAhg^{-1} at 0.1C rate with 1M NaClO_4 in PC electrolyte¹⁴⁹. In their work, 25% glucose content was used to increase the cycling performance and to make the NVP/C material more stable in organic electrolyte¹⁴⁹. The organic electrolytes reacted with the carbon component in the cathode material to form a thicker SEI layer during the initial cycles, This effect was also seen in other batteries.¹²⁴.

3.4 Organic and additive electrolyte electrochemical performance with NVP/C and Na metal:

The electrochemical characterization of our NVP/C was performed over a potential window of 3 to 3.8 V (vs. Na/Na^+), at a scan rate of 0.1 mVs^{-1} , in both organic and organic + IL electrolytes,

as shown in Figure 3.2a. The vanadium redox couple (V^{3+}/V^{4+}) occurs between 3 to 3.8 V vs Na/Na^+ and showed excellent reversibility with respect to Na insertion/de-insertion reactions ($Na_3V_2(PO_4)_3/C \leftrightarrow NaV_2(PO_4)_3/C$). The peak positions in the organic electrolyte are similar to those reported by Yang¹²⁴. Charge-discharge cycling tests at different C-rates in both organic and organic + IL electrolytes are shown in Figure 3.2b. Adding IL to the electrolyte led to higher capacity for the NVP/C at all rates examined. This may be attributed to suppression of electrolyte degradation and formation of a more stable passivation layer on the electrode material in the presence of ionic liquid in the organic + IL electrolyte, as observed in other battery systems and explained below;¹⁵⁰⁻¹⁵² notably the capacity decreased sharply over the first 3 cycles in the organic electrolyte before stabilizing.

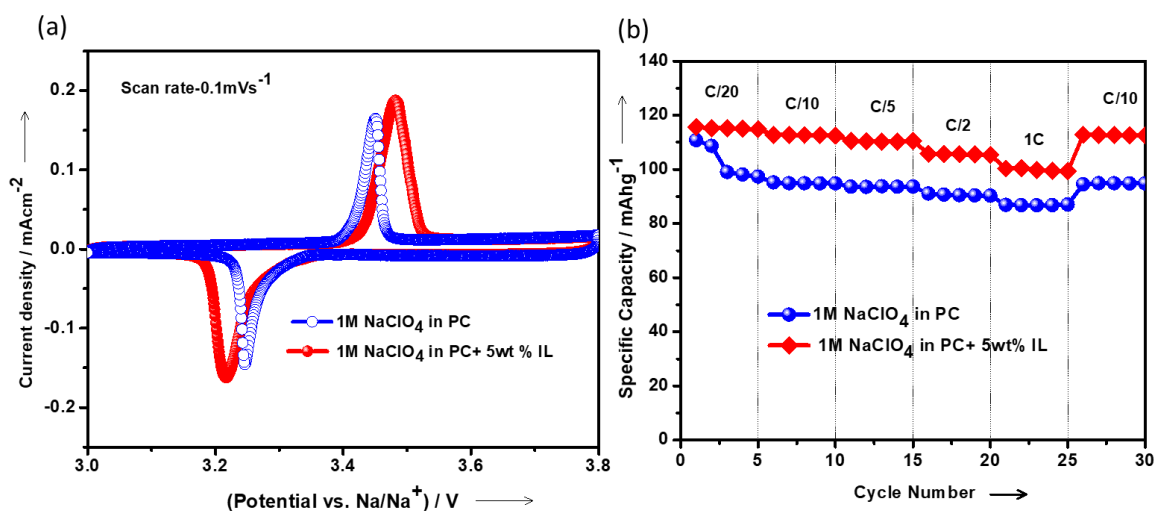


Figure 3. 2:(a) CV curves for NVP/C, (b) Cycling performance of NVP/C at various C-rates with organic and organic+IL electrolytes.

Figure 3.2a shows the charge-discharge cycling performance of NVP/C at a C/2 rate in the potential window of 2.5 to 3.8 V (the lower cut off was limited to 2.5 V to compare the results with Yang's work). Our NVP/C showed 1st and 50th discharge capacity values of 98.5 ± 1 mAhg⁻¹ and 85 ± 1 mAhg⁻¹, respectively in the organic electrolyte (error values are calculated based on repeat experiments with separate samples of NVP/C electrode), corresponding to 86.7 %

capacity retention. In contrast, in the organic+IL electrolyte a discharge capacity of 107.0 ± 0.7 mAhg⁻¹ after 50 cycles with capacity retention of 99.7%, and average coulombic efficiency around 99.9 % were obtained. The potential versus specific capacity plots (Figure 3.3c and Figure 3.3d) show that adding ionic liquid reduces the polarization loss, compared to that seen in the organic electrolyte. This is probably because the ionic liquid controls the electrolyte side reactions, and makes a stable passivation layer on the cathode material.

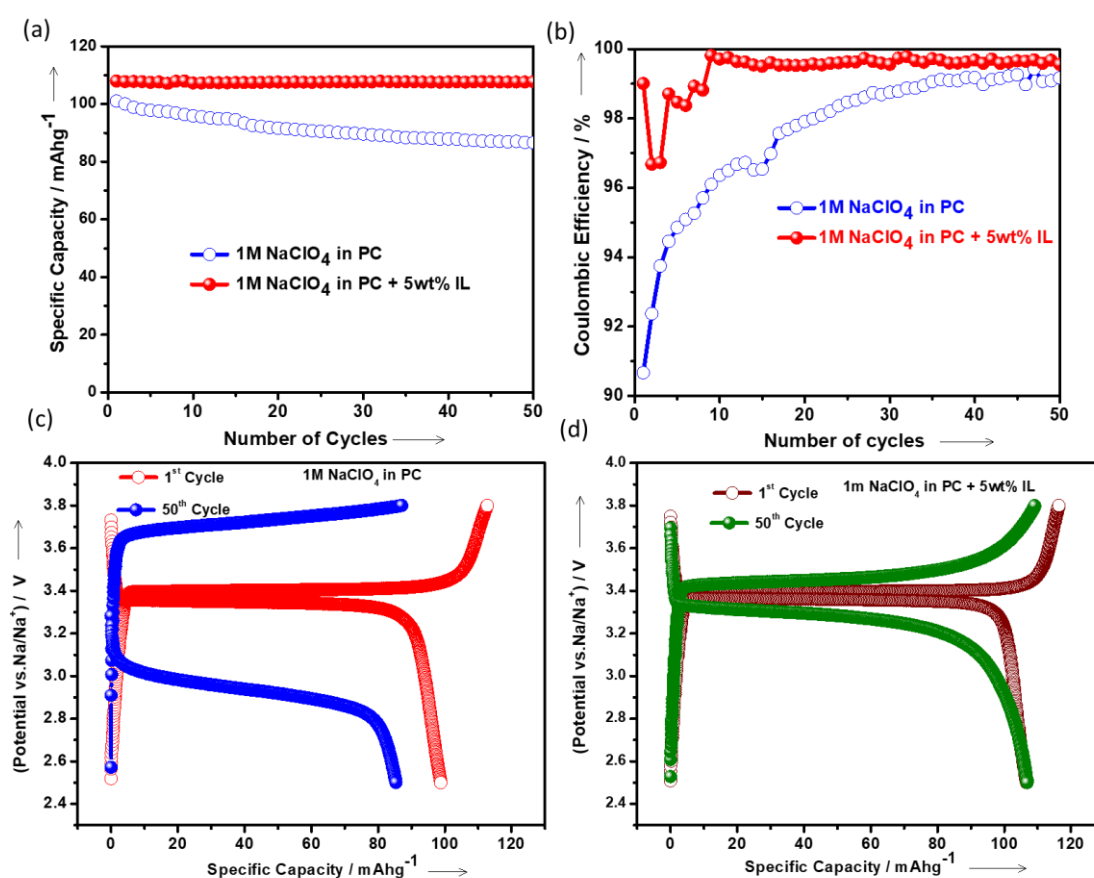


Figure 3. 3:(a) Charge-discharge cycling performance and (b) Coulombic efficiency of NVP/C in organic and organic+IL electrolytes at C/2 rate, with potential ranging from 2.5 to 3.8 V (vs Na/Na⁺), (c) Potential vs. Capacity plot of NVP/C cathodes with organic elect electrolyte, and (d) with organic+IL electrolyte. All cells used sodium metal anodes.

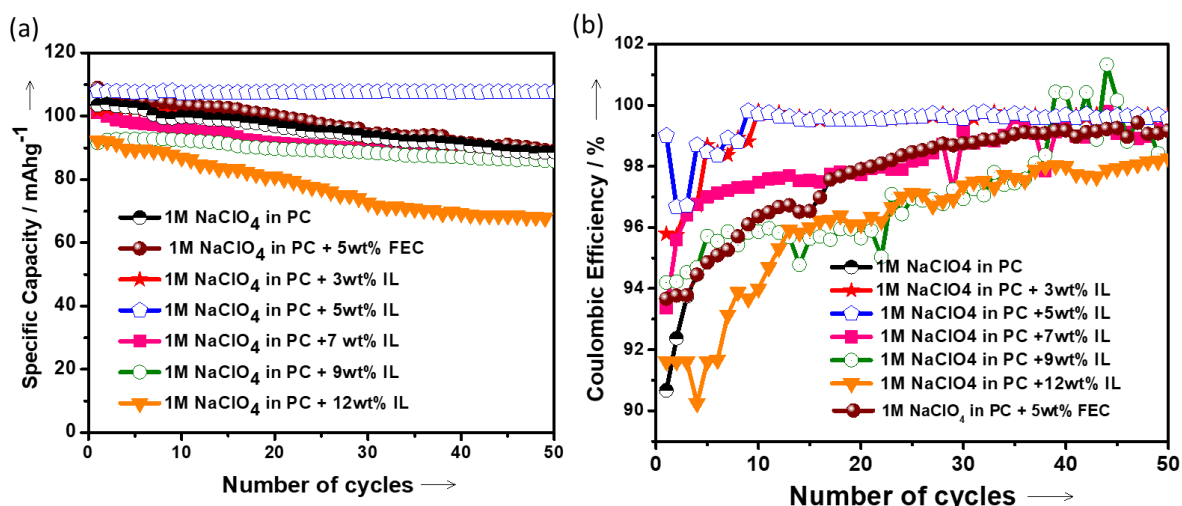


Figure 3. 4: (a) Charge-discharge cycling performance, and (b) Coulombic efficiency of NVP/C in 1M NaClO₄ in PC with FEC and different amounts of [C₃mpyr] [NTf₂] IL added. C/2 rate, with potential ranging from 2.5 to 3.8 V (vs Na/Na⁺).

Additive optimization studies were carried out by varying the [C₃mpyr] [NTf₂] concentration from 3–12 wt% in 1M NaClO₄ in PC electrolyte and evaluating the charge-discharge cycling performance with NVP/C cathode material at a C/2 rate for 50 cycles. Organic and organic+5 wt% FEC electrolytes were also tested for comparison (Figure 3.4). The 50th discharge capacities and coulombic efficiency values obtained for NVP/C material in organic electrolyte with different concentrations of additives are shown in Table 3.1.

Table 3. 1: NVP/C electrochemical performance in 1M NaClO₄ in PC electrolyte with different additives.

Additive	50 th Discharge capacity (mAhg ⁻¹)	Coulombic Efficiency (%)
1M NaClO ₄ in PC + None	90.0±1.1	98.5
1M NaClO ₄ in PC + 5wt% FEC	92.0±0.8	99.3
1M NaClO ₄ in PC+ 3wt% IL	81.0±3.0	99.2
1M NaClO ₄ in PC+5wt% IL	107.0±0.7	99.9
1M NaClO ₄ in PC+7wt% IL	85.0±2.0	98.4
1M NaClO ₄ in PC+9wt% IL	79.0±1.0	96.9
1M NaClO ₄ in PC+12wt% IL	67.0±1.0	96.2

3.5. SEI characterization studies on NVP/C cathode material with organic and organic + IL electrolyte:

To further understand the variation in capacity, at least five cells were cycled for each composition, and the standard deviations for the 5th, 20th and 50th cycles are shown in Figure 3.5. It is observed that 1M NaClO₄ in PC + 5wt% [C₃mpyr] [NTf₂] electrolyte has higher discharge capacity and smaller standard deviation values, compared to those seen for other electrolyte compositions.

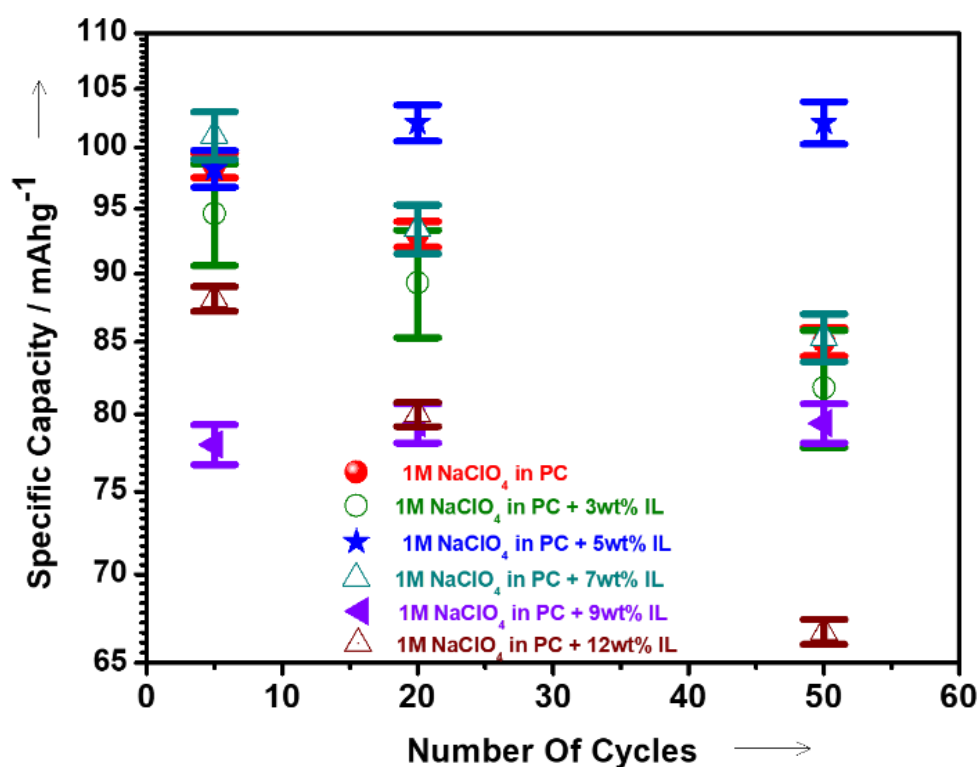


Figure 3. 5: Specific capacity vs. cycle number for 5th, 20th and 50th cycles for different amounts of IL in 1M NaClO₄ in PC electrolyte. SD values are based on measurements of at least five separate cells.

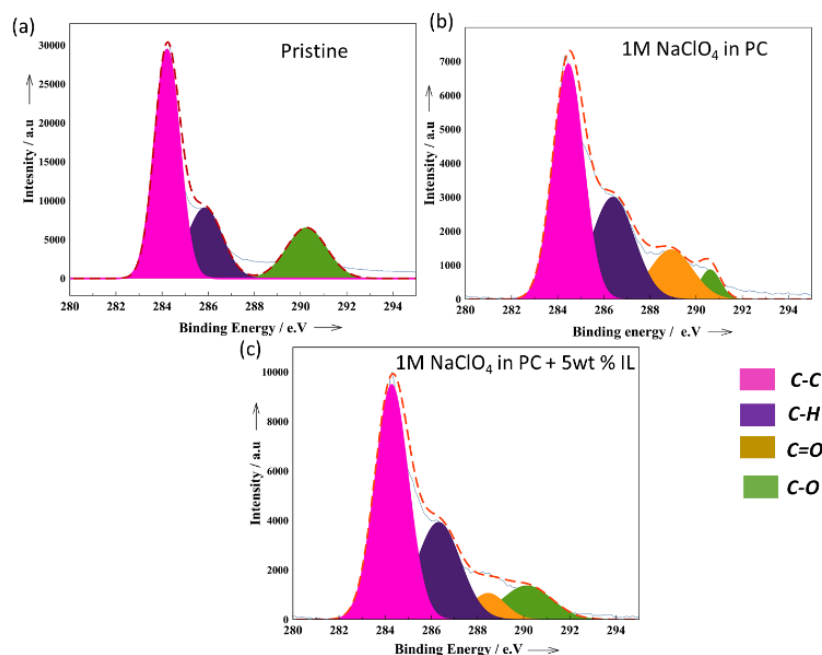


Figure 3. 6: XPS C1s Peaks for NVP/C cathodes. (a) Pristine, and after 50 cycles with (b) Organic, (c) Organic+IL electrolytes

The passive layer formation on the NVP/C electrodes was examined through XPS. In the pristine NVP/C electrode spectrum (Figure 3.6a), peaks at 284.5 eV, 286.7 eV, and 290.8 eV are assigned to C-C(sp²) and C-C(sp³) for the in-situ carbon in NVP/C and the added carbon in the electrode material; C-H and C-F peaks are related to the added PVDF binder. After 50 cycles in either organic or organic+IL electrolyte, another peak occurs at 288.5 eV, which is assigned to C-O species, part of the passivation film on the electrode surface, rather than part of the original, pristine material. The intensity ratio of C-C to C-O peaks is higher for the organic+IL electrolyte than for the organic electrolyte. This is further evidence that the added IL forms a more uniform passivation layer, with less degradation of the electrolyte.

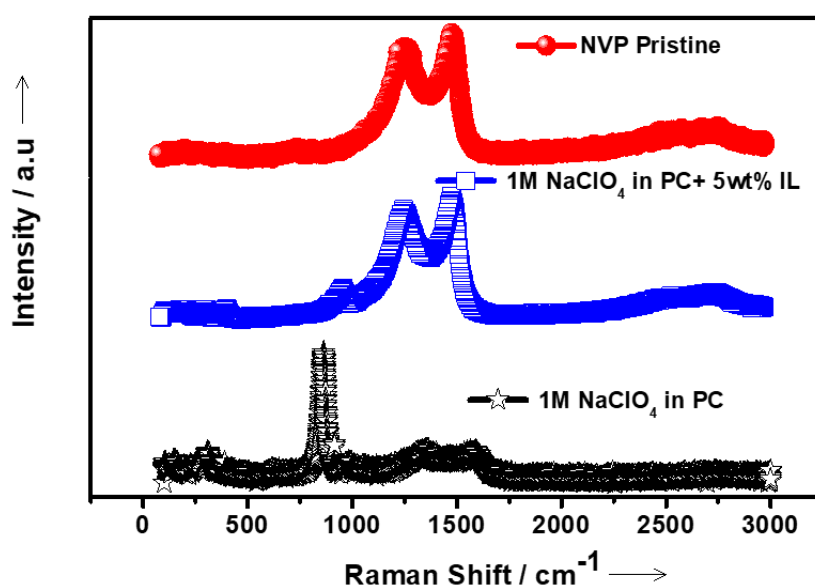


Figure 3. 7: Raman spectra of NVP/C cathode electrode for pristine and after 50 cycles with Organic and ionic liquid added electrolyte

To characterize the nature of SEI layer on the NVP/C cathode material, Raman spectra were collected for fresh NVP/C and for NVP/C after 50 cycles at a rate of C/2 with either organic or organic+IL electrolytes. Significant differences were observed, as shown in Figure 3.7. Raman peaks are assigned to different components in the SEI layers on the surface of the cathode material, as listed in Table 3.2.

Table 3. 2 : Listing of Raman peaks and their assignments for the spectra of the SEI layers on NVP@C electrodes after cycling with organic and ionic liquid added electrolyte.

NVP/C electrode SEI compositions	
Raman Shift (cm ⁻¹)	Assigned to the functional groups
1039	H-F
833	S-F, SO ₂ FSI
563	S-F
447	S-S
332	C-H
231	C-N

The amorphous nature of the carbon in the NVP/C material was confirmed by the I_D/I_G intensity ratios for the fresh and post-cycled NVP/C electrodes; the values were organic electrolyte (1.03), organic+IL electrolyte (0.96) and fresh NVP/C electrode (0.95). Thus, the carbon is more amorphous in the NVP/C cathode material cycled in organic+IL electrolyte.

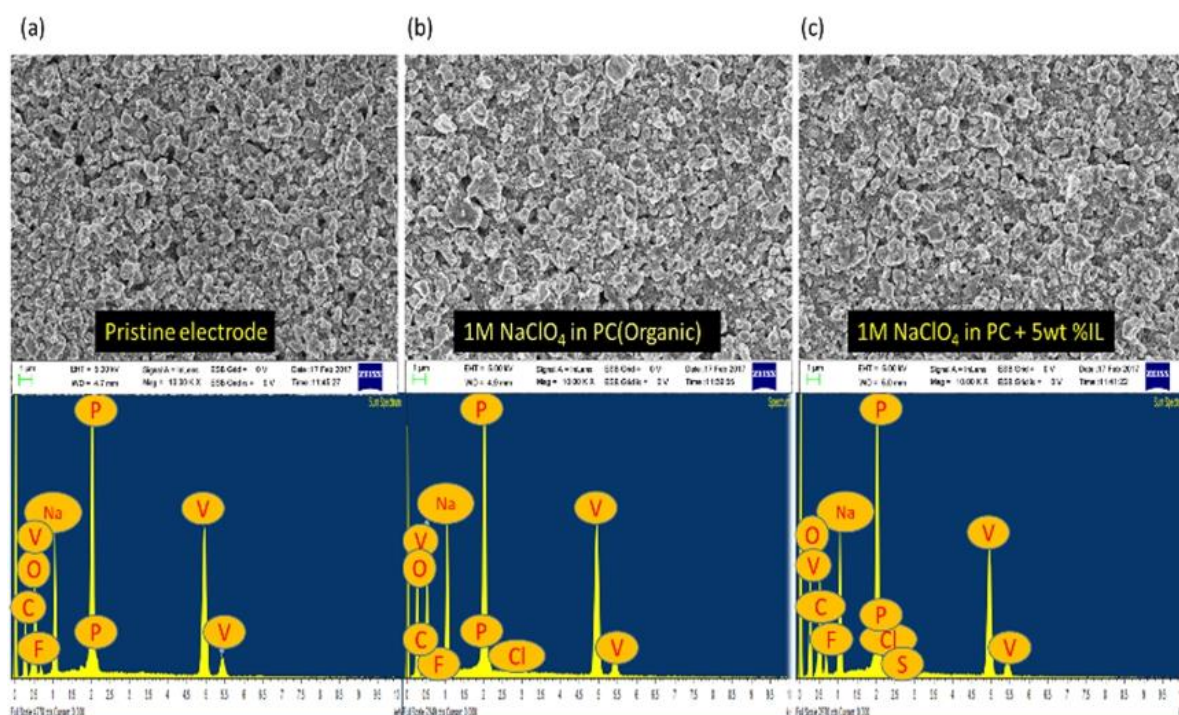


Figure 3. 8:FEG-SEM-EDS images of NVP/C electrodes. (a) pristine, (b) after 50 cycles with organic electrolyte, and (c) after 50 cycles with organic+IL electrolyte

The dispersive energy X-ray (EDX) analysis of the NVP/C electrodes after 50 cycles reveal clear differences (Figure 3.8). Sulfur was found on the surface of the NVP/C electrode cycled with 1M NaClO₄ in PC + 5wt% [C₃mpyr] [NTf₂] electrolyte. This sulfur comes from the IL and may form part of the protective passivation layer on the surface of the electrode.

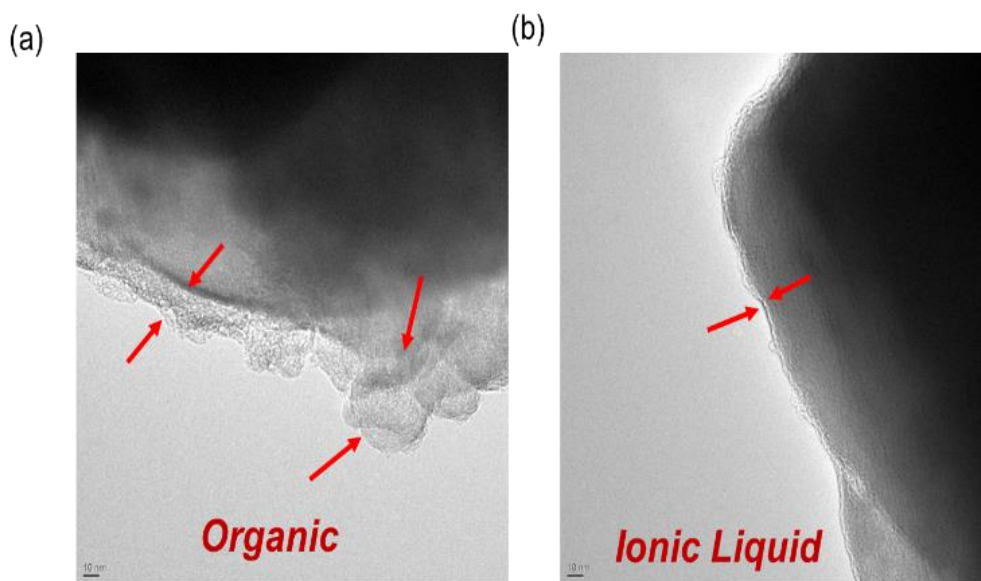


Figure 3. 9: HR-TEM images of NVP/C electrodes after 50 cycles with (a) organic electrolyte (b) organic+IL electrolyte

Figure 3.9 shows the HR-TEM images of NVP/C electrodes cycled with organic and organic+IL electrolytes. With the organic electrolyte, side reactions formed an uneven passivation layer on the surface of the NVP/C material in the sodium battery (Figure 3.9a). In contrast, when NVP/C is cycled in the organic+IL electrolyte, a uniform passivation layer is apparent (Figure 3.9b). This difference in passivation is consistent with the difference in polarization drop with cycling seen in Figures 3.3c and 3.3d. The polarization drop increases, caused by the cathode material deterioration, electrolyte degradation, and unstable surface passivation film formation on electrode materials, can lead to poor cycling performance of batteries.¹⁵³ Here, we observed that the NVP/C cathode cycled in the organic electrolyte showed a high polarization loss and an increased charge transfer resistance. These changes were suppressed by addition of the IL, which appears to lead to a stable passivation layer.

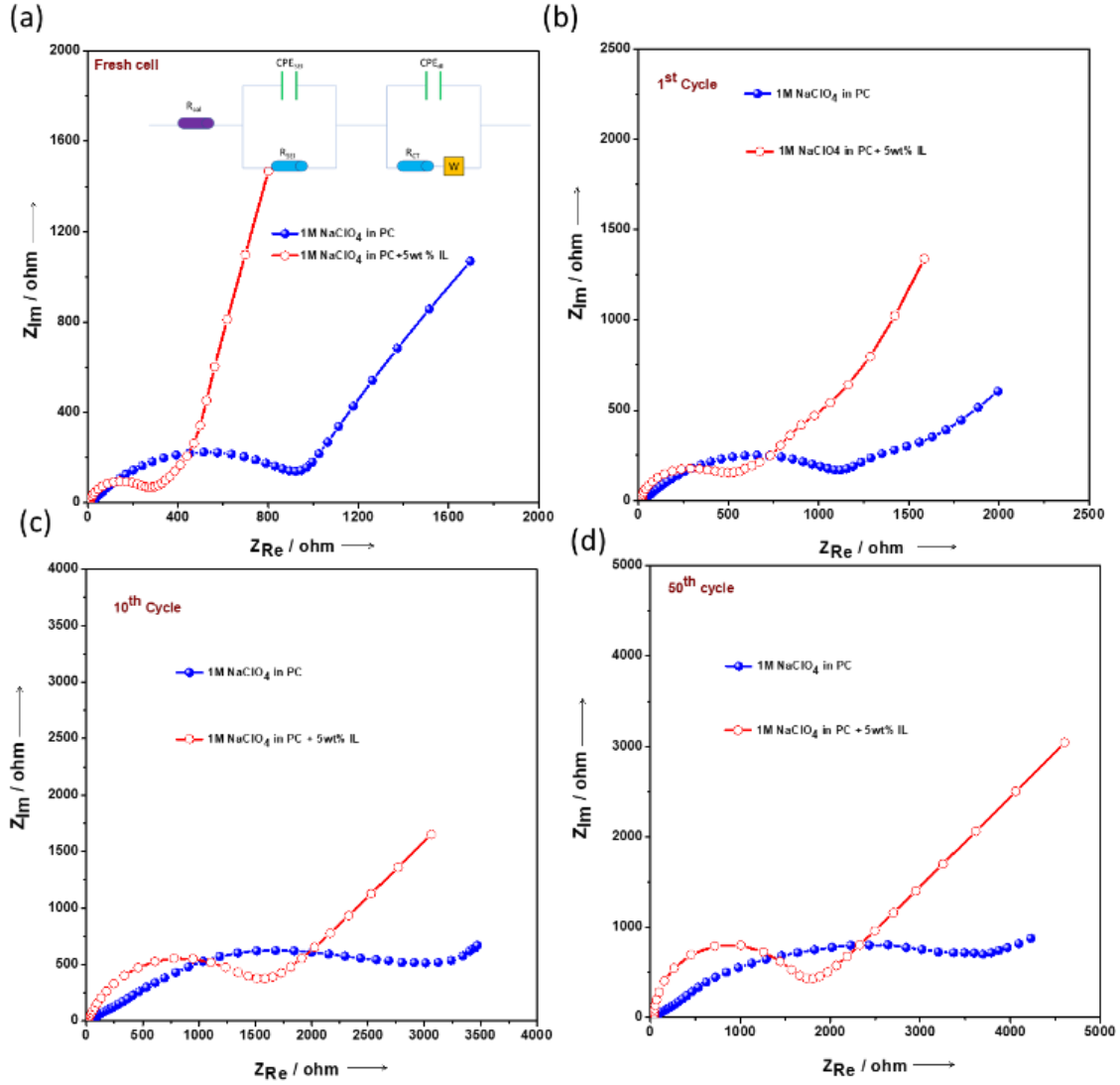


Figure 3. 10: Nyquist plots of NVP/C|Na Cells (a) after aging the cell for one day; then after (b) 1st cycle, (c) 10th cycle, and (d) 50th cycle with organic and organic+IL electrolytes

Electrochemical impedance spectroscopy studies on NVP/C|Na cells with organic and organic+IL electrolytes in the frequency range from 1 MHz to 50 mHz are shown in Figure 3.10. In EIS spectra of batteries, SEI layer resistance, charge-transfer resistance, and Warburg diffusion are usually observed at the high-frequency, mid-frequency and low-frequency regions, respectively.¹⁵⁴ Such spectra are usually fitted to the circuit shown in the inset of Figure 3.10a. Before cycling, the cells were stored for one day to allow spontaneous reactions between the electrodes and electrolytes in the batteries. These spontaneous reactions form passivation layers on the surfaces of the electrodes¹⁵⁵. After storage, the cell with the organic+IL electrolyte had

formed a less resistive passivation layer, as indicated in Figure 3.10a. After the first cycle, the EIS spectra of the two cells showed significantly different low-frequency regions (Figure 3.10b), corresponding to differences in diffusion of ions into and out of the electrodes. The cell containing the organic electrolyte showed greater irreversible loss after the first charge-discharge cycle with NVP/C cathode material (Figure 3.3). This loss is caused by sodium accumulation on the diffusion layer; this sodium cannot reach the active materials because of the more resistive surface film (Figure 3.10a). In contrast, the organic+IL electrolyte controlled the irreversible loss of sodium on the diffusion layer on the cathode material in the sodium battery (Figure 3.10b). After subsequent cycles, these resistance values are increased for both electrolytes, but the organic+IL electrolyte shows less resistive layers on the electrodes, and superior cycling performance compared to that of the organic electrolyte (Figures 3.10c and 3.10d). Therefore, the addition of 5wt% IL to the conventional organic electrolyte enhanced the NVP/C cycling performance for sodium metal battery.

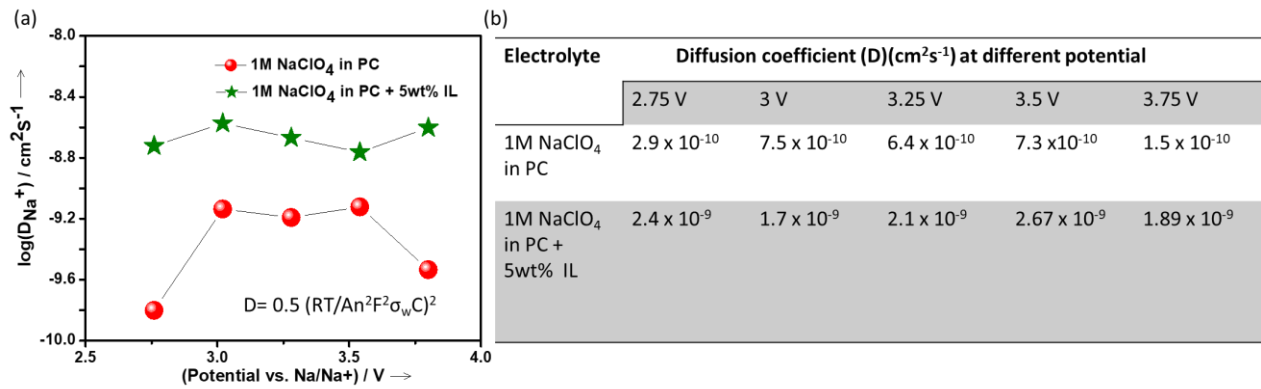


Figure 3. 11: Diffusion coefficient (as evaluated from Warburg impedance) for NVP/C material at different potentials during first discharging cycle in inorganic and organic +IL electrolytes.

EIS is another way to examine the electrode surface diffusion kinetics at different potentials in batteries. The Warburg parameter, σ_w , can be used to calculate the diffusion coefficient of the NVP cathode material using the equation in the inset of Figure 3.11. These results confirmed that adding IL to the electrolyte leads to a less resistive passivation layer on the surface of the electrode, thus improving the NVP/C material diffusion coefficient compared to that seen with

the conventional organic electrolyte.

3.6 Summary:

NVP/C composite material was demonstrated as a cathode material for sodium-ion batteries using [C₃mpyr] [NTf₂] IL as an electrolyte additive. The optimum content of 5 wt% IL showed far more stable cycling performance with NVP/C composite compared to that seen when NVP/C composite was cycled in the base organic electrolyte. The electrolytes with added IL controlled the side reactions on the surface of the electrode, and improved the Na⁺ ionic mobility within the passivation layer, which further enhanced the charge-discharge cycling performance. A sodium-ion battery using the composite cathode and the IL-containing electrolyte exhibited high discharge capacity of 107.0±0.7 mAhg⁻¹, with capacity retention around 99.7%, and an average coulombic efficiency around 99.4%, which was significantly better than the performance found with an IL-free electrolyte (1M NaClO₄ in PC). The HR-TEM images show passivation layers on the surface of NVP/C electrodes for organic and IL-containing electrolytes. EDX found Sulphur in the surface film of the electrode cycled with IL-containing electrolyte, and this surface film was more stable than that produced on the NVP/C electrode in the base organic electrolyte

Chapter 4

Stability-enhancing ionic liquid based hybrid electrolyte for NVP@C cathode based sodium-ion batteries

4.1 Introduction:

In batteries, electrolyte selection is also critical — electrolytes must have high ionic conductivity, a wide electrochemical stability and high thermal stability. Commercial lithium-ion battery electrolytes comprise of a lithium salt dissolved in organic solvents. These display excellent ionic conductivity, but are volatile, toxic and flammable.¹⁵⁶⁻¹⁵⁹ Ionic liquid (IL) based electrolytes have been proposed to enhance battery safety, and have been extensively studied for lithium-ion batteries over the past few years.⁶⁶⁻⁷⁰ This work suggests that ILs may also be suitable electrolytes for sodium-ion batteries.⁷¹⁻⁷⁶ In particular, pyrrolidinium-based ILs display a large electrochemical window and good cycling stability with sodium.^{72, 73, 75} For example, 1-methyl 1-propyl pyrrolidinium bis(fluorosulfonyl)imide (C₃mpyrFSI) has been used as an electrolyte with hard carbon and NaCrO₂ electrode systems, and was cycled more than 500 times in a sodium-ion battery.⁷⁴ Imidazolium based ILs have also been used as electrolytes for different sodium-ion battery systems, but the acidic proton on the imidazolium ring causes decomposition of the electrolyte at relatively modest voltages.⁷⁷⁻⁸¹

ILs generally display higher viscosity and lower ionic conductivity than those of conventional organic electrolytes at room temperature. Therefore in order to reduce their viscosity, “hybrid electrolytes” — mixtures of IL and organic electrolyte — were developed, and provided improved electrochemical performance and safety in lithium-ion batteries.⁸²⁻⁸⁶ Palacin et al. reported hybrid electrolyte formulations and studied their physical properties, electrolyte thermal stability, solvation ability and electrochemical performance with hard carbon as a sodium-ion battery anode.¹⁶⁰ However, the electrochemical stability of this hybrid electrolyte was found to be only 3V versus sodium, which is too low for most sodium cathode materials.

Here we seek improved sodium batteries that can operate at room temperature. We have developed a simple synthesis of a composite cathode of carbon and $\text{Na}_3\text{V}_2(\text{PO}_4)_3$, NVP@C and characterized its performance in detail with hybrid electrolytes comprising 1M NaFSI in a mixture of ethylene carbonate (EC)/propylene carbonate (PC) organic electrolyte and an ionic liquid, ($\text{C}_3\text{mpyrTFSI}$) (The choice of ionic liquid here will be further explored and discussed in Chapter 5). The surface layers formed on the cathode are examined by XPS, TEM and SEM.

4.2 Synthesis and Characterization of NVP@C electrodes:

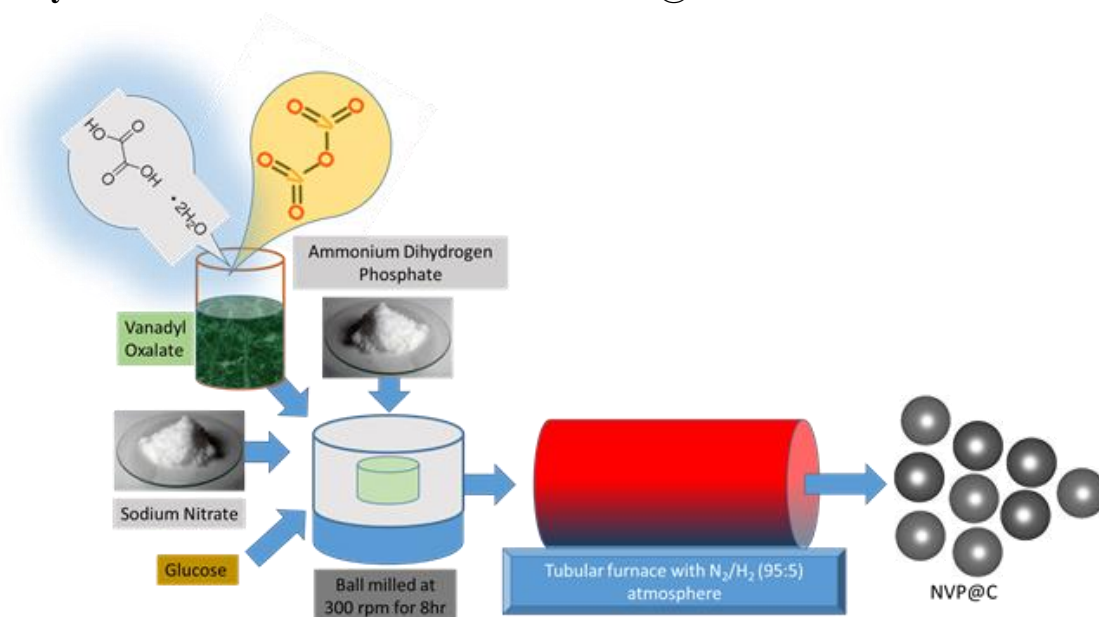


Figure 4. 1: Schematic representation of NVP@C synthesis

Our approach to the synthesis of NVP – carbon composites is described in detail in the experimental section and summarized in Figure 4.1. This process is facile and could be readily scaled up. The XRD pattern of as-prepared NVP@C is displayed in Figure 4.2a. The NVP@C diffraction patterns match with ICSDS data (card no-248410) and show the formation of a crystalline NASICON-type framework with an $\text{R}\overline{3}\text{C}$ space group.¹⁶¹

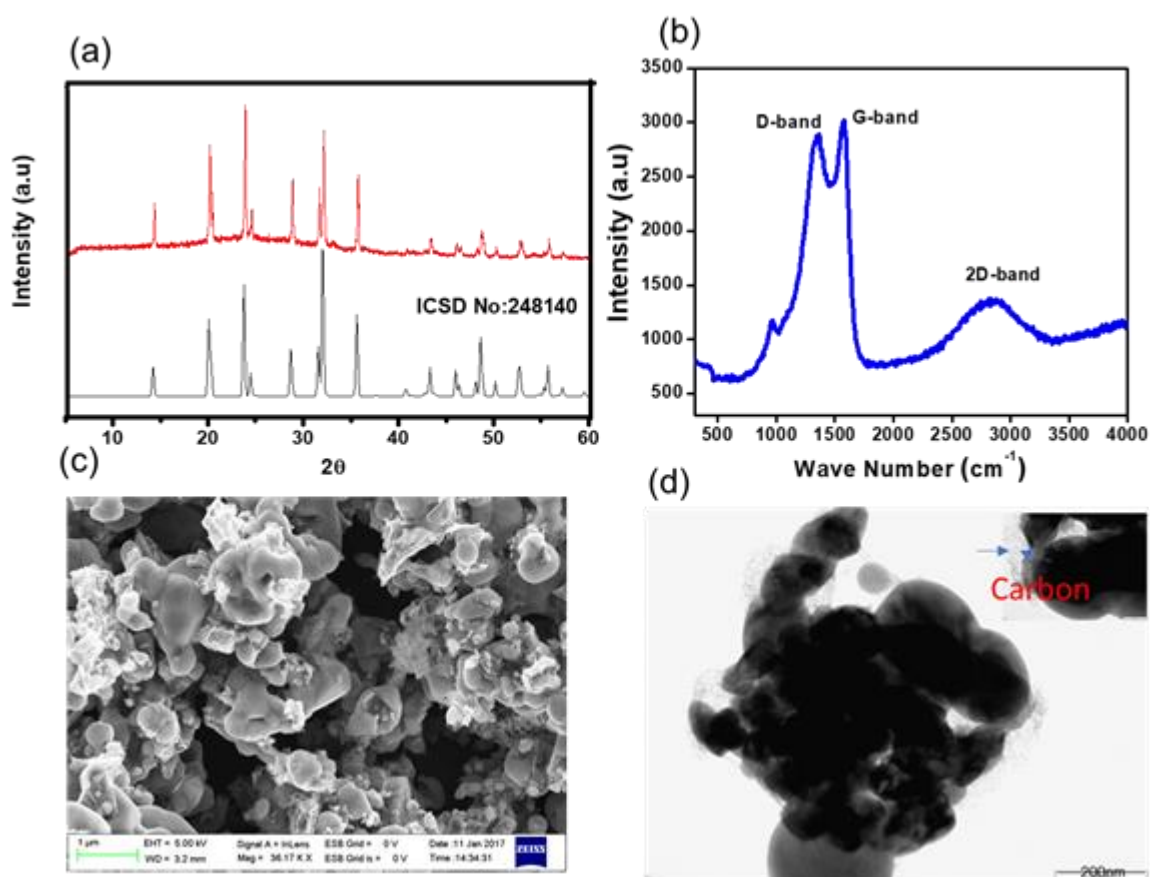


Figure 4. 2: Characterization of NVP@C: (a) Powder XRD pattern (red is experimental, black is literature); (b) Raman spectrum; (c) FE-SEM image; and (d) HR-TEM images

The surface of NVP@C was investigated with Raman spectroscopy (Figure 4.2b). NVP@C displayed a vibration band around 1000 cm⁻¹, which corresponds to weak stretching vibrations of PO₄³⁻. The stronger peaks at 1316 cm⁻¹ and 1605 cm⁻¹ are related to the D and G bands intrinsic to residual carbon, confirming the presence of amorphous carbon in NVP@C. This is consistent with the elemental analysis, which found that NVP@C contains 4.2 wt% carbon.

Figure 4.2c is an SEM image of as-prepared NVP@C powder, showing micron-sized particles.

The TEM image in Figure 4.2d shows agglomerates of NVP@C particles partly coated with amorphous carbon.

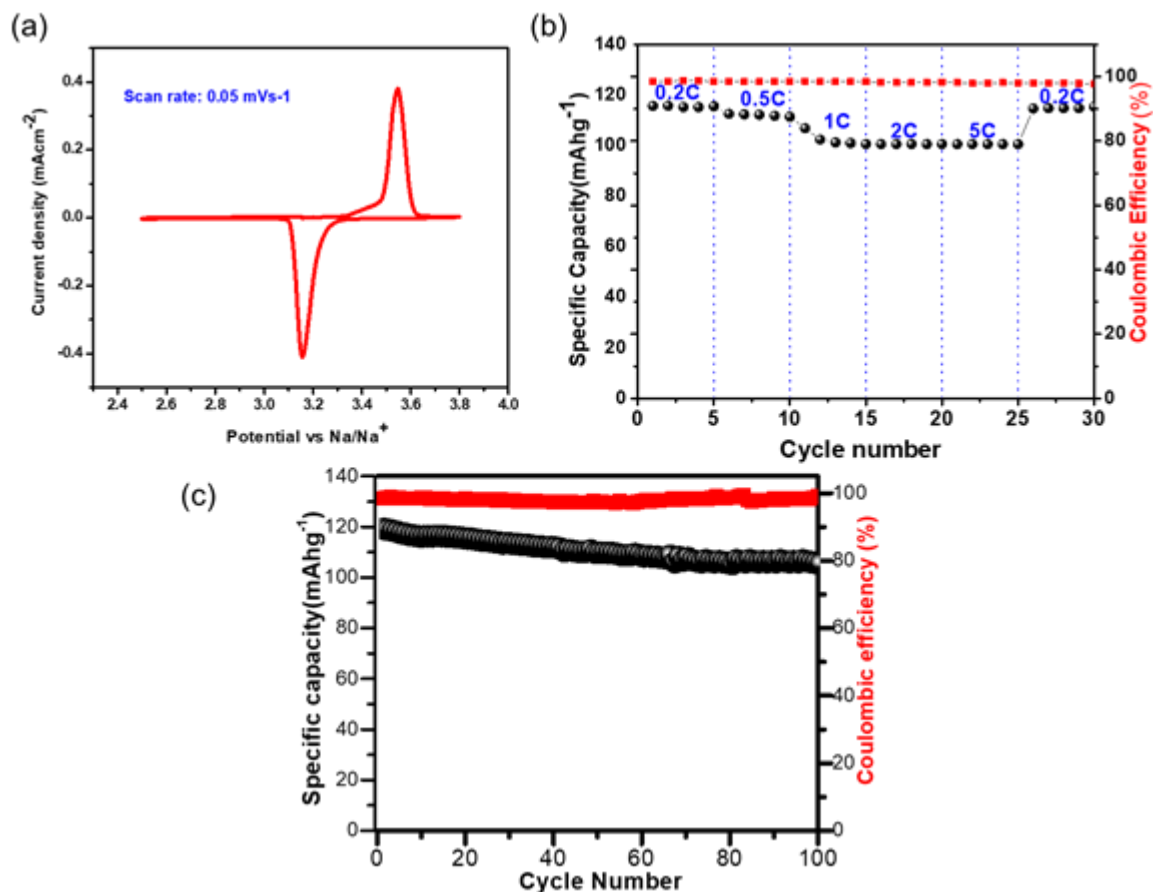


Figure 4. 3: Electrochemical performance of NVP@C: (a) CV curve measured from 2.5 to 3.8 V vs. Na/Na⁺, scan rate 0.05 mVs⁻¹ in organic electrolyte (b) Cycling performance at various C-rates (c) Cycling performance at 0.5C rate; potential range from 2.5 to 3.8 V vs. Na/Na⁺ with 1M NaClO₄ in a EC: PC electrolyte at 20⁰C.

The CV for NVP@C, measured with conventional electrolyte (1M NaClO₄ in EC: PC (1:1) v/v) at scan rate 0.05mVs⁻¹, showed two redox peaks at 3.41 and 3.35 V vs. Na⁺/Na, which correspond to the oxidation/reduction of V⁴⁺/ V³⁺ (Figure 4.3a). The charge-discharge cycling performance of NVP@C at different current densities is presented in Figure 4.3b; NVP@C showed initial discharge capacity values of 114, 112, 104, 102 and 100 mAhg⁻¹ at discharge rates of 0.2, 0.5, 1, 2 and 5C, respectively. This result indicates lower polarization loss and high reversible capacity of our NVP@C composite material as compared to previously-reported versions of similar materials.¹⁶¹⁻¹⁶⁷ As shown in Figure 3.3c, NVP@C retains 89% of its capacity when charged and discharged at 0.5C for 100 cycles. This material was further investigated with the hybrid electrolytes as discussed below.

4.3 Characterization of hybrid electrolytes:

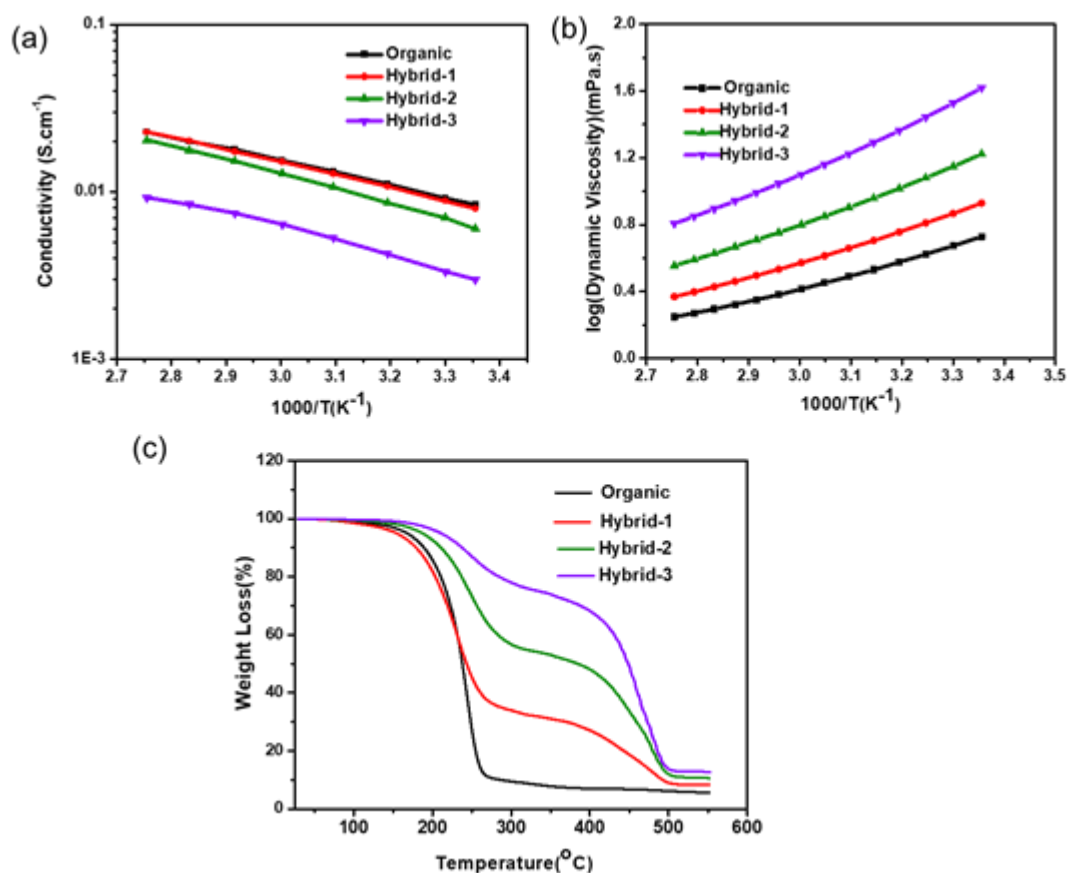


Figure 4. 4:(a) Ionic conductivity (b) viscosity and (c) TGA measurements for organic and hybrid electrolytes.

Ionic conductivity of the organic and hybrid electrolytes as a function of C₃mpyrTFSI concentration at various temperatures is shown in Figure 4.4a. At 25 °C, the conductivity value of the organic electrolyte was 5.5 mScm⁻¹, which is consistent with a previously reported value.¹⁶⁸ The conductivities of the hybrid electrolytes decreased with increasing IL concentration (4.2, 3.2, 2.9 mScm⁻¹ for hybrid-1, hybrid-2 and hybrid-3, respectively); this is expected because of the increased viscosity and enhanced ion-ion interactions at higher IL concentrations.^{169, 170} Viscosities of organic and hybrid electrolytes are shown in Figure 4.4b; the hybrid electrolyte viscosities increase at higher IL concentrations.

The thermogravimetric analysis (TGA) data for the organic and hybrid electrolytes are shown in Figure 4.4c. The organic electrolyte showed a significant mass loss of >75% when the temperature reached 250°C, corresponding to the evaporation of organic solvents (EC and PC). In contrast, the hybrid electrolytes showed lower mass losses: 55%, 27% and 12% for hybrid-1, hybrid-2 and hybrid-3, respectively at 250 °C, indicating their increased thermal stability. Furthermore, the addition of C₃mpyrTFSI to the electrolytes shifted the EC/PC evaporation temperature to higher values (300°C).

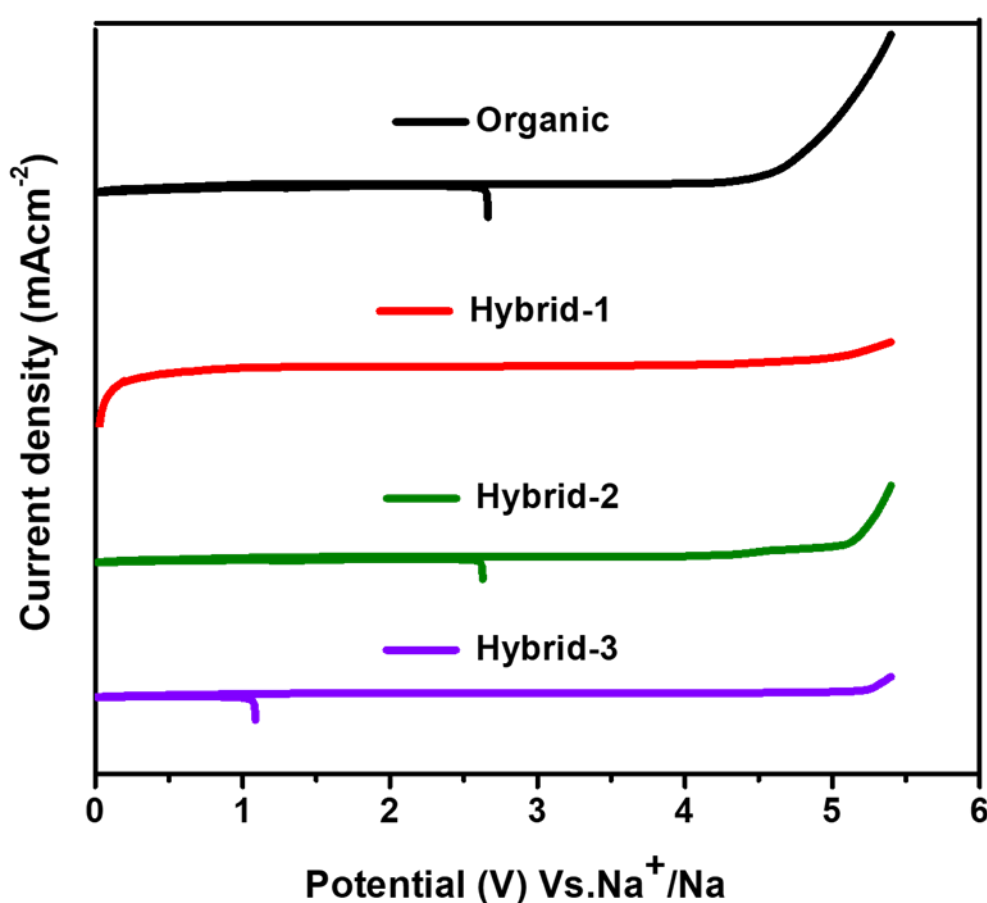


Figure 4. 5: Electrochemical oxidative stability tests (by cyclic voltammetry) in three electrode Swagelok cells at 10mVs⁻¹ scan rate.

CV was used to evaluate the electrochemical oxidative stability for the electrolytes in contact with sodium metal (Figure 4.5). Hybrid electrolytes showed higher oxidative stability than the organic electrolyte; the oxidative stability trend followed the IL concentration with hybrid-3

(5.1 V vs. Na^+/Na) > hybrid-2 (5 V vs. Na^+/Na) > hybrid-1 (4.2 V vs. Na^+/Na) > organic electrolyte (4 V vs. Na^+/Na).

4.4 NVP@C combined with hybrid electrolytes:

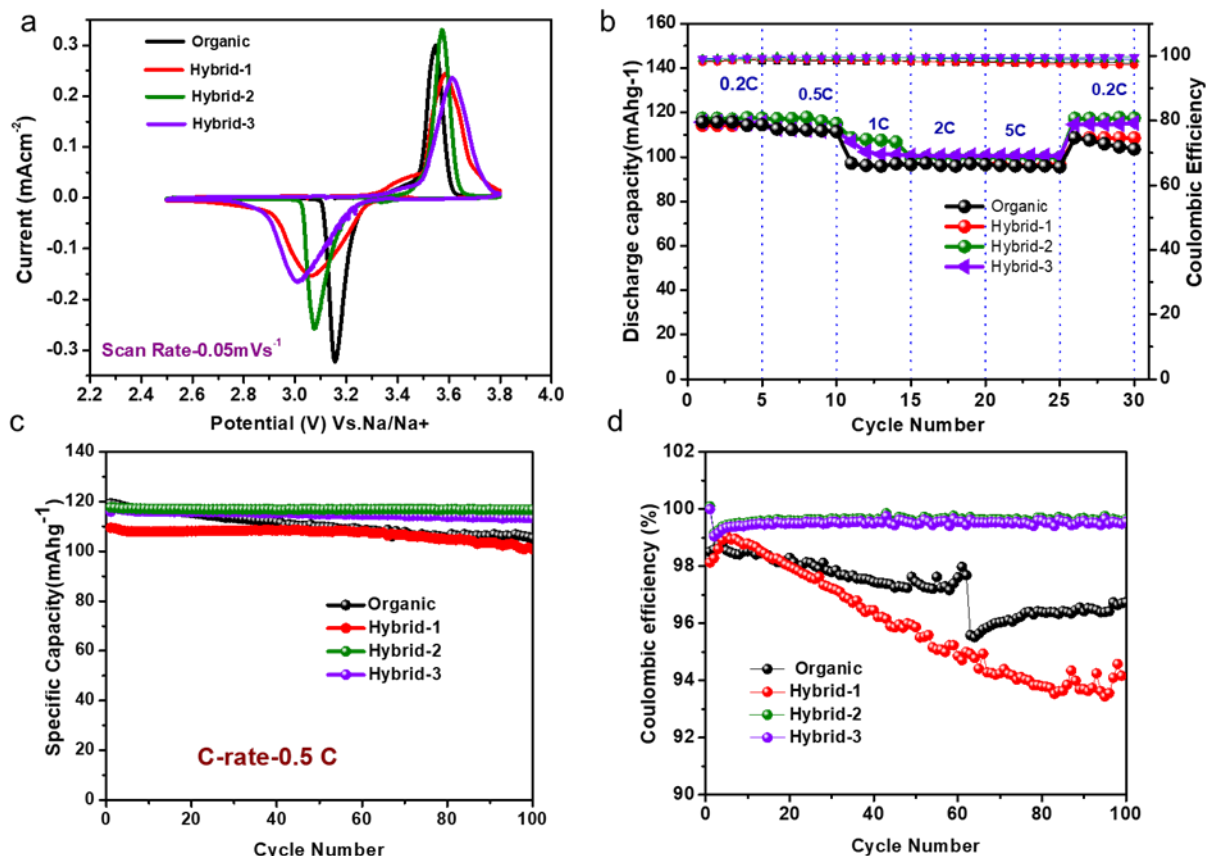


Figure 4. 6:(a) CVs for NVP@C, at a scan rate of 0.05 mVs⁻¹, (b) Cycling performance of NVP@C at various C-rates (c) Cycling performance of NVP@C with organic electrolyte and hybrid electrolytes at 0.5C; (d) Coulombic efficiency of NVP@C with organic and hybrid electrolytes at 0.5C; potential range from 2.5 to 3.8 V vs Na/Na⁺.

CVs of NVP@C with organic (1M NaFSI in EC: PC(1:1)(v/v)) and our new hybrid electrolytes are shown in Figure 4.6a. NVP@C clearly shows the oxidation/reduction reaction, $\text{Na}_3\text{V}_2(\text{PO}_4)_3 \leftrightarrow \text{NaV}_2(\text{PO}_4)_3$, in both organic (at 3.44 ± 0.02 V vs. Na/Na^+) and hybrid (at 3.22 ± 0.02 V vs. Na/Na^+) electrolytes. Figure 4.6b shows the charge-discharge cycling performance of NVP@C with organic, hybrid-1, hybrid-2 and hybrid-3 electrolytes at various current rates from 0.2 to 5C for 5 cycles. NVP@C with hybrid-2 electrolyte delivered discharge capacities of 115, 112, 108, 104 and 100 mAhg⁻¹ at 0.2, 0.5, 1, 2 and 5C, respectively. After this cycling,

the discharge capacity of the same NVP@C material was measured again at 0.2C, and yielded the original value of 115 mAhg⁻¹. This shows the stable cycling performance of this combination of hybrid electrolyte and NVP@C. The behaviour of NVP@C with organic electrolyte was similar to that with hybrid electrolyte at lower discharge rates (115 and 112 mAhg⁻¹ at 0.2 and 0.5C, respectively). However, at higher discharge rates (1, 2 and 5C) in the organic electrolyte, the capacity decreased to 95 mAhg⁻¹. There was no decrease in capacity in the hybrid electrolytes even at the 5C rate.

The charge-discharge cycling performance of NVP@C was examined at 0.5C rate with both organic and hybrid electrolytes for 100 cycles (Figure 4.6c). NVP@C retained its discharge capacity of 112 ± 3 mAhg⁻¹ at 0.5 C rate for 100 cycles with hybrid-2 and hybrid-3 electrolytes. NVP@C with the organic electrolyte gave 1st and 100th discharge capacities of 112±3 mAhg⁻¹ and 105±2 mAhg⁻¹, respectively, at 0.5C rate – a capacity retention of 87% over 100 cycles. NVP@C in the hybrid electrolytes with higher concentrations of IL delivered both slightly higher discharge capacities and stable cycling performance compared to that obtained in the organic and hybrid-1 electrolytes.

The coulombic efficiency data for 100 cycles are shown in Figure 4.6d. NVP@C in hybrid-2 and hybrid-3 electrolytes displayed coulombic efficiencies of approximately 99%, respectively, over 100 cycles while NVP@C with organic and hybrid-1 electrolytes gave coulombic efficiencies of 98% and 96%, respectively. In summary, the hybrid electrolytes offer more stable cycling than organic electrolytes.

4.4.1 Characterization of Na metal and NVP@C SEI layers:

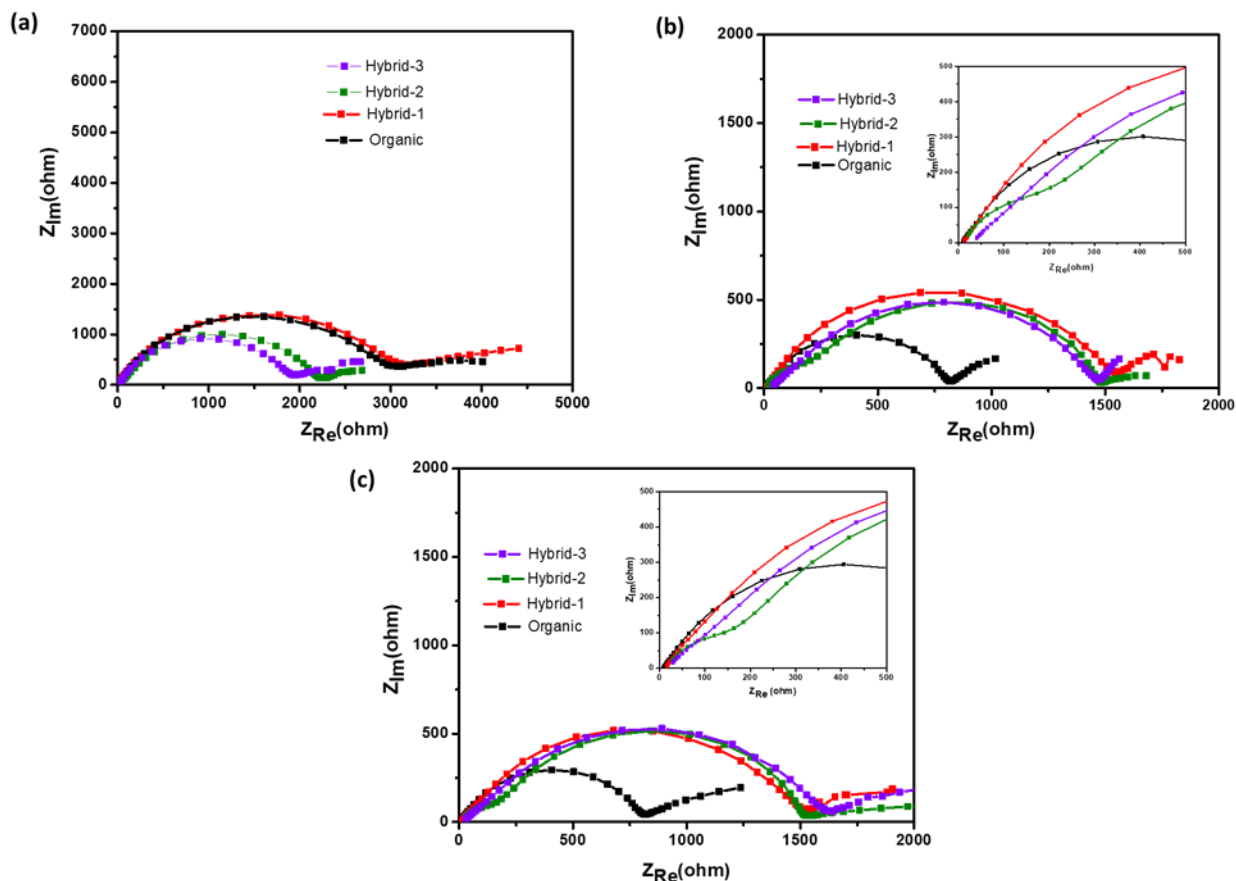


Figure 4. 7: Electrochemical impedance measurements for Na//Na symmetrical cells at (a) OCV, (b) after 50 cycles, and (c) after 100 cycles with organic and hybrid electrolytes.

Figure 4.7 shows the Nyquist impedance plots for sodium symmetrical cells after the charge-discharge cycling with organic and hybrid electrolytes at 0.1 mA/cm^2 . At OCV, the organic and hybrid-1 electrolytes displayed high charge transfer resistances, as compared to those found with hybrid-2 and hybrid-3 electrolytes (Figure 4.7a); this is related to sodium diffusion kinetics at the electrode/electrolyte interface. After the 50th and 100th cycles, hybrid-2 and hybrid-3 electrolytes showed an additional feature (see inset) at high frequency in the Nyquist plots; this is related to the resistance of the SEI layers formed on the surface of the Na metal.¹¹⁷ (Figure 4.7b and 4.7c). In contrast, Nyquist plots of cells containing organic and hybrid-1 electrolytes do not exhibit depressed semicircles at high-frequency, and this behavior is known to be associated with capacity fade behavior in some of other systems with organic electrolytes.^{168, 171, 172} It appears that hybrid-2 and hybrid-3 electrolytes form stable SEI layers

on the surface of Na metal, thus controlling the electrolyte decomposition reaction, and enhancing the electrolyte stability while avoiding dendrite formation in sodium cells. There were no changes of SEI layer resistance observed for hybrid-2 and hybrid-3 electrolytes at 50th and 100th cycles – implying that the SEI layer is stable.

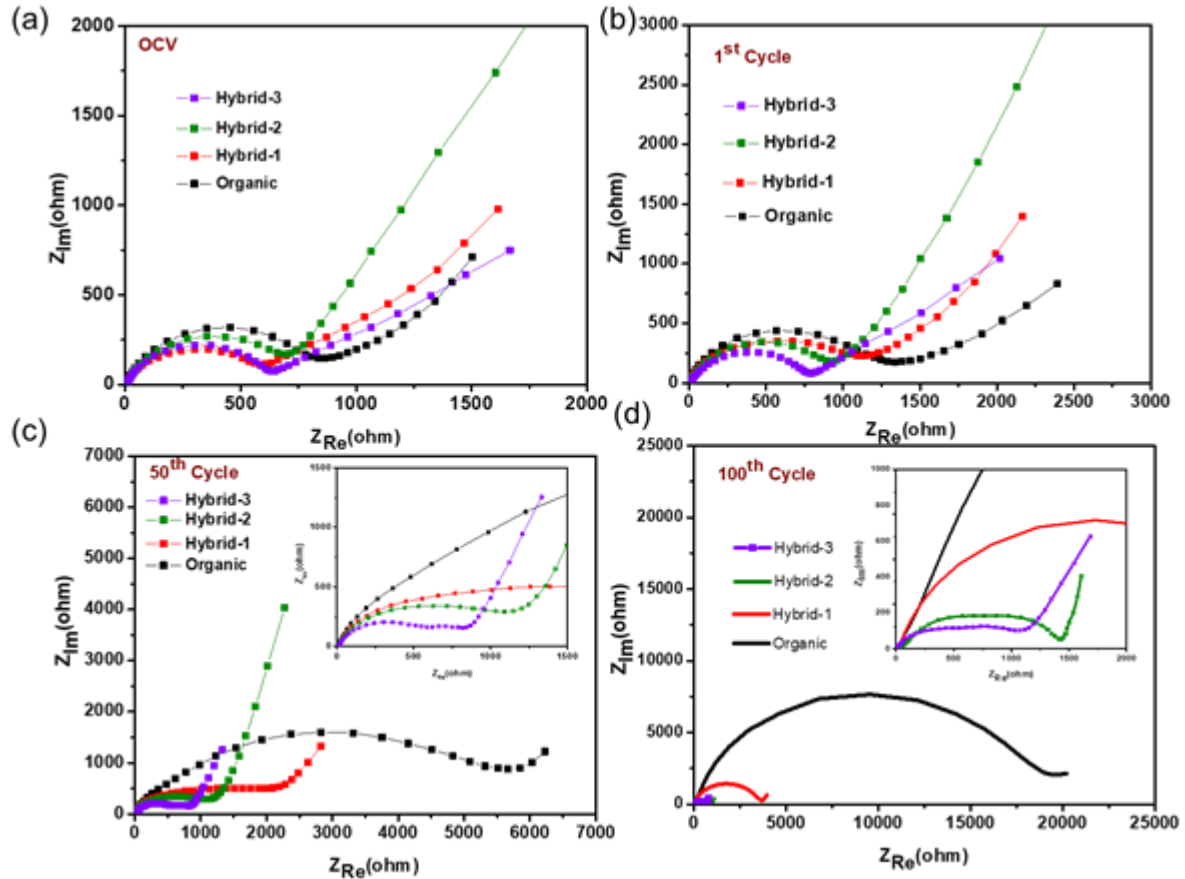
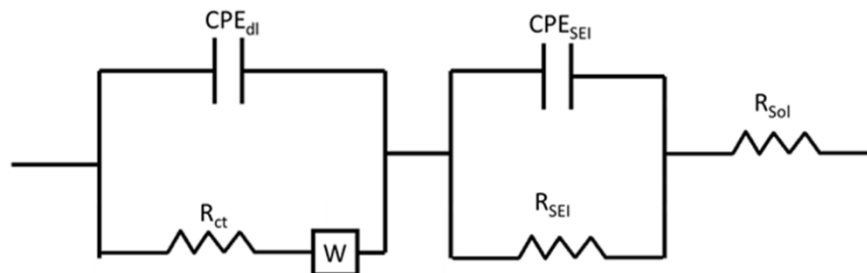


Figure 4. 8: Electrochemical impedance measurements for NVP@C at (a) OCV, (b) after 1 cycles, (c) after 50 cycles, (d) after 100 cycles with organic and hybrid electrolytes.

Electrochemical impedance spectroscopy (EIS) studies were also performed for organic and hybrid electrolytes with sodium foil as an anode material and NVP@C electrode as cathode material in 2032-coin cells. The EIS spectra are shown in Figure 4.8. These experiments were performed at OCV, 1st cycle, 50th cycle and 100th cycle, while cycling at 0.5C rate. The differences observed here are more dramatic than those observed for the Na/Na symmetric cells and suggest that the different electrolytes have a much larger impact on the cathode performance. At OCV and 1st cycle, hybrid electrolytes showed lower charge transfer

resistances in the EIS, as compared to that obtained with the organic electrolyte (Figure 4.8a and Figure 4.8b). After the 50th cycle, we can see a depressed semicircle at high frequency. The magnitude of the depressed semicircle is too large to be the sodium anode SEI layer and therefore we hypothesise that this is related to the SEI layer resistance on NVP@C electrode material (Table 4.1). A second depressed semicircle occurs in the low frequency region, which is related to charge transfer resistance, for hybrid-2 and hybrid-3 electrolytes. The values of charge-transfer resistance and SEI layer resistance obtained with the hybrid electrolytes are lower than those obtained with the organic electrolyte. After the 100th cycle, the EIS spectra of the hybrid electrolytes still displayed lower SEI layer resistances at high frequency and smaller charge transference resistances (Figure 4.8c and 4.8d) than the organic electrolyte.

Table 4. 1: RC Circuit and resistance values for hybrid electrolytes in sodium ion battery.



System	R_{SEI} (ohm)	R_{ct} (ohm)	R_{sol} (ohm)
Na HE-2 Na	144.9	823.4	14.4
Na HE-3 Na	129.3	689.7	14.8
NVP@C HE-2 Na	731.2	782.8	16.2
NVP@C HE-3 Na	607.6	731	16.7

- R_{SEI} -SEI resistance

- R_{ct} - Charge transfer resistance

- R_{sol} - Solution resistance

-HE- Hybrid electrolyte

Thus, EIS data demonstrate that hybrid-2 and hybrid-3 electrolytes provide significantly more stable and low resistance SEI layers on the working surface of the NVP@C electrode materials.

This is consistent with the improved cell cycling behaviour demonstrated in Figure 4.6. In the case of the organic electrolyte, a depressed semicircle at high frequency region and Warburg diffusion impedance in the low frequency region were not observed. This EIS spectrum indicates that organic electrolyte generates an unstable passivation layer and poor Na^+ ion diffusion between electrode and electrolyte interface while cycling with the NVP@C electrode. This unstable passivation layer formation has been observed in other studies on cycling with organic electrolytes in sodium ion batteries. The hybrid-1 electrolyte showed SEI resistance and charge transfer resistance values in between those obtained with the organic electrolyte and those obtained with hybrids 2 or 3.

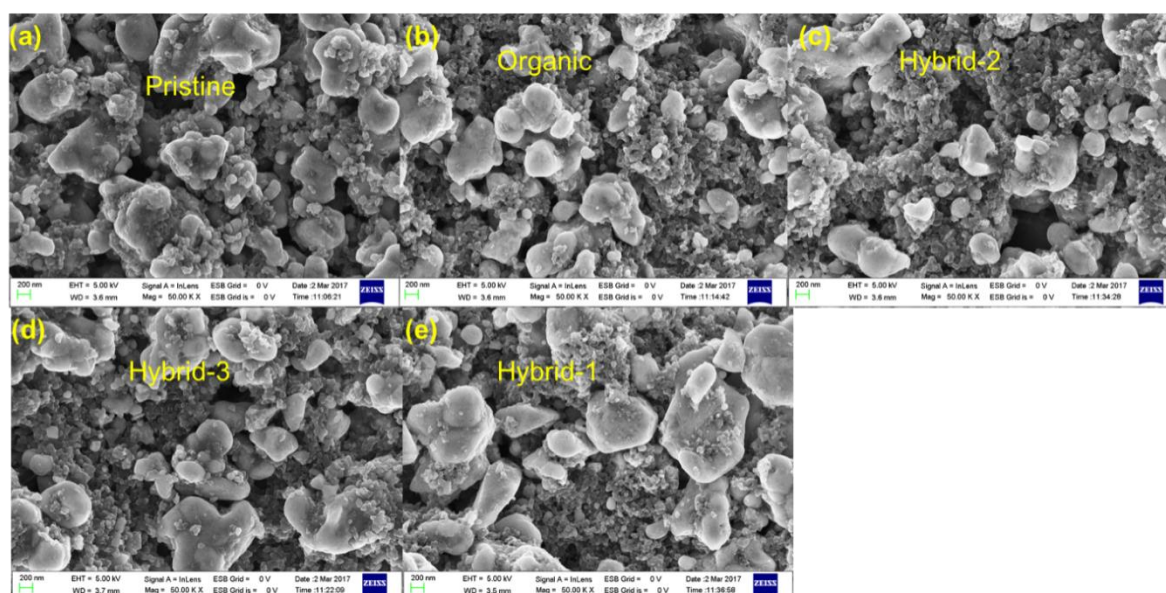


Figure 4. 9:FEG-SEM images of NVP@C electrodes: pristine and after 100 cycles with organic and hybrid electrolytes.

The FEG-SEM images (Figure 4.9) of the NVP@C electrode before and after 100th cycles show that the pristine electrode has a rough surface with many pores; after 100 cycles, the electrodes have become rather smooth, because of the formation of an SEI layer on the surface during cycling. In both cases, no structural damage is seen on the NVP@C electrode. The data suggests that increasing the IL concentration in the hybrid electrolytes prevents the decomposition of organic solvents (EC and PC) that has been observed in other systems.^{83, 173,}

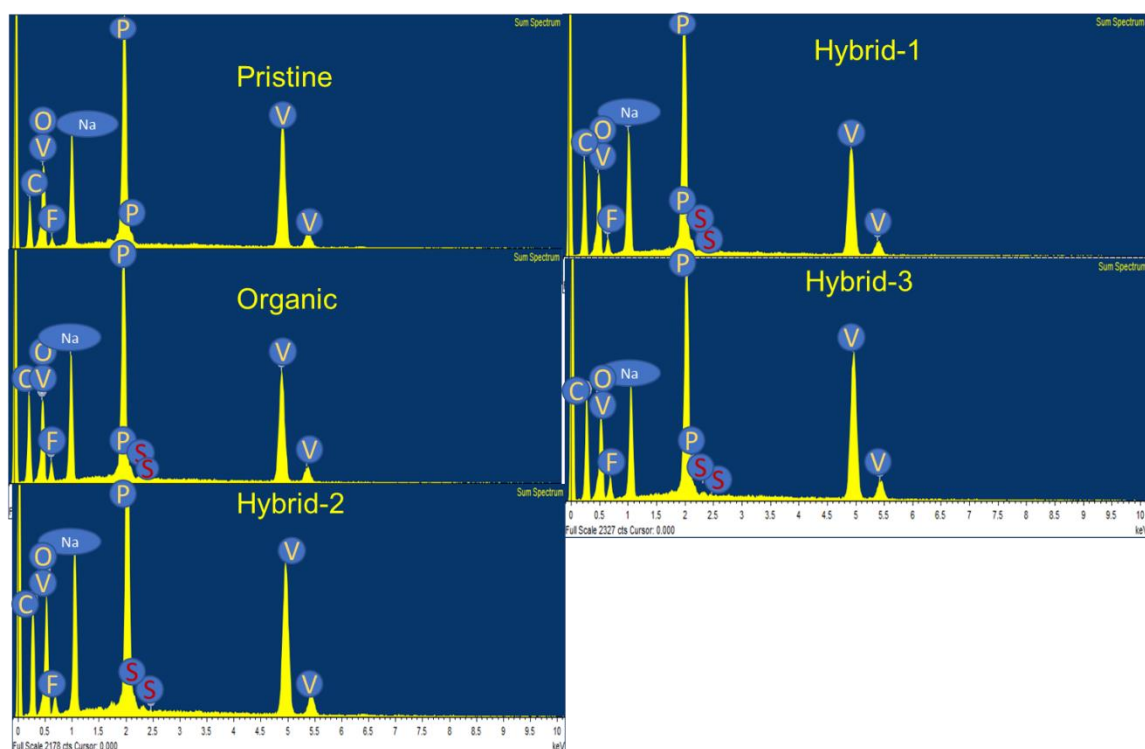


Figure 4. 10: EDX analysis of NVP@C electrode cycled with organic and hybrid electrolytes.

EDX analyses were used to identify elements on the NVP@C electrodes after 100 cycles (Figure 4.10). Sulphur traces were present on the surface of NVP@C electrode, probably from retained anion.

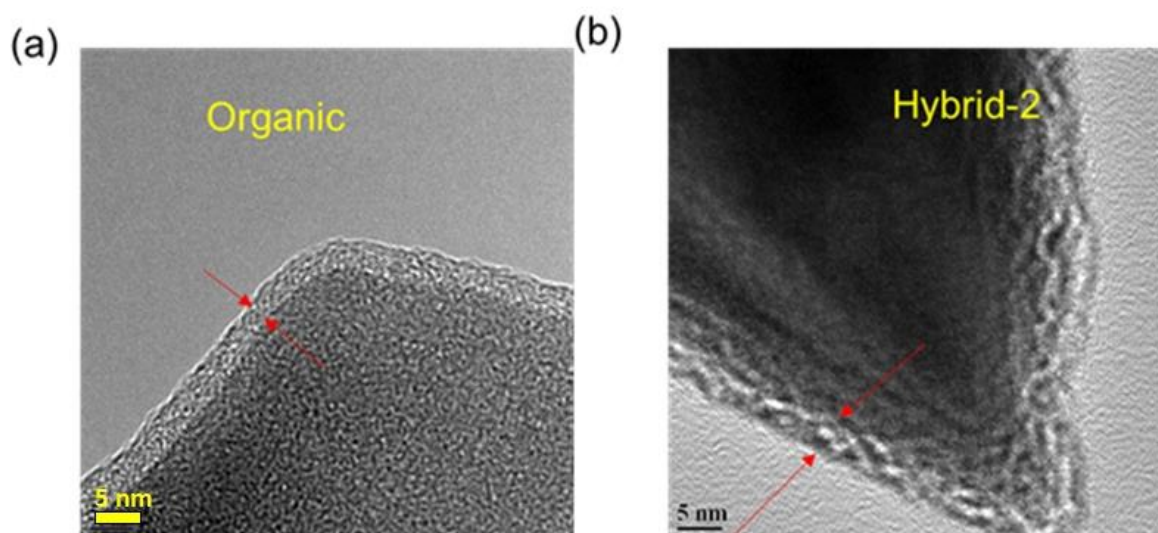


Figure 4. 11: HR-TEM images of NVP@C electrodes after cycling with (a) organic, and (b) hybrid-2 electrolyte.

HR-TEM images were obtained, as shown in Figure 4.11, and show clear differences between the passivation layer formation on the surface of NVP@C electrode with organic and hybrid electrolytes. Figure 4.11a shows that a uniform passivation layer has been formed on the surface of NVP@C electrode, as expected from the evidence of impedance spectrum (Figure 4.7 and Figure 4.8). Figure 4.11b shows a thinner SEI layer on the cathode (as compared to that in Figure 4.11a) with the organic electrolyte, as also observed in the impedance spectra in Figures 4.7 and 4.8.

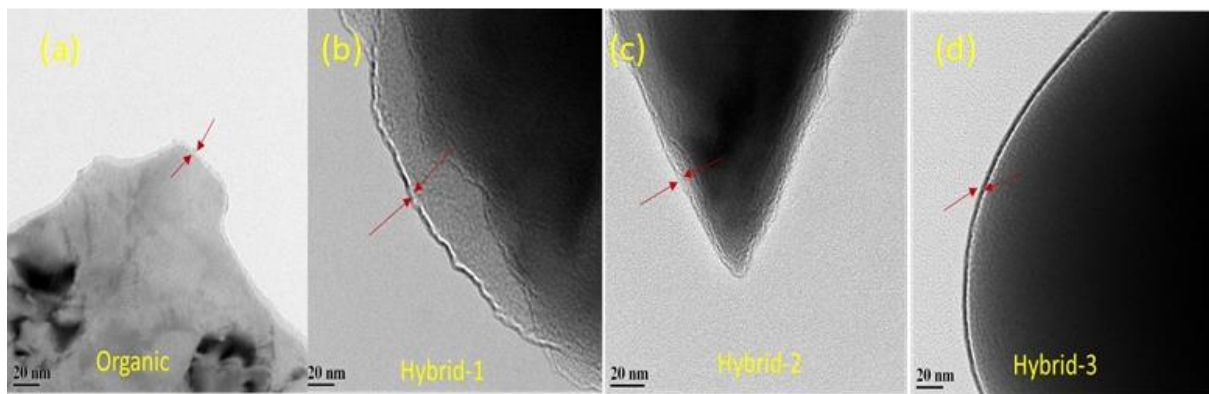


Figure 4. 12: HR-TEM images of Passivation layer on the surface of NVP@C electrode after cycling with (a) Organic, (b) Hybrid-1, (c) Hybrid-2 and (d) Hybrid-3 electrolyte.

It is proposed that in hybrid electrolytes the presence of ionic liquid may suppress the NaFSI-induced reaction on the surface of the cathode material (Figure 4.12) and prevent the electrolyte decomposition on the cathode surfaces (Table 4.1).

Table 4. 2: Different electrolyte compositions in sodium and lithium ion battery literature.

S.NO	Cell System	Solvent	Salt	Electro chemical Stability	Thermal Stability	Reference
1	Hard Carbon Na	EC:PC (1:1) wt%+10 wt% C ₃ mpyrTFSI	0.8M NaTFSI	<3.2V	<140 ⁰ C	160
2	NVP Na	EC:PC (50:50) wt%	1M NaClO ₄	0.1-5V	~100 ⁰ C	47
3	Na[Ni _{0.25} Fe _{0.5} Mn 0.25]O ₂ /C C- Fe ₂ O ₃	EMS + 2Vol% FEC	1M NaClO ₄	5.6V	~120 ⁰ C	175
4	Na _{0.7} CoO ₂ Na	EC:DMC (30:70) wt%	0.5M NaPF ₆	4.8V	~120 ⁰ C	176
5	NVP@C Na	EC:PC (1:1) v/v% :C ₃ mpyrTFSI	1M NaFSI	0.01-5V	>180 ⁰ C	Our work
6	LiFePO ₄ Li	EC:DEC (1:1)v/v% +38wt% C ₃ mpyrTFSI	1M LiPF ₆	4.8V	<90 ⁰ C	147
7	LiCoO ₂ Li	EC:DMC (1:1) v/v% + 40 wt% C ₃ mpyrTFSI	1M LiPF ₆	4.8V	<90 ⁰ C	151
8	LiFePO ₄ Li	PC:C ₄ mpyrTFSI	0.3M LiTFSI	4.1V	<128 ⁰ C	174

In lithium and sodium-ion batteries, hybrid electrolytes have previously shown good cycling performance, and thermal stability (Table 4.2). Furthermore a stable SEI layer on the surface of both cathode and anode were shown in these systems.^{83, 160, 173, 174} In our case the hybrid-2 and hybrid-3 electrolytes have shown a lower interfacial resistance, and a more stable SEI. In addition, a higher thermal and electrochemical stability is observed here in comparison to the literature.^{83, 171, 173, 174, 176}

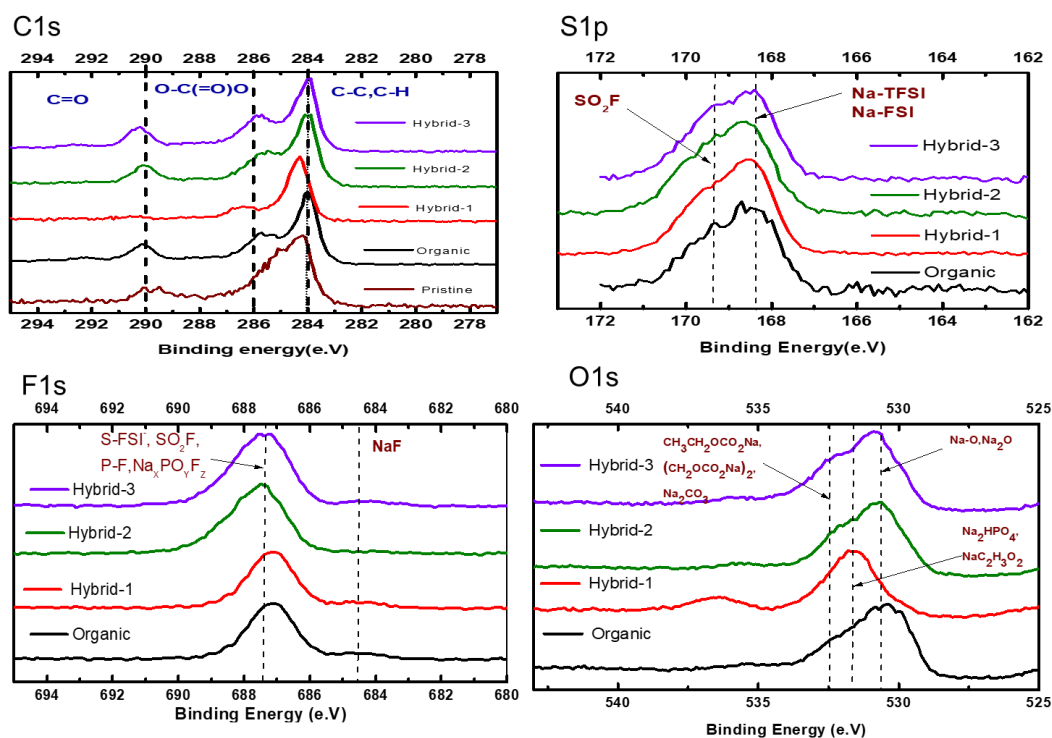


Figure 4. 13: XPS spectra of NVP@C cycled electrode with organic and hybrid electrolytes. XPS studies were used to identify the surface traces (Passivation layer composition or electrolyte decomposition products) on the surface of NVP@C electrodes after 100 cycles with organic and hybrid electrolytes (Figure 4.13). In the C1s spectrum, 284eV, 286eV and 290eV peaks are assigned to carbonates, sodium carbonates and alkyl carbonate, which are known to be major components of passivation film on the surface of NVP@C.^{171, 173} In the F1s spectrum, a peak at 687.4eV is assigned to S-FSI, $\text{Na}_x\text{PO}_y\text{F}_z$, P-F and NaF components, which arise from the organic electrolyte decomposition¹⁷¹. In the case of hybrid electrolytes, SO_2F and $\text{Na}_x\text{PO}_y\text{TFSI}$ peaks are assigned at the same peak position. These may come from ionic liquid ($\text{C}_3\text{mpyrTFSI}$) and the phosphate framework to form a passivation layer as observed in other systems.^{86 171, 173} In the S2p spectrum, 169.4eV and 168.5eV peaks are assigned to Na-TFSI, Na-FSI and SO_2F components of the passivation film on the surface of the electrodes cycled with hybrid electrolytes. In organic electrolytes, an Na-FSI peak is observed as a passivation film composition in other sodium electrolytes.^{171, 173} In the hybrid electrolytes, separate Na-FSI and Na-TFSI peaks are not observed in the XPS spectrum. In the O1s spectrum, peak positions

at 530.5 eV, 531.3 eV and 532.8 eV are assigned to Na₂O, Na-O, sodium bicarbonates, CH₃CH₂OCO₂Na₃, and sodium carbonate, as observed in other sodium cathodes with organic electrolytes.¹⁷¹ But in the case of hybrid electrolytes, an additional Na-TFSI peak is observed on the surface of the cathode which most likely arises from the anion in the ionic liquid (C₃mpyrTFSI) present in the hybrid electrolytes. This peak is overlapped with Na-FSI peak position in the XPS spectrum. In the case of hybrid electrolytes, these peaks show a higher intensity than in the organic electrolyte.

4.5 Summary:

In this work, we have successfully synthesized a cathode material, a NVP@C composite, for sodium-ion batteries, by an inexpensive synthesis route. This material displayed good cycling performance and high rate cycling stability with the conventional organic electrolyte. Further studies with hybrid electrolytes (mixtures of ionic liquid and organic-solvent-based electrolytes) showed good electrochemical performance with NVP@C composite material, and suppressed electrolyte decomposition on the surfaces of both the cathode material and the sodium metal. The hybrid-2 and hybrid-3 electrolytes also showed greater thermal stability, wider oxidative stability, higher specific capacity and more stable passivation layers, compared to the organic electrolyte, making them excellent candidates as potential electrolytes for sodium-ion batteries.

Chapter 5

Pure ionic liquid electrolytes development in high energy density sodium-ion batteries

5.1 Introduction:

Full-cell cycling performance of sodium-ion batteries with various cathodes with organic and ionic-liquid based electrolytes has been reported in the literature^{15, 109, 122, 180-185}. Ionic liquid-based devices need to improve their operating conditions, fabrication of devices, energy density, electrochemical performance, and formation of stable passivation layers on both electrodes for the commercialization of sodium ion batteries. NVP@C cathodes have been studied in the presence of various organic electrolytes¹⁸⁶ due to its high potential (3.4 V vs Na), high capacity (theoretical capacity = 117mAh/g) and good rate capability. However, to the best of our knowledge, a full cell combining the advantageous features of the NVP@C cathode combined with a hard carbon anode and an ionic liquid electrolyte has not yet been reported. In this work, we have used an NVP@C cathode material, synthesized by a simple and facile solid-state reaction developed in our laboratories¹⁸⁷, with a commercially-available hard carbon anode material. 1M NaFSI dissolved in N-Propyl-N-methyl pyrrolidinium bis(fluoromethanesulfonyl)imide (C₃mpyrFSI) is used as a state of the art ionic liquid electrolyte^{188, 189}. The IL supports extended cycling of the hard carbon, providing the basis for an energy density as high as 368 Wh/kg.

5.2 Hard carbon material characterization:

Commercial hard carbon used as anode material and synthesized from the glucose source at high temperature pyrolysis process. NVP@C material used as a cathode material and synthesized at our lab by solid state reaction process. Both materials are studied thoroughly with pure ionic liquid electrolytes to develop the high safe full sodium ion battery and detailed studied are briefly explained in the below sections.

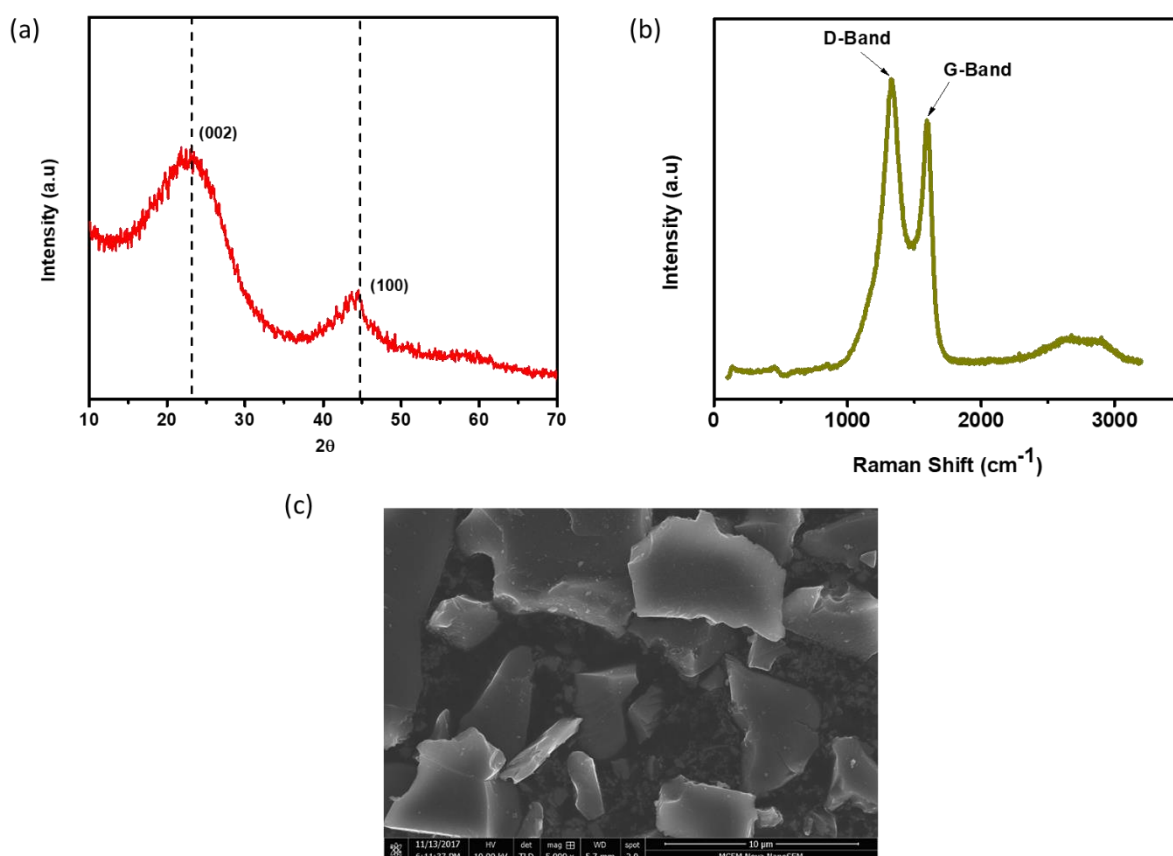


Figure 5. 1: Commercial hard carbon anode material morphology and structural information by (a) XRD, (b) Raman and (c) SEM.

Figure 5.1a shows the XRD pattern of commercial hard carbon anode material, which exhibited two broad peaks at 23° and 44° , corresponding to the (002) diffraction of the graphitic layer structures and the (101) diffraction of graphite, respectively¹²⁰. Moreover, the Raman spectrum shows two broad bands: the defect-induced band at 1335 cm^{-1} (D-band) and crystalline graphite band at 1587 cm^{-1} (G-band) (Figure 5.1b). The intensity of the I_G/I_D ratios was 0.94, indicating that the graphene sheets in the material are highly defective¹⁴. An SEM image of the hard carbon (Figure 5.1c) shows sheet-like particles, with a wide range of sizes, in the material.

5.3 Characterization of organic and ionic liquid electrolyte:

The thermogravimetric analysis (TGA) data for the organic (1M NaClO₄ in EC:PC (1:1)v/v) and ionic liquid electrolytes are shown in Figure 5.2. The organic electrolyte showed a significant mass loss of $>85\%$ when the temperature reached to 300°C , corresponding to the

evaporation of organic solvents (EC and PC). In contrast, the ionic liquid electrolyte showed a mass loss of >5% when the temperature reached at 300 °C, indicating their higher thermal stability.

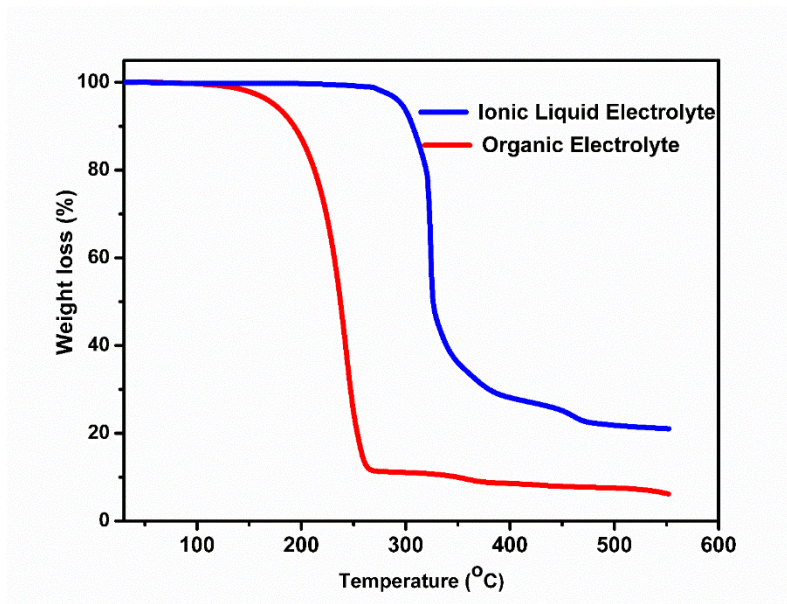


Figure 5. 2: TGA measurements for organic and ionic liquid electrolytes.

CV was used to evaluate the electrochemical oxidative stability for the electrolytes in contact with sodium metal (Figure 5.3). Ionic liquid electrolyte shows a higher oxidative stability (5.2 V vs. Na^+/Na) than does the organic electrolyte (4 V vs. Na^+/Na).

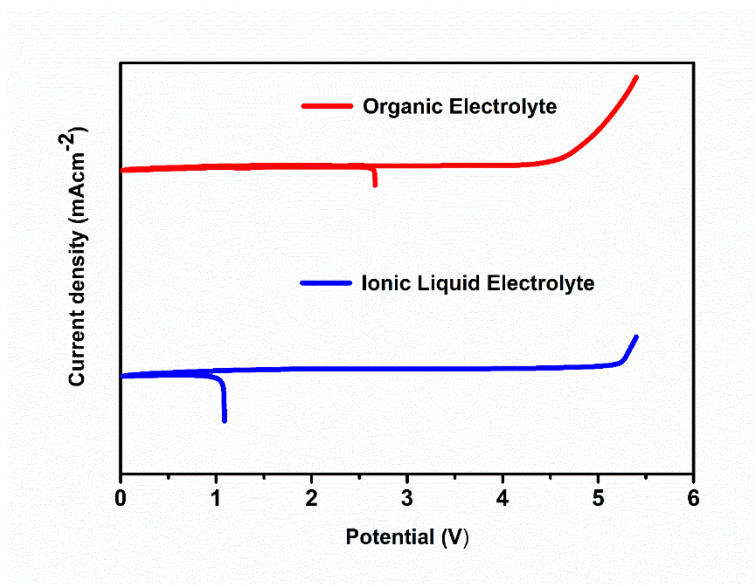


Figure 5. 3: Electrochemical oxidative stability tests were performed in three electrode swagelok cells at 10 mVs⁻¹ scan rate.

5.4 Electrochemical performance of NVP@C and hard carbon with Na metal:

Cyclic voltammetry of NVP@C cathode material with ionic liquid electrolyte shows clearly reversible oxidation and reduction of V^{3+}/V^{4+} at 3.45 V(oxidation) and 3.31 V(reduction) vs. Na/Na⁺ at a scan rate of 0.01 mVs⁻¹(Figure 5.4a). Figure 5.4b shows charge-discharge profiles, obtained at different rates, of NVP@C cathode material with ionic liquid electrolyte in a NVP@C||Na half-cell configuration. The discharge capacity values were 89, 85, 83, 82, 75, 79 and 60 mAhg⁻¹ at C/20, C/10, C/5, C/2, 1C, 2C, and 10C, respectively.

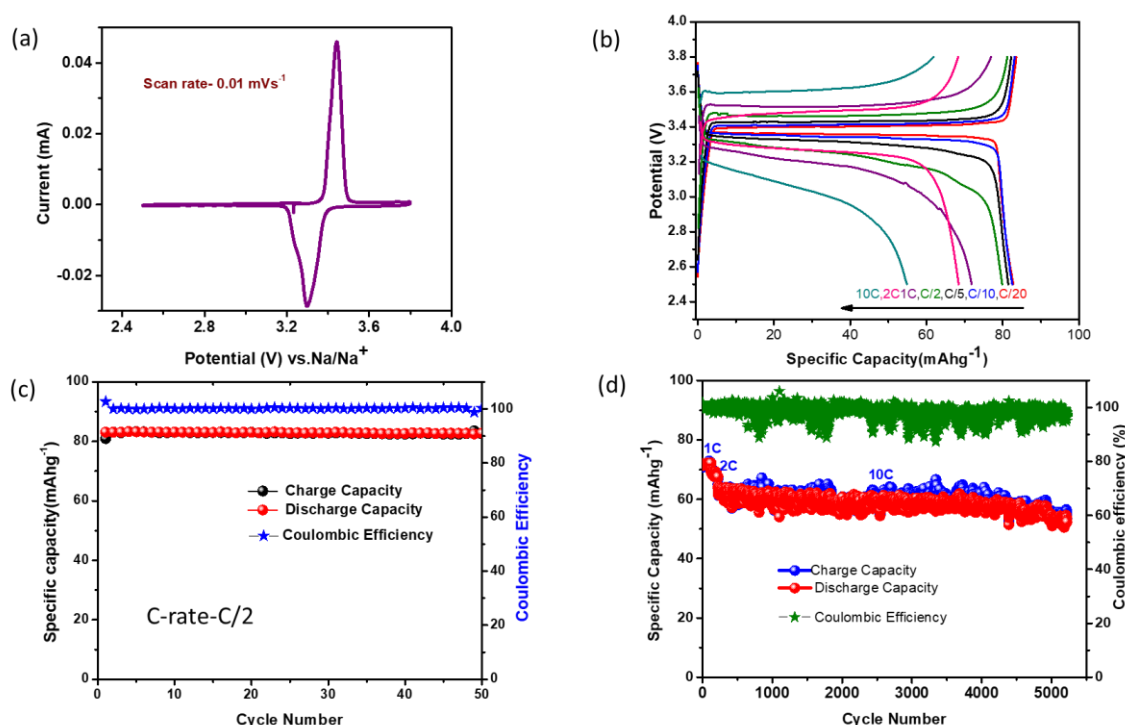


Figure 5. 4:Electrochemical characterization of NVP@C | Na metal cell with ionic liquid electrolyte: (a) Cyclic Voltammogram, (b) Potential vs. Specific capacity curves obtained at different rates for NVP@C|Na cell, (c) Charge-discharge cycling performance at C/2 rare for 50 cycles, and (d) charge-discharge cycling performance at different rates (1C, 2C and 10C) for 5000 cycles.

These capacity values are lower than the theoretical capacity (117mAhg⁻¹) of NVP@C cathode material, probably because of the high charge transfer resistance values of ionic liquid electrolyte with sodium metal at room temperature¹¹⁷. NVP@C electrode exhibited excellent charge-discharge cycling performance at the C/2 rate for 50 cycles (Figure 5.4c), as

characterized by stable cycling with consistent capacity values of 83 mAhg⁻¹, 99% capacity retention and close to >99% coulombic efficiency.

The NVP@C || Na half-cell system was subjected to extended cycling with IL electrolyte for a total of 5000 cycles: at rates of 1C (for 100 cycles), 2C (for 100 cycles), and 10C (for 4800 cycles). This material showed excellent reversibility and consistent capacity values, with an impressive 99% average coulombic efficiency, even after 5000 cycles (Figure 5.4d).

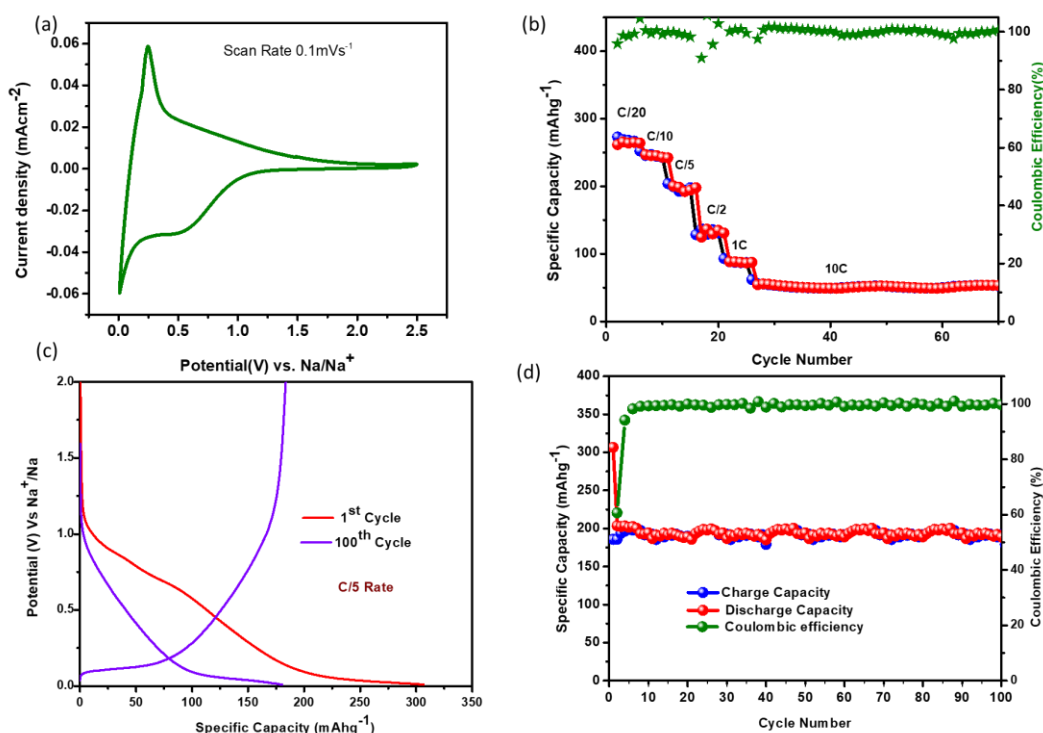


Figure 5. 5:Electrochemical performance of hard carbon | Na cell with ionic liquid electrolyte (a) Cyclic voltammetry performed at a scan rate of 0.1 mVs⁻¹, (b) The charge-discharge cycling performance of hard carbon at different rates in the potential range of 0.01 to 2V vs Na/Na⁺,(c) Potential versus Capacity plot of hard carbon anode material for first and 100th cycle, (d) Charge-discharge cycling performance of hard carbon for 100 cycles at C/5 rate in the potential range of 0.01 to 2V vs Na/Na⁺.

Figure 5.5 shows similar electrochemical performance measurements for the hard carbon || Na cell with ionic liquid electrolyte. The cyclic voltammetry of hard carbon was performed at 0.1 mVs⁻¹ scan rate in the potential interval of 0.01 to 2.5 V vs. Na/Na⁺ (Figure 5.5a). The hard carbon anode material shows peaks at 0.5 V and 0.01 V vs. Na/Na⁺, which are related to the insertion and adsorption mechanism of sodium on the electrode material in SIBs^{14, 121}. This

electrode material was then subjected to charge-discharge cycling at different rates with IL electrolyte, and showed discharge capacity values of 258, 250, 200, 150, 100, 50 mAhg⁻¹ at C/20, C/10, C/5, C/2, 1C, and 10C rates, respectively (Figure 5.5b). It shows that excellent rate capability and good capacity retention of 99% with ionic liquid electrolyte, and followed the similar trend with organic electrolyte^{167, 190}. Figure 5.5c and 5.5d show the charge-discharge cycling performance of hard carbon with sodium metal at the C/5 rate for 100 cycles in the potential range of 0.01 to 2 V vs. Na/Na⁺. The potential versus capacity plot shows that the first charge capacity value is less than the first discharge capacity, due to the formation of a solid electrolyte interface (SEI) on the surface of hard carbon. During the subsequent cycles, the capacity values stabilized and showed stable capacity values up to 100 cycles (Figure 5.5d).

5.5 Electrochemical performance of NVP@C||Hard carbon full cell:

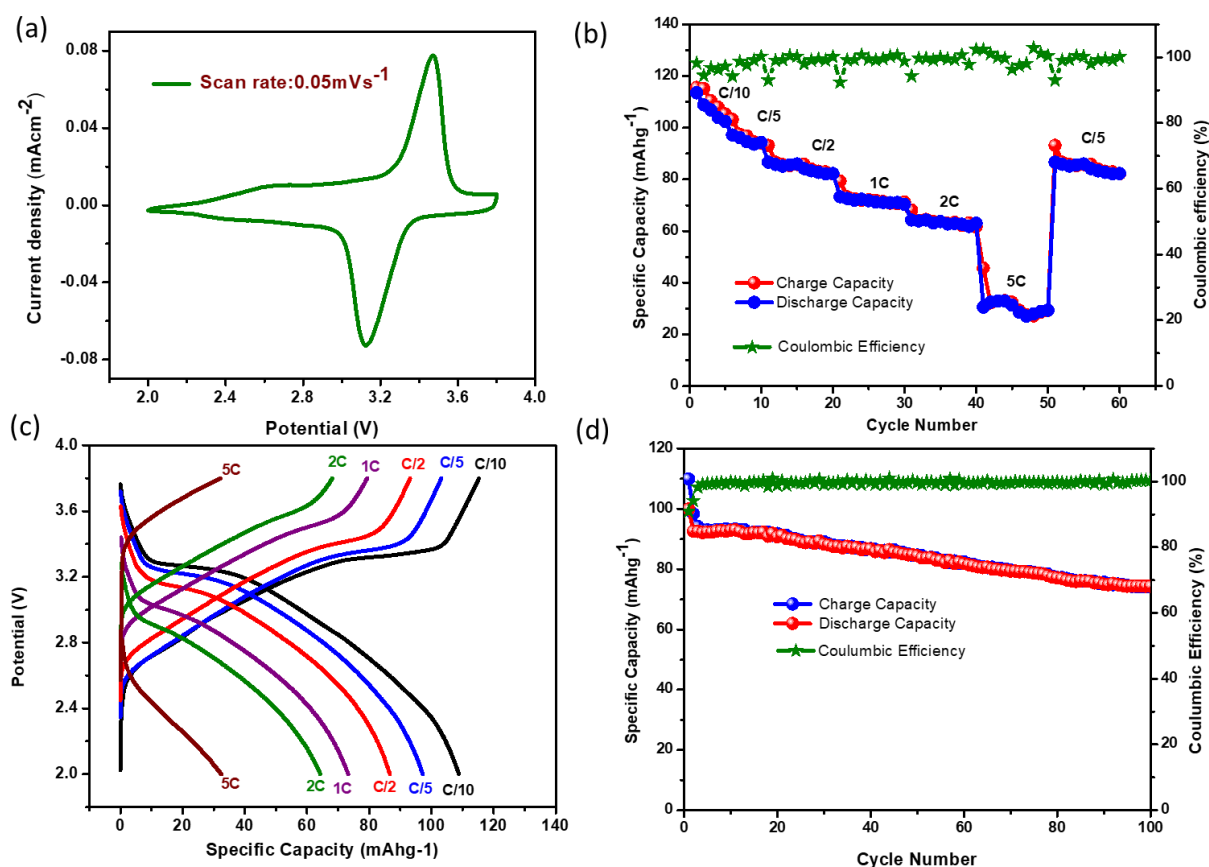


Figure 5. 6: Electrochemical characterization of NVP@C | hard carbon cell with IL electrolyte for (a) Cyclic voltammogram, (b) Charge-discharge cycling performance of full cell with IL electrolyte at different current density rates, (c) Potential vs. specific capacity curve at different

current density rates for NVP@C | hard carbon full cell, and (d) Charge-discharge cycling performance at C/2 rate for 100 cycles

Based on the above results, NVP@C and hard carbon electrode materials are suitable candidate cathode and anode materials for a full cell SIB. Charge-discharge cycling performance of full cell was investigated under galvanostatic conditions at room temperature in the potential window of 2 to 3.8 V. Figure 5.6a shows a cyclic voltammetry curve for NVP@C// Sodium ion intercalated hard carbon full cell at a scan rate of 0.05 mVs⁻¹. This curve shows two well-defined redox couples at 3.35 V (cathode sweep) and 3.28 V (anode sweep), consistent with the reported literature¹⁹⁰. The rate capability test of the full cell is shown in Figure 5.6b. As the rate changed (from C/10, through C/5, C/2, 1C, 2C, to 5C), capacity values change from 110 to 35 mAhg⁻¹ based on the cathode mass. Figure 5.6c shows a capacity versus potential plot, which highlights the polarization loss of the full cell at different currents. Capacity decreased with increasing current, and polarization loss between charge and discharge curves also increased. These trends were observed in some other SIB systems¹⁹⁰. Figure 5.6d shows the charge-discharge cycling performance, and coulombic efficiency tests at a rate of C/2. This corresponds to a capacity retention value of 66%, which is better than that for an organic-electrolyte (57%) based full cell room temperature SIB¹⁹⁰.

5.6 SEI characterization of NVP@C and Hard carbon:

Electrochemical impedance spectroscopy studies were performed for NVP@C| hard carbon, NVP@C|Na, and hard carbon|Na cells cycled with ionic liquid electrolyte at C/5 rate and are shown in Figure 5.7. At OCV, the NVP@C| hard carbon cell shows a smaller charge-transfer resistance compared to those of the other two cells (which contain Na metal), (Figure 5.7a). This implies that the charge-transfer resistance values are high for NVP@C|Na and hard carbon|Na cells, because of formation of a more resistive passivation film on sodium metal with ionic liquid electrolyte when operated at room temperature, as has previously been observed in ionic-liquid electrolyte based sodium batteries¹¹⁷. After 100 cycles, the NVP@C|

hard carbon full cell shows a increased charge transfer resistance (R_{ct} :1000 ohm), as compared to after 5th (R_{ct} : 200 ohm) and 50th (R_{ct} : 500 ohm) cycles (Figure 5.7b–d). This may be the root cause of capacity fade, since it implies irreversible loss of sodium on hard carbon material, which would then cause insufficient sodium to be available for insertion into NVP@C cathode material in later cycles in a full cell SIB (Figure 5.7).

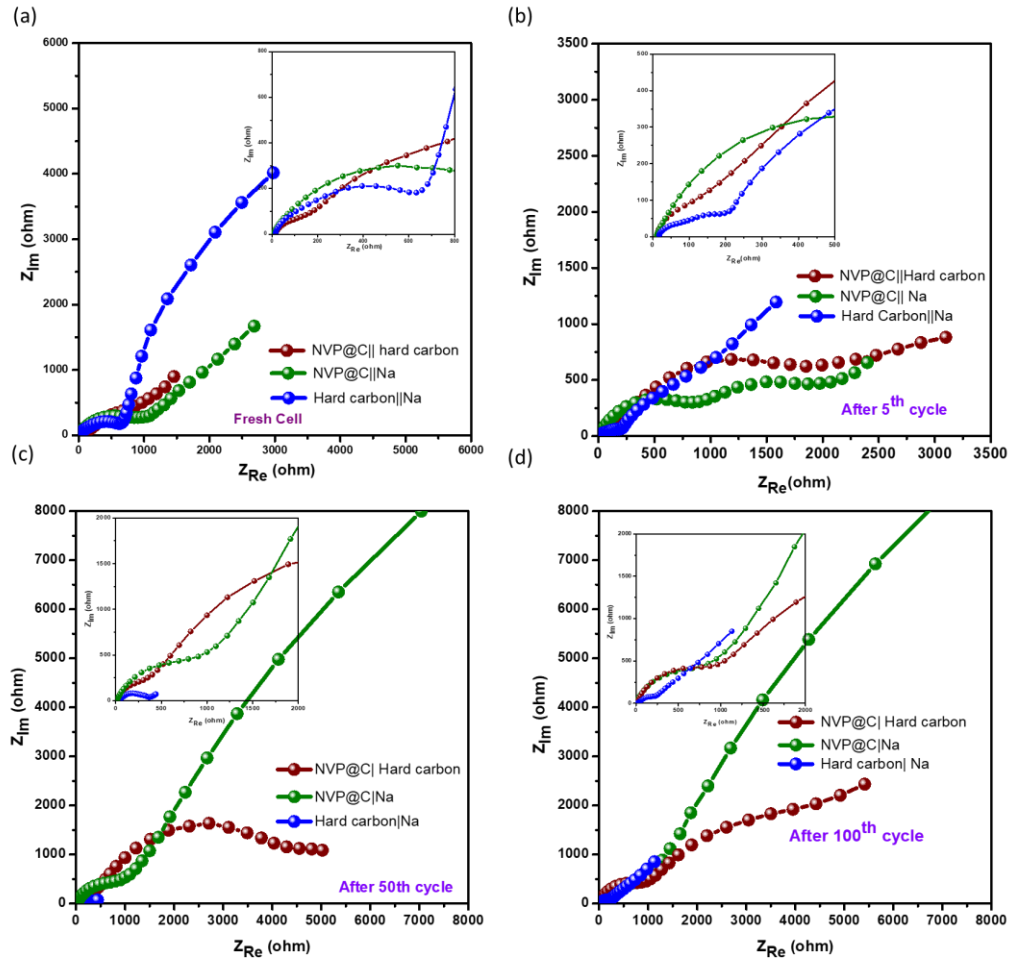


Figure 5. 7: Electrochemical impedance measurements for NVP@C| Na, Hard carbon| Na, and NVP@C| Sodiated Hard carbon cell at (a) OCV, (b) after 5 cycles, (c) after 50 cycles, (d) after 100 cycles with ionic liquid electrolyte.

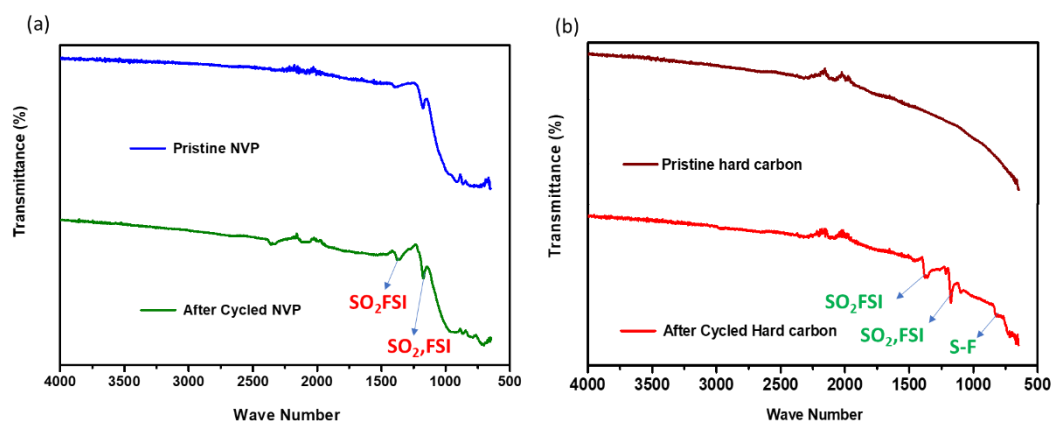


Figure 5. 8:Ex situ FTIR spectra of electrodes extracted from NVP@C | Sodiated Hard carbon cells. (a) NVP@C, pristine and after 100 cycles; (b) hard carbon, pristine (not sodiated) and after 100 cycles.

FTIR spectra (Figure 5.8) were collected for fresh NVP@C and hard carbon electrodes, and also after the electrodes had been cycled with IL electrolyte for 100 cycles at C/2 rate. There are significant differences between the spectra of the fresh and cycled NVP@C electrode surfaces. It shows a composition of the (SO₂F&FSI), and SO₂FSI peaks at 1184, 1368 cm⁻¹ based SEI layer compositions on the surface of electrode material (Figure 5.8a). Both peak differences are explained in more detail in the subsequent table. Figure 5.8b showed clear differences in the spectra of fresh and cycled hard carbon electrodes, and includes peaks corresponding to SEI components SO₂F, SO₂FSI, and S-F at 1184, 1368 and 820 cm⁻¹, respectively on the electrode surface.

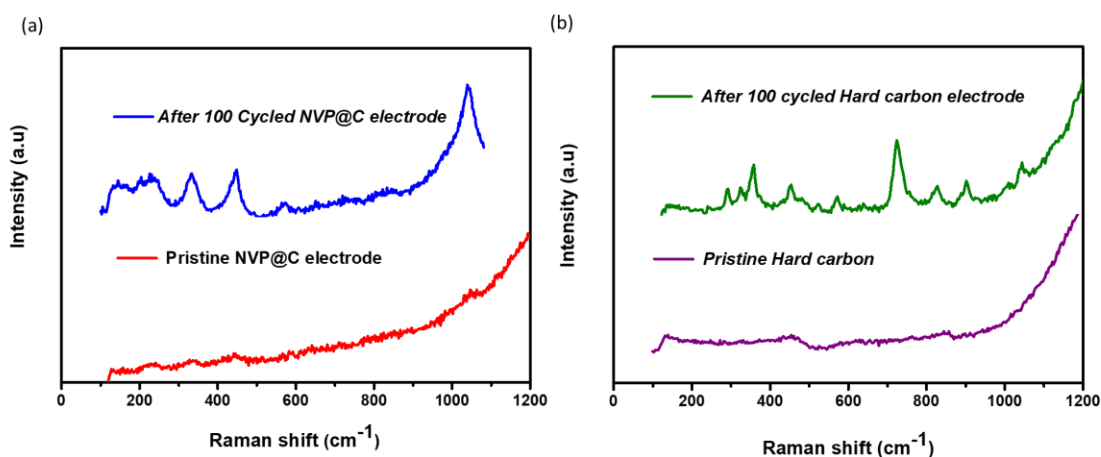


Figure 5. 9:Raman spectra of electrodes from NVP@C | sodiated hard carbon cells. (a) NVP@C, pristine and after 100 cycles, (b) hard carbon, pristine (not sodiated) and after 100 cycles.

Raman spectra were collected from NVP@C and hard carbon electrodes extracted from cells after 100 cycles with IL-based electrolyte, and are shown in Figure 5.9. The Raman peak positions are listed in Table 4.1 and assigned to different components of the SEI layer, which forms through reaction of the electrode surfaces with the IL electrolyte during cycling. This layer is critical to protect the electrodes and electrolyte from further degradation.

Table 5. 1: Listing of Raman peaks and their assignments for the spectra of the SEI layers on NVP@C and hard carbon electrodes after cycling with IL electrolyte.

NVP@C electrode SEI composition's	
Raman Shift(cm ⁻¹)	Assigned to the compositions
1039	H-F
833	S-F, SO ₂ FSI
563	S-F
447	S-S
332	C-H
231	C-N
Hard carbon electrode SEI composition's	
Raman Shift(cm ⁻¹)	Assigned to the compositions
1214	C-C
1126	SO ₂
1082	CF ₂
1038	S-O
968	C-H
902	C-F,S-F
724	S-C,C-F

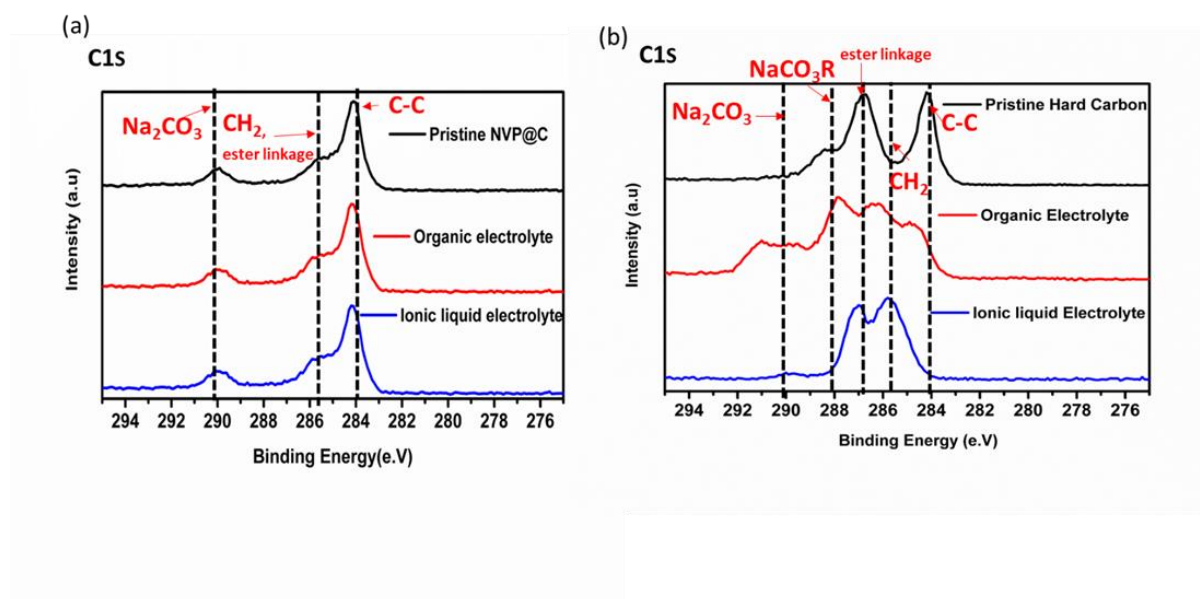


Figure 5. 10: XPS spectra for pristine and after 100 cycles with organic and ionic liquid electrolytes for (a) NVP@C and (b) HC electrodes.

XPS studies were used to identify the surface traces on the surface of NVP@C and hard carbon electrodes after 100 cycles with organic (1M NaClO_4 in EC:PC (1:1)v/v) and ionic liquid electrolytes (Figure 5.11). In the C1s spectrum, 284eV, 286eV, and 290eV peaks are assigned to carbonates, sodium carbonates and alkyl carbonate, which are known to be major components of SEI film on the surface of NVP@C and hard carbon.^{171, 173} There is a significant difference in the hard carbon XPS spectra, shown in Figure 5.11b. The organic electrolyte forms an SEI film based on $\text{O}-\text{C}=\text{O}$ and Na_2CO_3 components on the surface of hard carbon; such a film is known to cause unfavorable Na^+ ion transport and side reaction of the electrolyte^{187, 191}, lead to the poor cycling performance of the sodium ion battery. The ionic liquid controlled the carbonate-based SEI films on the surface of hard carbon (Figure 5.11b) and showed the excellent cycling performance of full cell sodium ion battery.

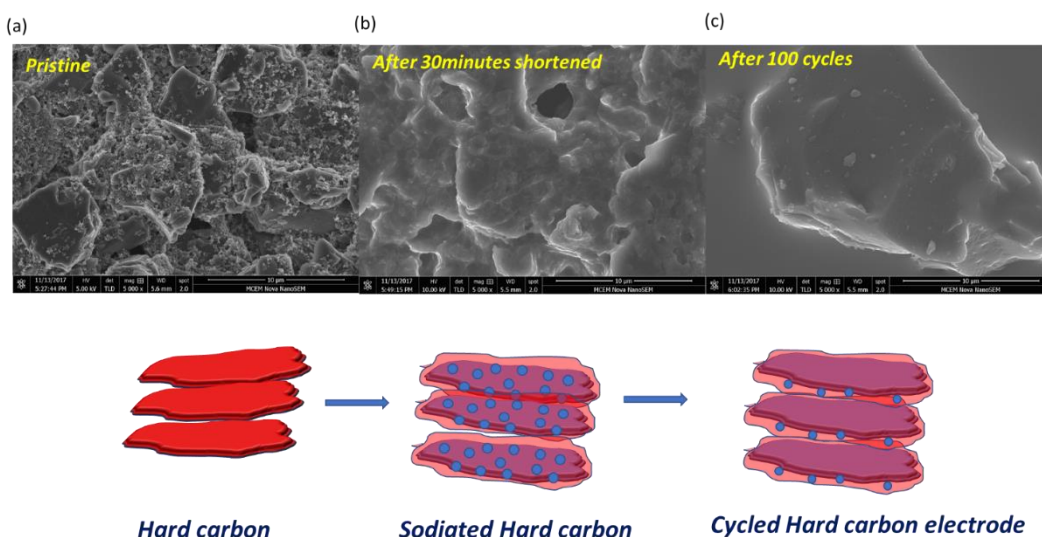


Figure 5. 11:FEG-SEM of hard carbon (a) in pristine state, (b) Sodiated Hard carbon (i.e. after 30 minutes in contact with Na metal wet with IL electrolyte), and (c) after 100 cycles in a cell comprising NVP@C| Sodiated hard carbon.

FEG-SEM images of hard carbon electrode material at various stages of cell life (pristine, sodiated, and after 100 cycles in a full cell SIB with IL electrolyte) are shown in Figure 5.11. The pristine hard carbon electrode has sheet-like particles, which appear uniformly dispersed with the binder (CMC) and carbon black (Figure 5.11a). This electrode was then sodiated (a sodium metal surface was wet with electrolyte, and the hard carbon electrode placed on this surface and left for 30 minutes) to increase the sodium availability, and coulombic efficiency in the initial cycle with NVP@C cathode material in a SIB. After sodiation, the electrode morphology changed, probably due to the formation of a passivation layer on the electrode surface (Figure 5.11b). The sodiated hard carbon electrode was used as an anode in a SIB (along with NVP@C cathode material and IL electrolyte) and the cell was cycled for 100 times. After cycling, the electrode morphology is different again as compared to previous state of hard carbon electrode and is shown in Figure 5.11c. The IL-based electrolyte forms a uniform passivation layer on both electrode surfaces and enhances the cycling performance of the SIB.

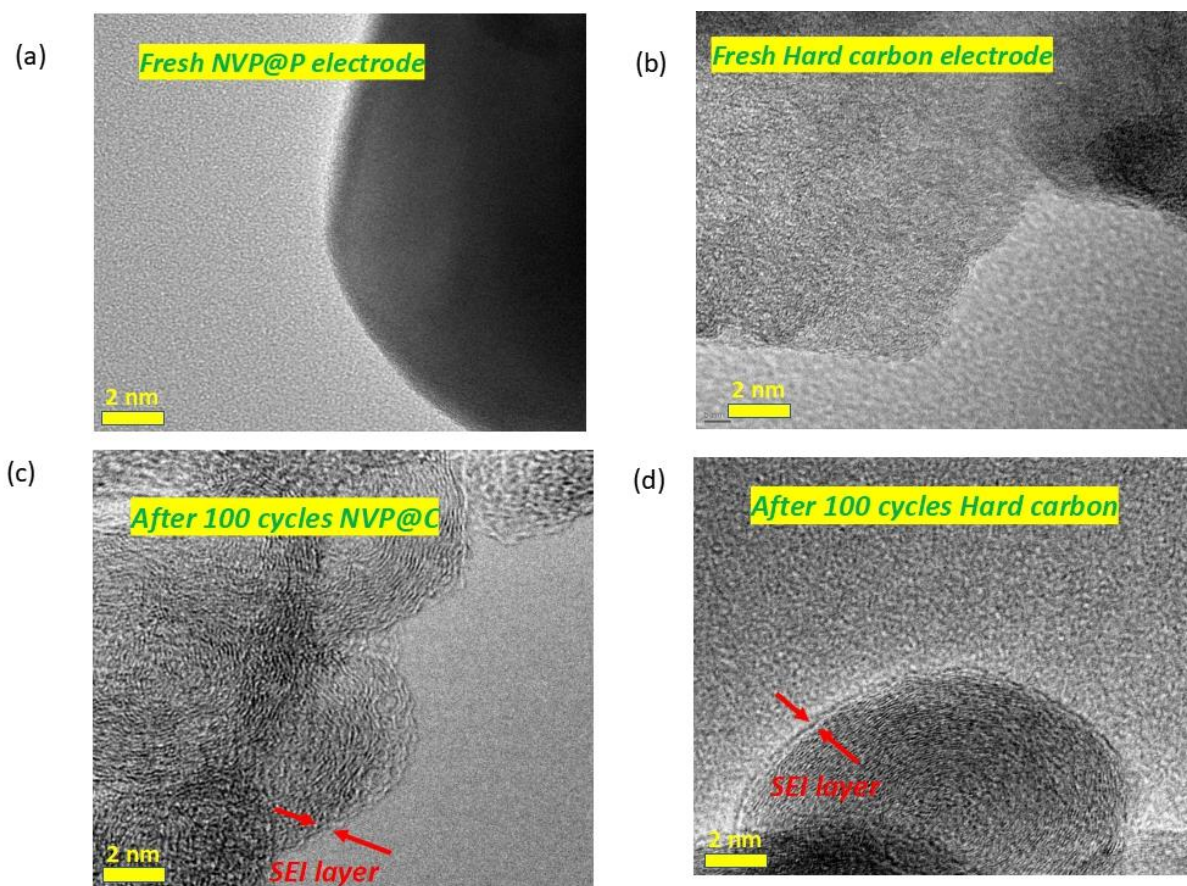


Figure 5.12: HR-TEM images of (a) Pristine NVP@C, (b) Pristine Hard carbon (not sodiated), (c) NVP@C electrode after 100 cycles, and (d) Hard carbon electrode after 100 cycles.

HR-TEM images obtained for NVP@C and hard carbon electrodes before and after 100 cycles with IL electrolyte are shown in Figure 5.12. Both electrodes showed a uniform passivation layer on their surfaces after cycling, (Figure 5.12c and Figure 5.12d), in contrast to the surfaces before cycling (Figure 5.12a and 5.12b). The passivation layer that forms on the hard carbon electrode appears to be thicker than that formed on the NVP@C electrode. It means that IL electrolyte forms more passivation layer on the surface of hard carbon due to the electrolyte reaction with different heterogeneous atoms (C, H, N, O) in hard carbon and more sodium deposition on the surface electrode surface^{120, 183}. This could explain why SIBs that contain hard carbon anodes generally show capacity fading, regardless of the choice of cathode; it could also explain why electrolyte additives do not solve the capacity fade problem. Similar capacity fade trends are observed in our present work, although our full SIB outperforms other SIBs

containing IL- or organic solvent-based electrolytes, as shown in Table 5.2. The NVP@C and hard carbon-based cathode and anode materials gave a 3.3V full cell SIB with IL electrolyte, which was able to power an LED study lamp in a demonstration with a 2032-coin cell (Figure 5.13).



Figure 5. 13:NVP@C| Pre-sodiated hard carbon full sodium-ion battery prototype demonstration video, showing an LED study lamp with a 2032-coin cell.

Table 5. 2 : Summary of electrochemical performance of various sodium-ion batteries.

Sodium systems	Voltage (V)	Nominal Voltage(V)	Specific Energy (Whkg ⁻¹)	Capacity Retention (%)	Reference
NVP@C/1M NaClO₄ in EC:PC +2wt% FEC/Hard carbon	2–3.8	3.3	363 _C (0.5C)	57%(1–100)	190
O3-Na_{0.5}Cu_{0.22}Fe_{0.3}Mn_{0.48}O₂ / 0.8M NaPF₆ in EC / DMC (1:1)v/v /HC	1–4.05	3.2	210 _{A+C} (0.05C)	>95%(1–100)	45
P2-Na_{7/9}CuO_{2/9}Fe_{1/9}Mn_{2/3}O₂ / 1M NaClO₄ in EC / DEC(1:1) v/v /HC	1–4.2	3.5	195 _{A+C} (0.02C)	89%(1–50)	192
P2-Na_{2/3}Ni_{1/3}Mn_{2/3}O₂/1M NaClO₄ in EC:PC (1:1)v/v+5wt% FEC/Sb	1.4–4.0	2.9	130 _{A+C} (0.5C)	94%(1–110)	193
P2-Na_{0.7}CoO₂/ 1M NaClO₄in TEGDME/Graphite	0.5–3.7	2.2	60 _{A+C} (0.175C)	80(1–1250)	194

Symmetrical P2-Na_{0.6}Cr_{0.6}Ti_{0.4}O₂ /1M NaClO₄ or 0.8M NaPF₆ in EC:DEC(4:6)v/v	1.5–3.0	2.5	82 _{A+C} (0.106C)	84(1–100)	195
Na₃V₂(PO₄)₃/1M NaPF₆ in DEGDME/graphite	0.7–4.2	2.9	120 _{A+C} (0.1C)	70(1–250)	196
Na₂FeP₂O₇/1M NaClO₄ in PC+2vol% FEC/C-Fe₃O₄	1.1–4.2	2.3	142 _{A+C} (0.01C)	93.3(1–100)	197
NaFePO₄ /NASICON-based hybrid solid electrolyte/HC	1.5–4.0	2.6	312 _{A+C} (0.2C)	96(1–200)	198
R-Na_{2x}MnHCF/1M NaClO₄ in DEC/EC(1:1)+10wt% FEC/HC	1.5–3.8	3.2	448 _C (0.1C)	95(2–25)	107
P2/P3/O2-Na_{0.76}Mn_{0.5}Ni_{0.3}Fe_{0.1}Mg_{0.1}O₂/1M NaPF₆ in PC/HC	2–4.2	3.3	180 _{A+C} (0.09C)	80(1–700)	183
NVP@C/1M NaFSI in P₁₃FSI/HC	2–3.8	3.3	368 _C (0.5C)	66(1–100)	Our work*

5.7 Summary:

In summary, we have developed a high energy-density, high rate capability, safe and easy to fabricate NVP@C|| hard carbon full-cell sodium ion battery, with 1M NaFSI in C₃mpyrFSI electrolyte. Studies of the individual electrodes in the electrolyte found that the NVP@C cathode material shows stable, fast and consistent cycling performance – retaining a 99% coulombic efficiency at a 10C rate for at least 5000 cycles. In the full cell, using sodiated hard carbon (obtained by wetting the carbon with electrolyte and then bringing it into contact with sodium metal) improved the initial coulombic efficiency. In the full cell sodium-ion battery, the ionic liquid electrolyte formed a stable and uniform passivation layer on the surfaces of both electrodes. Compared to other battery systems, our full cell showed high safety, high energy density (368Whkg⁻¹) and outperformed the others. A 2032-coin cell sodium ion battery with ionic liquid electrolyte lit the prototype LED study lamp at full light intensity.

Chapter 6

Ionic liquid added electrolytes improve the physio-chemical properties and stabilize the SEI layer in sodium batteries

6.1 Introduction

Much research is underway on cathodes, anodes, and electrolytes for development and commercialization of sodium-ion batteries^{59, 199}. In all batteries the electrolyte plays a significant role in determining the cycling performance. Aqueous electrolyte-based sodium-ion batteries are restricted to lower power and energy density¹¹⁷, and are unsuitable for commercial grid-storage applications. The most-used electrolytes consist of a sodium salt dissolved in organic carbonate solvents⁵⁷, and have some significant disadvantages, including low thermal stability, high volatility and being flammable, which diminished their potential safety in manufacturing operations and large scale use⁹.

Ionic liquids have been used as novel battery electrolytes because their physio-chemical and electrochemical properties can solve some of the above issues in respect of sodium-ion batteries⁸⁷. In particular, pyrrolidinium cations (C3mpyr & C4mpyr) with different anions (TFSI & FSI) as ionic liquid electrolytes have shown excellent electrochemical performance at room temperatures in sodium ion batteries^{160, 200-202}. However, pure ionic-liquid based electrolytes are not especially effective in sodium-metal batteries, due to their low ionic conductivity and high charge-transfer resistance when stripping and plating with sodium metal^{117, 203}. “Hybrid” electrolytes, mixtures of ionic-liquid and organic-solvent based electrolytes, have been introduced and used in lithium- and sodium-ion batteries^{60, 147, 151, 152}. They can show excellent electro chemical performance and compatibility with cathode and anode materials as well as enhancing thermal stability compared to pure carbonate based electrolytes¹⁶⁰. The solid electrolyte inter-phases (SEI) formed on both cathode and anode materials with organic, hybrid

and ionic liquid electrolytes have been characterized^{204, 205}. Here, we probe more deeply the properties of these hybrid electrolytes compared to the pure carbonate or ionic liquid solvents. Thermal stability is probed by examining the gaseous products on thermal decomposition. Their electrochemical performance is also evaluated in Na|Na symmetrical and NVP@C|Na cells for 100 cycles at room temperature. Surface passivation layer studies are performed and the morphology and composition of the SEI layers examined by FEG-SEM and ATR-FTIR techniques.

6.2 TGA-IR studies of organic, hybrid and ionic liquid electrolytes:

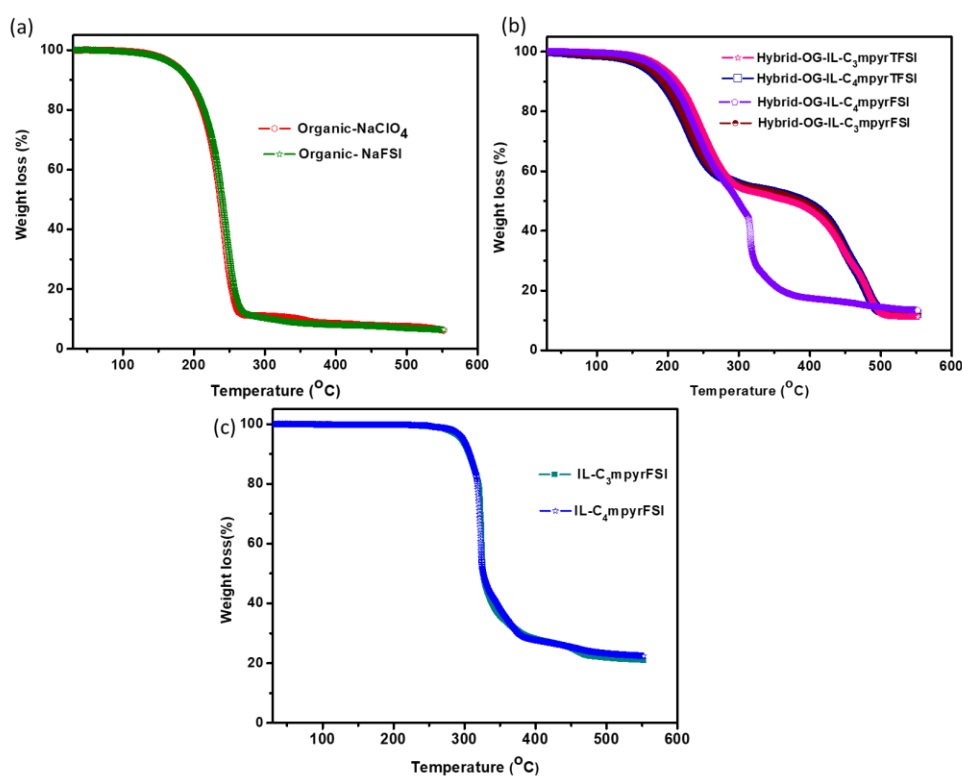


Figure 6. 1:TGA curves of (a) organic, (b) hybrid, and (c) ionic liquid electrolytes.

The thermogravimetric analysis traces for the organic, hybrid and ionic liquid electrolytes are shown in Figure 6.1. The organic electrolytes showed a significant weight loss, >85% before 260°C, attributed to evaporation of the organic solvents. The hybrid electrolytes had considerably lower weight loss, <35% by 260°C, demonstrating that the thermal stability of

the electrolytes increased when the ionic liquids were added. All of the hybrid electrolytes show a plateau beginning at $\sim 260^{\circ}\text{C}$ which indicates the completion of the evaporation of the organic solvents²⁰⁶. This result clearly states that the addition of ionic liquid to conventional electrolytes, increased the thermal stability of the electrolytes in sodium systems. Similar findings were observed in other battery systems^{174, 207}.

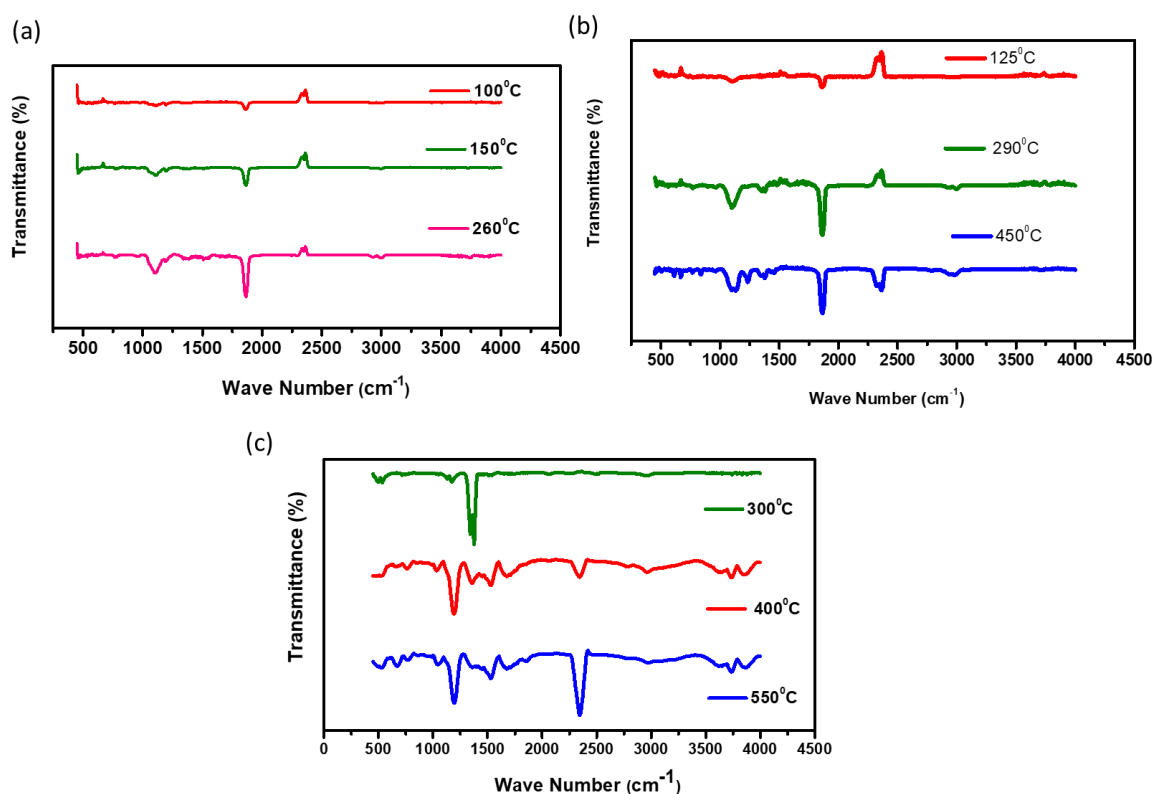


Figure 6. 2: Gaseous thermal decomposition products detected by FTIR spectra for (a) organic, (b) hybrid, and (c) ionic liquid electrolytes.

Figure 6.2 shows the FTIR spectra of the gaseous products obtained from organic, hybrid and ionic liquid electrolytes at particular temperatures (corresponding to significant stages in the weight-loss data for each electrolyte). Peaks are collated and assigned in Table 6.1. In the organic electrolyte, first NaFSI salt decomposed to form NaF and CF_2SO_3 products^{208, 209}. at higher temperatures the organic solvents (EC and PC) evaporated, resulting in the significant weight loss of 85% by 260°C . The remaining residue in the pan should be NaF, carbon and

Sulfur compounds based solid products (Figure 6.2a). The FTIR spectra of the gaseous decomposition products obtained during thermal analysis of the hybrid electrolyte show good agreement with the spectra obtained for the organic electrolyte up to 260°C; again, these spectra are related to decomposition of the sodium salt and organic solvent. Further increasing the temperature of the hybrid electrolyte to 500°C led to some additional peaks in the FTIR spectrum, which are related to ionic liquid decomposition products (Figure 6.2b). In contrast, there was no significant weight loss for the ionic liquid electrolyte at 260°C – the decomposition reaction of NaFSI salt has been shifted to 300°C. The FTIR spectra of the decomposition products of the ionic liquid electrolyte are significantly different from those of the other electrolytes (Figure 6.2c).

Table 6. 1 : FTIR peaks assigned to gaseous decomposition products from organic, hybrid and ionic liquid electrolytes.

Decomposition gaseous products of Organic electrolyte	
Wavenumber (cm ⁻¹)	Assigned to functional groups
1876	C=O
1544	C=O
1372	S=O, C-H, O-H
1192	C-O, C-N
1116	C-O
Decomposition gaseous products of Hybrid electrolyte	
2368	O=C=O
1856	C=O
1374	S=O, O-H, C-H
1246	C-N (stretching vibrations)
1106	C-O
838	C=C
Decomposition gaseous products of Ionic liquid electrolyte	
3882, 3742	O-H
2974	C-H
2348	O=C=O
1874, 1706	C=O
1520	N-O
1368	C-H, S=O, O-H
1184, 1038	S=O, C-O
778, 672	C=C

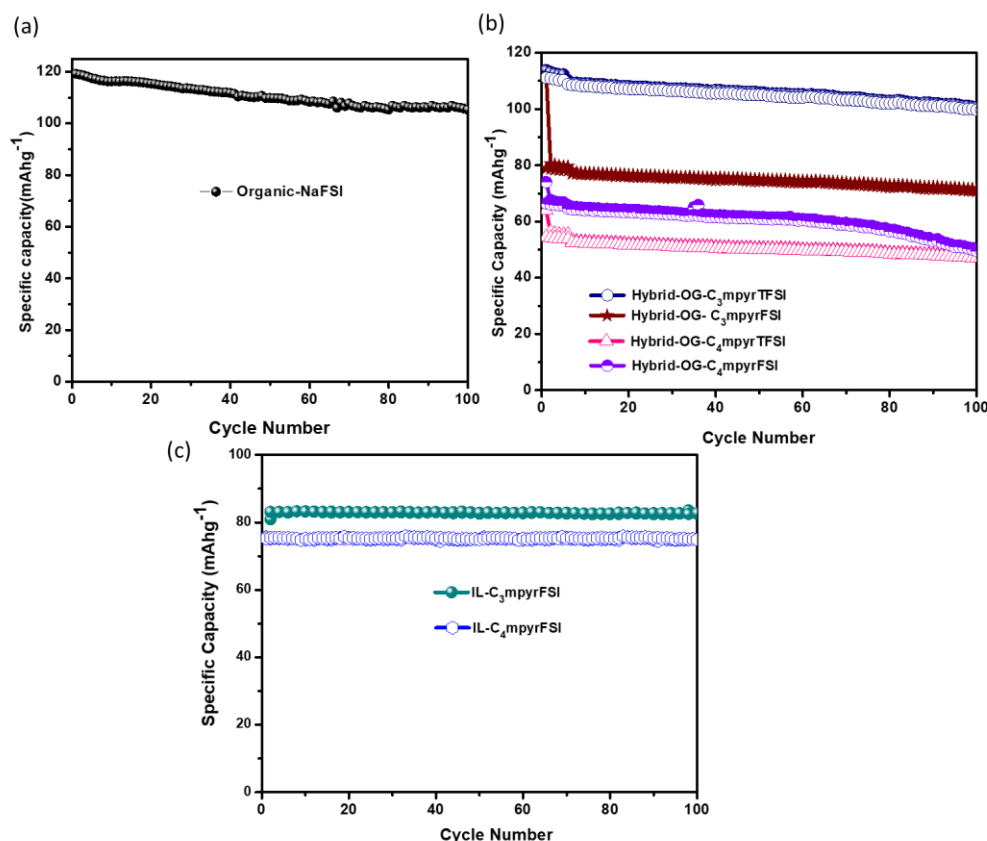


Figure 6. 3: Charge-discharge cycling performance of NVP@C /electrolyte/Na-foil cell using (a) organic, (b) hybrid and (c) ionic liquid electrolytes.

Figure 6.3 shows the charge-discharge cycling performance of NVP@C | Na cells with organic, hybrid and ionic liquid electrolytes at a 0.5C current rate over a potential range of 2.5 to 3.8V vs. Na/Na⁺ for 100 cycles. As shown in Figure 6.3a, NVP@C retains 89% of its capacity when charged and discharged in this way with the organic electrolyte. The capacities and capacity retention values obtained with the hybrid electrolytes depended on the ionic liquid used (Figure 6.3b). Hybrid-OG-C₃mpyrTFSI shows a high capacity and 95% capacity retention up to 100 cycles as compared to other Hybrid-OG-C₃mpyrFSI, Hybrid-OG-C₄mpyrTFSI, and Hybrid-OG-C₄mpyrFSI electrolytes. Hybrid-OG-C₃mpyrTFSI electrolyte forms a Na-FSI, Na-TFSI and SO₂F based stable SEI layer on the both NVP@C and sodium metal surfaces as compared to other hybrid compositions, as indicated in the sodium battery literatures^{152, 160}. Pure ionic

liquid electrolytes (IL-C₃mpyrFSI & IL-C₄mpyrFSI) with NVP@C cathode material show 99% capacity retention after 100 cycles, but specific discharge capacity is 80mAhg⁻¹ at a 0.5C rate which is lower than that found with the organic and hybrid electrolytes (Figure 6.3c). This is due to the high charge-transfer resistance which occurs when ionic liquid electrolytes are used in sodium-ion batteries ¹¹⁷

Based on the above electrochemical performance results, we have chosen three electrolytes for further study of the SEI layers that form on both NVP@C and Na metal surfaces in contact with these electrolytes (Organic-NaFSI, Hybrid-OG-C₃mpyrTFSI, and IL-C₃mpyrFSI).

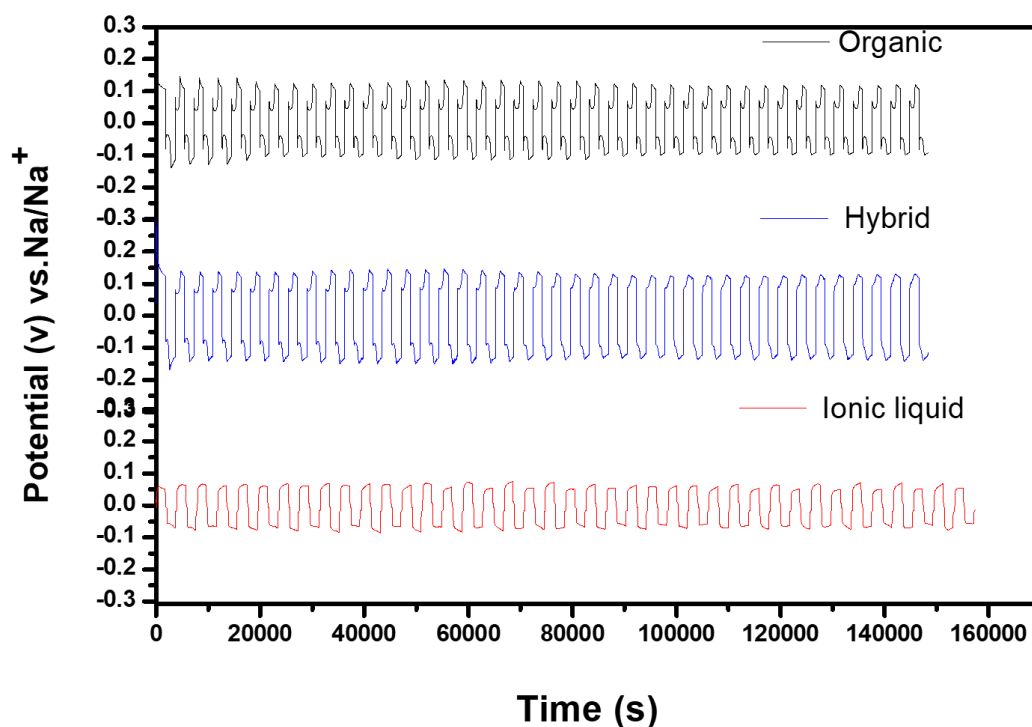


Figure 6. 4: Plating and stripping cycles of Na| Na symmetrical cells with organic, hybrid and ionic liquid electrolytes at 0.1 mAcm⁻².

Na|Na symmetrical cell cycling was performed over 100 cycles at 0.1 mAcm⁻² current density, as shown in Figure 6.4. The initial polarization values for each cell were 150mV, 130mV, and

50mV for organic, hybrid and ionic liquid electrolytes, respectively (Figure 6.5). The organic electrolyte shows tail peaks in these stripping and plating reactions. This is attributed to the deposition, dissolution of the sodium and formation of the surface passivation film on the metal surface^{98, 142}. As indicated by the greater over potentials in each cycle (150mV) the organic electrolyte, the passivation film on sodium metal is more resistive than that formed in either hybrid or ionic liquid electrolytes. Further, the presence of ionic liquid in the hybrid and ionic liquid electrolytes may lead to the formation of smoother, less resistive passivation layers on sodium metal, as has been observed in other metal batteries²¹⁰. The hybrid and ionic liquid electrolytes showed smooth stripping, and plating reaction peaks as compared to the organic electrolyte.

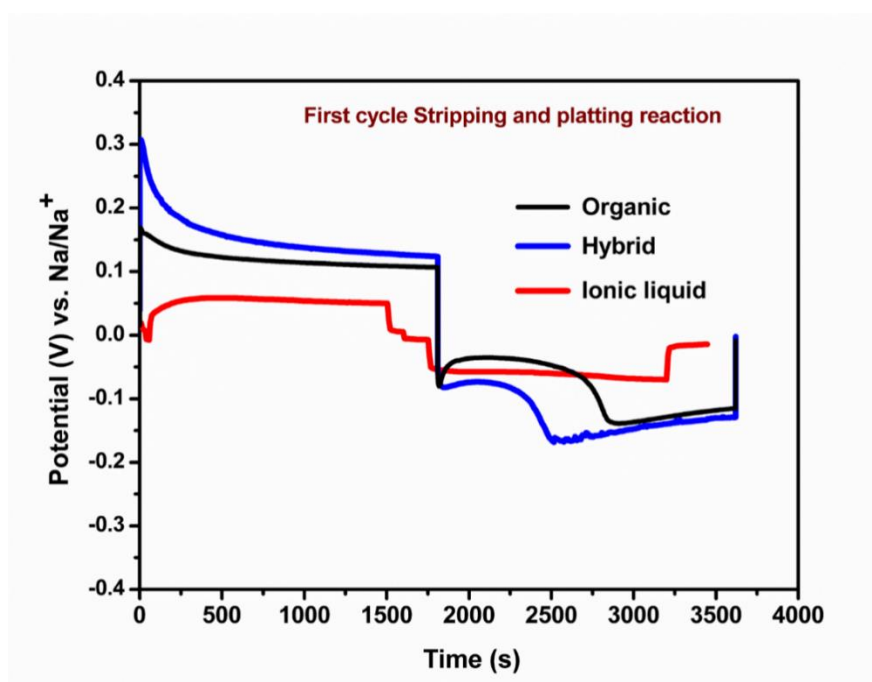


Figure 6. 5: First cycle plating and stripping reaction of Na|Na symmetrical cells with organic, hybrid and ionic liquid electrolytes.

6.3 Characterization of SEI layers on NVP@C and Sodium metal surfaces:

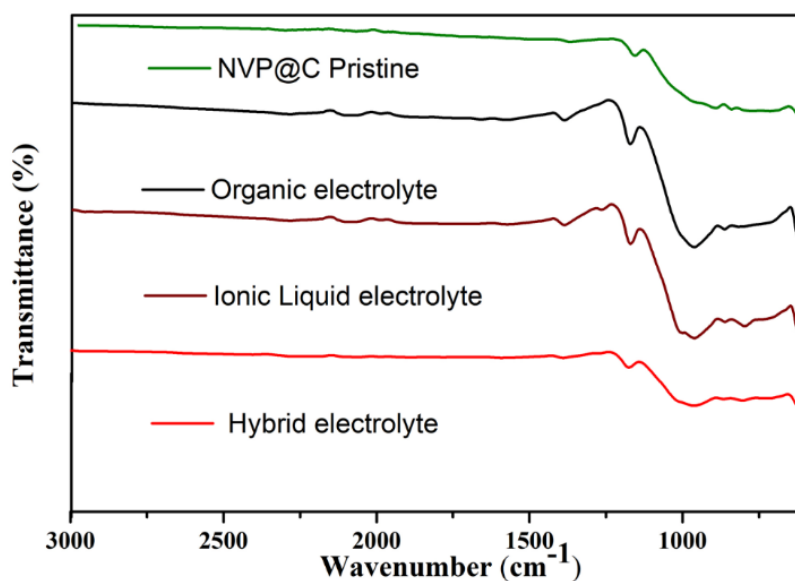


Figure 6. 6: Ex-situ FTIR spectra of NVP@C cathode material: pristine and after 100 cycles with organic, hybrid and ionic liquid electrolytes.

FTIR spectra of the surfaces of NVP@C electrodes cycled with organic, hybrid and ionic liquid electrolytes are showed in Figure 6.6. These spectra show that the SEI layers that formed on the electrodes depend upon the electrolyte used. The most relevant peaks are those for SO_2F , FSI, and SO_2FSI at 1184, 1038 and 1368 cm^{-1} . Organic and ionic liquid electrolytes produced SEI layers, as indicated by spectra that were quite different from that of the pristine NVP@C electrode. In contrast, the spectrum of the surface of the electrode cycled in the hybrid electrolyte is similar to that of the pristine NVP@C electrode.

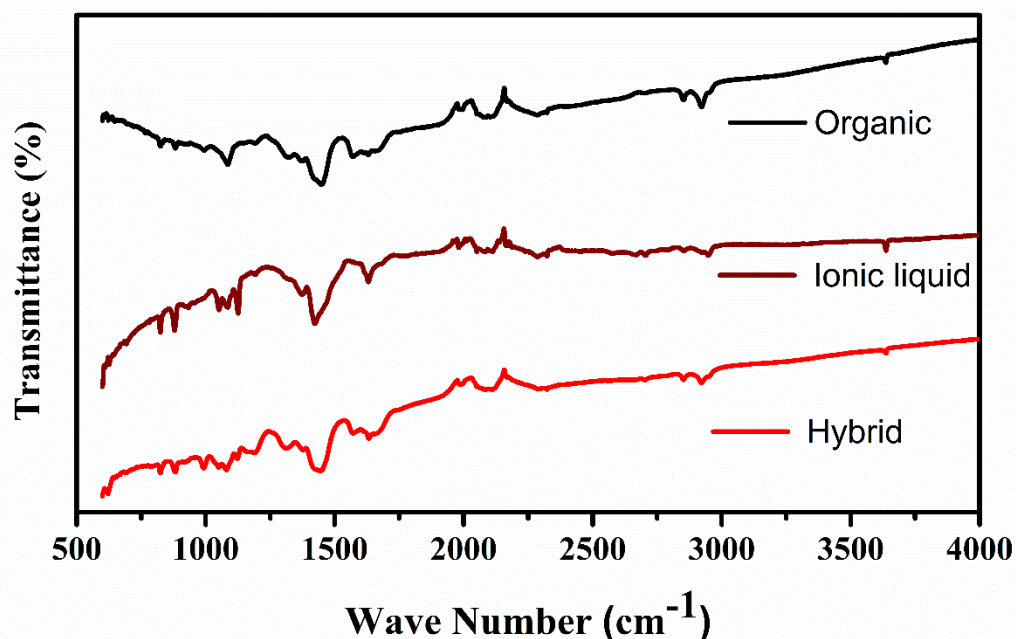


Figure 6. 7:Ex-situ FTIR spectra of sodium metal extracted from Na| Electrolyte |NVP@C cells after 100 cycles with organic, hybrid or ionic liquid electrolytes.

FTIR spectra of sodium metal after cycling with organic, hybrid and ionic liquid electrolytes are showed in Figure 6.7. The FTIR peaks, listed in Table 6.2, show a major component of carbonate, sodium carbonate and alkyl carbonate based SEI layer on sodium metal by the organic electrolyte. There is a significant difference between SEI layer compositions, with additional peaks of ionic liquid related peaks seen in the spectra from the sodium surfaces cycled in hybrid and ionic liquid electrolytes, as listed in Table 6.2.

Table 6. 2 : SEI compositions on sodium metal analyzed by FTIR for organic, hybrid and ionic liquid electrolytes.

SEI compositions on sodium metal by organic electrolyte	
Wavenumber (cm ⁻¹)	Assigned Functional groups
2932	C-H, O-H
2296	N=C=O, N=C=S
2097	N=C=N
2006	C=C=O, C=C
1661	NH ₂ , C=N
1643, 1579	C=O, C=C
1071	NH ₂ , N-H
SEI compositions on sodium metal by Hybrid and Ionic liquid electrolyte	
1443, 1379	S=O, S=O
1125,	C=S
1071	NH ₂ , N-H
889	NH ₂ , N-H
825	S-OR

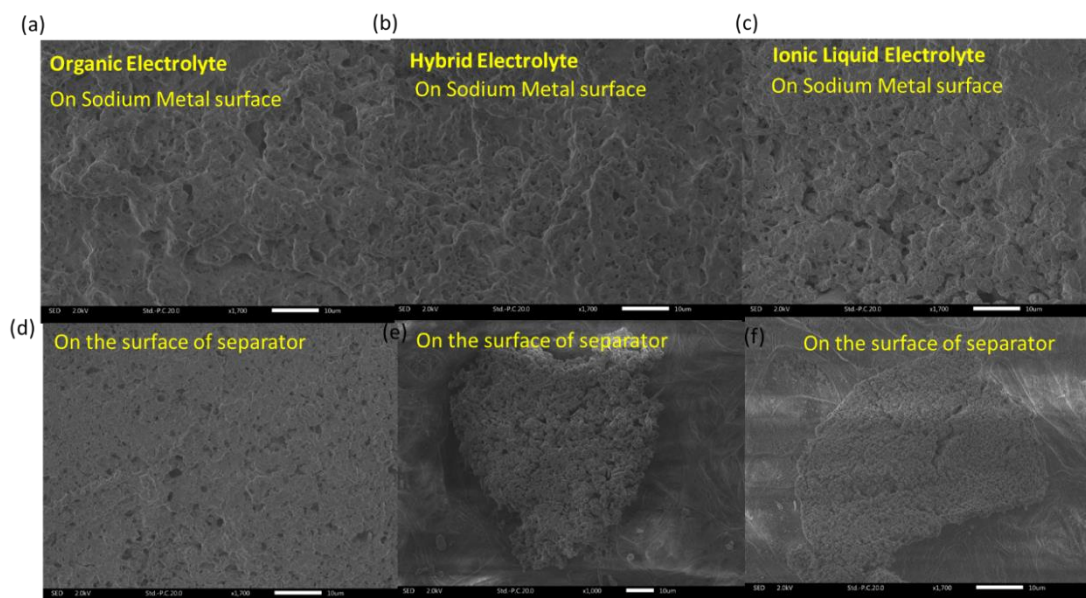


Figure 6. 8: SEM images of Sodium metal and separator after 100 cycles with (a) & (d) organic electrolyte, (b) & (e) hybrid electrolyte and (c) & (f) ionic liquid electrolyte.

The surfaces of Sodium metal electrode cycled with organic, hybrid and ionic liquid electrolytes for 100 cycles at a C/2 rate are shown in Figure 6.8. The organic electrolyte formed

a thick, uneven, SEI layer, containing small pores, on the surface of sodium metal (Figure 6.8a). The hybrid electrolyte formed a more uniform SEI layer, but the layer appeared very porous (Figure 6.8b). The ionic liquid electrolytes formed a more stable SEI layer, compared to those formed with the organic or hybrid electrolytes. As well as being porous and uneven, this layer has some cracks in it (Figure 6.8c), which could be the cause of the high charge transfer resistance seen with this electrolyte^{98, 117}. Here, separator surfaces shown similar morphologies to the corresponding sodium surfaces with organic, hybrid and ionic liquid electrolytes (Figure 6.8d, 6.8e, and 6.8f).

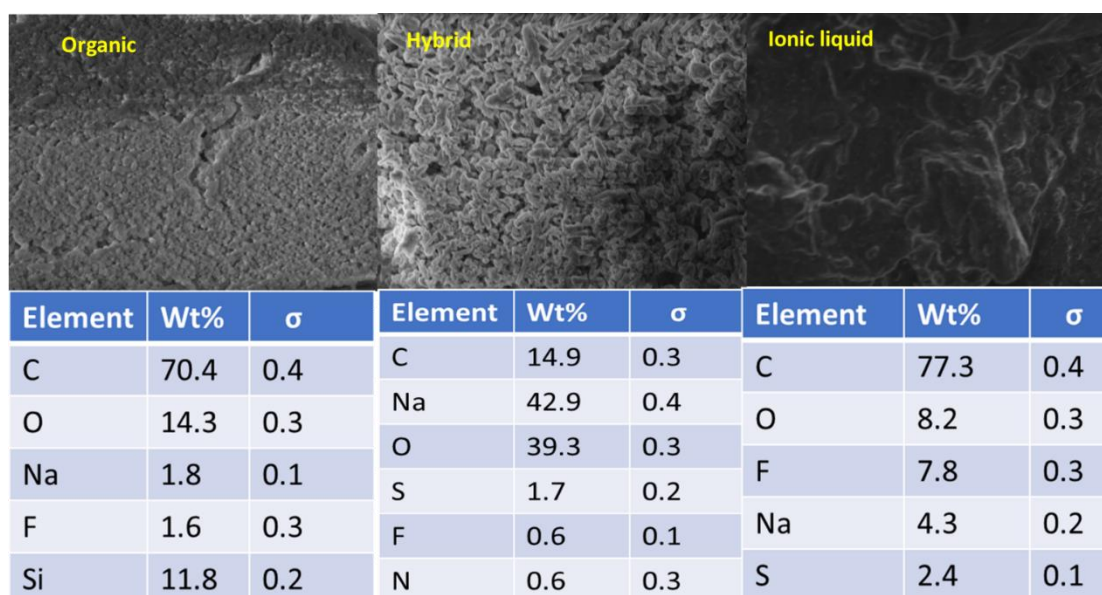


Figure 6. 9: EDX analysis of sodium metal surface with (a) organic, (b) hybrid, and (c) ionic liquid electrolytes.

The FEG-SEM-EDX technique was used to determine the compositions of the surface films formed on sodium metal by different electrolytes, as shown in Figure 6.9. The SEI layer formed on sodium metal in the organic electrolyte (Figure 6.9a) shows the most carbonate and fluorinate, while the SEI layer formed in the hybrid electrolyte shows sulfur, carbonate and fluorinate compounds (Figure 6.9b). The higher concentration of sulfur and fluoride compounds can come from the ionic liquid (Figure 6.9b). In the hybrid electrolyte, the ionic liquid formed a highly stable passivation layer on the surface of the sodium. In the ionic liquid

electrolyte, the SEI layer contains mostly fluorinate and sulfur compounds. This ionic liquid electrolyte formed the more stable passivation layer on the surface of the sodium metal battery as compared to organic electrolyte.

6.4 Summary:

In this work, adding ionic liquids to organic electrolytes increased their thermal stability. The electrolyte thermal decomposition reaction mechanism was examined by TGA-IR. The NVP@C cathode material shows stable and excellent cycling performance with organic, hybrid and ionic liquid electrolytes for 100 cycles at a rate of C/2. Hybrid electrolytes showed higher capacity (115 mAhg^{-1}) than organic or ionic liquid electrolytes. This is probably because hybrid electrolytes formed a uniform and stable SEI layer on the surfaces of NVP@C and sodium metal in the sodium metal battery. The SEI morphologies and compositions were analyzed by FEG-SEM, FTIR and EDX techniques. The hybrid electrolyte, a mixture of organic and ionic liquid-based electrolytes, provided increased thermal stability, excellent electrochemical performance, and a stable passivation layer on the surfaces of NVP@C cathode material and sodium metal in sodium metal batteries.

Chapter 7

Low-cost sodium-ion battery using almond-shell based hard carbon anode and NVP@C cathode

7.1 Introduction

Development of low cost and high-performance electrode materials is required for commercialization of sodium-ion batteries. In this context, carbonaceous materials stand out as a low cost and sustainable negative electrodes in energy storage devices.²¹¹ Graphite is a well-established carbon based electrode material for lithium batteries.²¹² Unfortunately, graphite shows poor electrochemical performance with Na⁺, probably due to its larger ionic radius than Li⁺. Problems include poor sodium insertion and more solid electrolyte interface products with organic electrolytes.²¹³ However, expanded graphite (otherwise known as reduced graphene oxide) displays significantly better sodium-insertion performance,^{214, 215} though it shows poor performance with alkyl carbonate-based organic electrolytes.⁵⁹ Hard carbon-based anode materials are promising because they display high capacity, low working potentials with sodium, and excellent long-term cycling stability.²⁰⁴

Hard carbons (HC) are prepared through calcination of carbon sources such as sucrose, glucose, poly vinyl chloride or biomass materials,^{18, 216, 217} and are extensively investigated because their precursors are abundant, cheap and easy to access when compared to other carbonaceous precursors.²¹⁸ Most biomass-derived hard carbons are prepared by a simple pyrolysis process from a vast range of sources such as banana peel,²¹⁹ peanut shell,²²⁰ apple waste,²²¹ corn cobs,¹⁹ sorghum stalk waste,²²² macadamia shell²²³, kelp²²⁴ and orange skin²²⁵. Recently, Dow et al. stated that a hard carbon prepared from a lignin-rich source (Peanut shell) showed superior cycling performance with sodium, in contrast to the performance of hard carbons prepared from pectin-rich

(apple waste) and hemicellulose-rich (corn cob) sources.²²⁶ Almond-shell waste is another example of a lignin-rich biomass. In particular, a relatively pure form of lignin that can be obtained after a bio-refinery process has extracted the valuable products from the almond shell.¹²⁵ Hard carbons derived from this type of pure lignin source have not yet been explored as anodes for sodium-ion batteries.

In this work, we report the synthesis, morphology, electrochemical and structural characterization of hard carbon anodes derived from almond-shell-waste lignin. The electrochemical performance of hard carbon electrode was evaluated with an ionic liquid-based electrolyte for 1000 cycles at a 1C rate in a HC |Electrolyte| Na-metal half-cell. The full-cell sodium-ion battery cycling performance was also investigated by assembling batteries containing the new hard carbon as anode material and a previously reported^{47, 152} NVP@C as cathode material (synthesized here by a new and more facile method), and testing for 350 cycles. Ionic liquid electrolyte (IL) based full cell results outperformed the standard organic electrolyte at room temperature and showed better cycling performance. The superior stability of the cells in the IL-based electrolyte in conjunction with its non- flammability results in a more reliable and higher safety sodium ion battery. The low cost and high-performance hard carbon material from the almond shell therefore appears promising for the development of high energy density, high rate capability, and eco-friendly sodium-ion batteries.

7.2 Characterization of Bioderived Hard carbon and NVP@C materials:

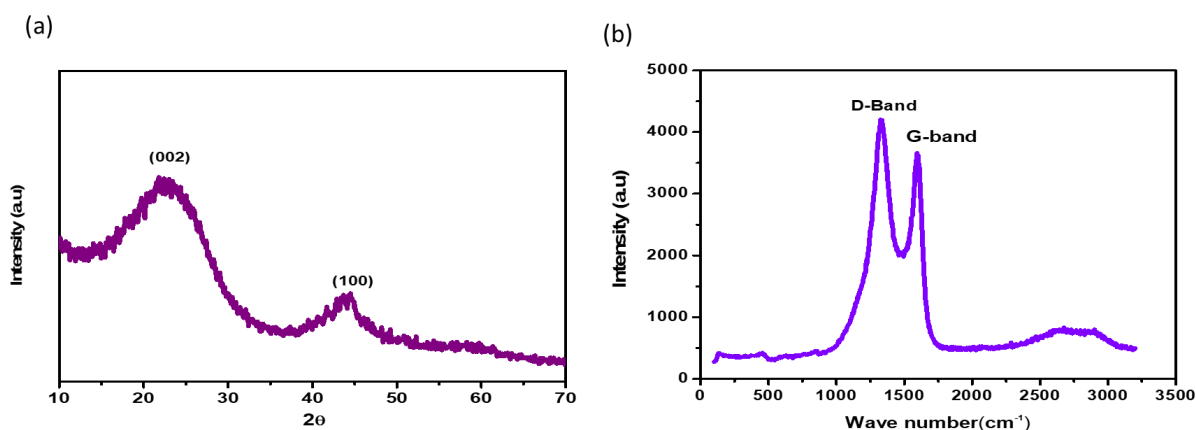


Figure 7. 1: Characterization of bio-derived hard carbon: (a) Powder XRD pattern and (b) Raman spectrum.

Figure 7.1a shows the XRD pattern of almond-derived hard carbon anode material, with two broad peaks at 23° and 44° , corresponding to the (002) diffraction of the graphitic layer structures and the (101) diffraction of graphite, respectively. The diffraction pattern of the as prepared bio-derived hard carbon is in good agreement with previous reports¹²⁰. Moreover, the Raman spectrum exhibits two broad bands: the defect-induced band at 1335 cm^{-1} (D-band) and crystalline graphite band at 1587 cm^{-1} (G-band) (Figure 7.1b)¹⁴

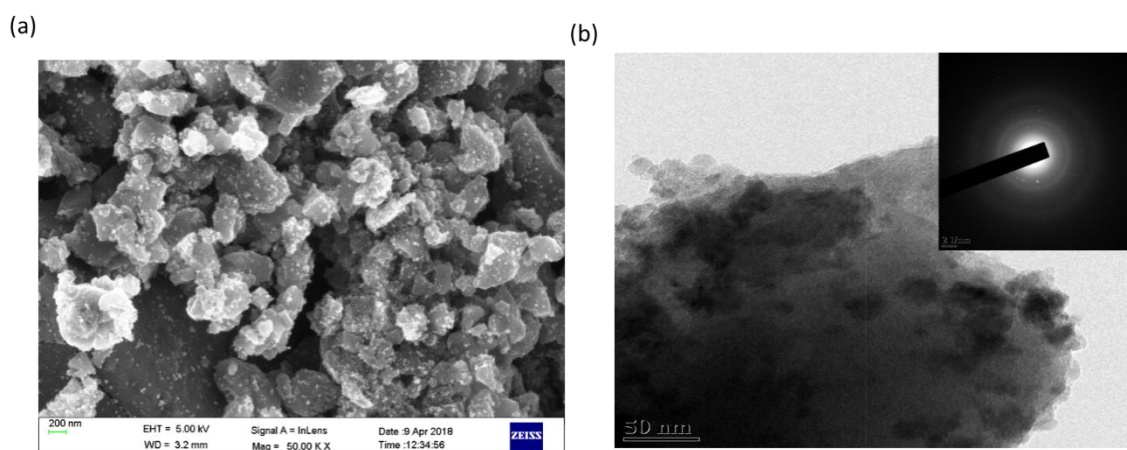


Figure 7. 2: Bio-derived hard carbon anode material morphology and structural information: (a) SEM, and (b) TEM images.

The morphology of the hard carbon derived from almond shell is displayed in Figure 7.2. The SEM image of hard carbon material shows agglomeration of particles with broad particle-size distribution from 100nm to 400nm (Figure 7.2a). The HR-TEM image confirms the amorphous

structure of this new hard carbon, which is consistent with previous studies on other hard carbons derived from different carbonaceous precursors(Figure 7.2b)^{18, 218}.

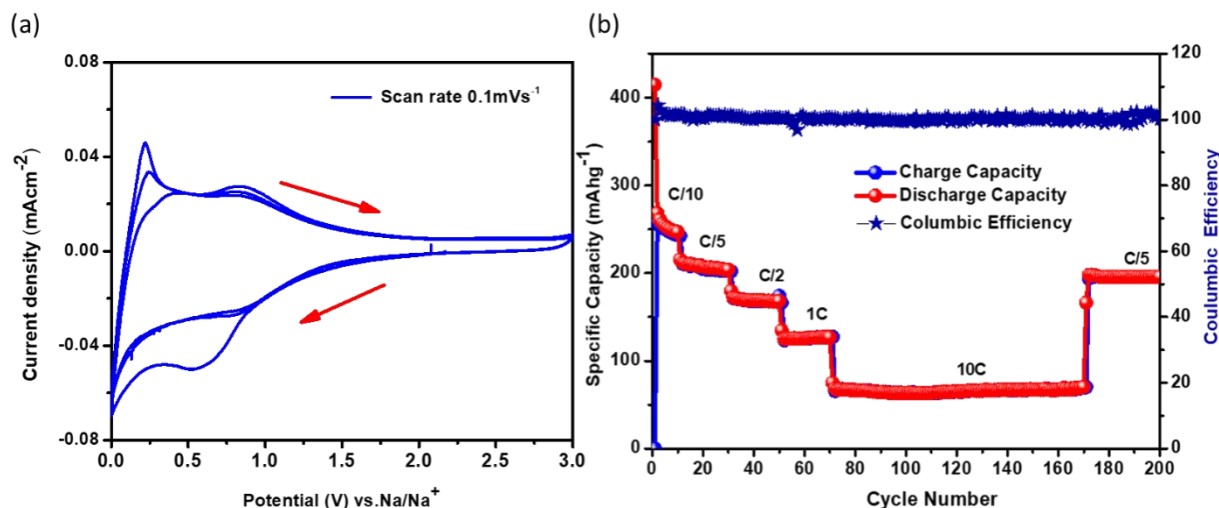


Figure 7. 3:Electrochemical performance of bio derived hard carbon with ionic liquid electrolyte (a) Cyclic voltammetry performed at a scan rate of 0.1 mVs⁻¹, (b) The charge-discharge cycling performance of hard carbon at different current rates in the potential range of 0.01 to 2V vs Na/Na⁺.

Figure 7.3 shows the electrochemical measurements for the HC/IL/Na using the ionic liquid-based electrolyte. The cyclic voltammetry of almond shell-derived hard carbon was performed at 0.1 mVs⁻¹ scan rate in the potential interval of 0.01 to 3 V vs. Na/Na⁺ (Figure 7.3a). The bio derived hard carbon anode material shows peaks at 0.5 V and 0.01 V vs. Na/Na⁺, which are related to the insertion and adsorption mechanism of sodium in the host carbon, respectively.^{14, 121121} This electrode material was then subjected to charge-discharge cycling at different rates and showed discharge capacity values of 258, 220, 180, 150 and 50 mAhg⁻¹ at C/10, C/5, C/2, 1C, and 10C rates, respectively (Figure 7.3b). The material showed excellent rate capability and good capacity retention of 99% with the ionic liquid-based electrolyte as compared to other

reported works in the literature for sodium ion battery.^{19, 218, 224, 226}

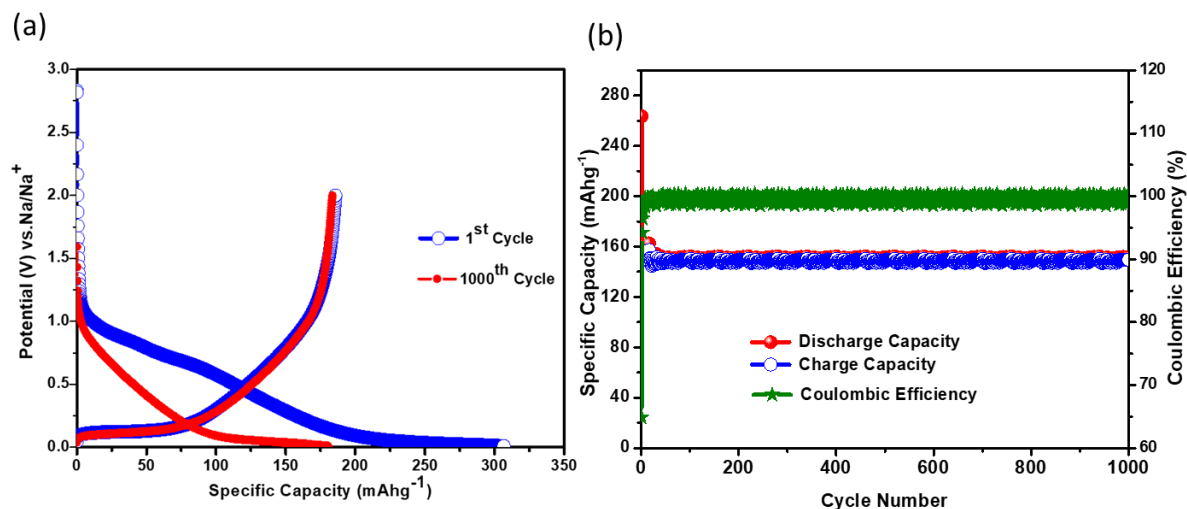


Figure 7. 4:(a) Potential versus Capacity plot of hard carbon anode material for first and 1000th cycles, (b) Charge-discharge cycling performance of hard carbon for 1000 cycles at 1C rate in the potential range of 0.01 to 2V vs Na/Na⁺.

Figure 7.4a and 7.4b show the charge-discharge cycling performance of almond-shell derived hard carbon with sodium metal at 1C rate for 1000 cycles in the potential range of 0.01 to 2 V vs. Na/Na⁺. The potential versus capacity plot shows that the first charge capacity value is lower than the first discharge capacity value, this is likely due to the formation of a solid electrolyte interface (SEI) on the surface of the carbon material (Figure 7.4a).^{16, 18 20} During the subsequent cycles, the capacity values are stabilized and remained stable around 150mAhg⁻¹ for up to 1000 cycles with 99% coulombic efficiency (Figure 7.4b).

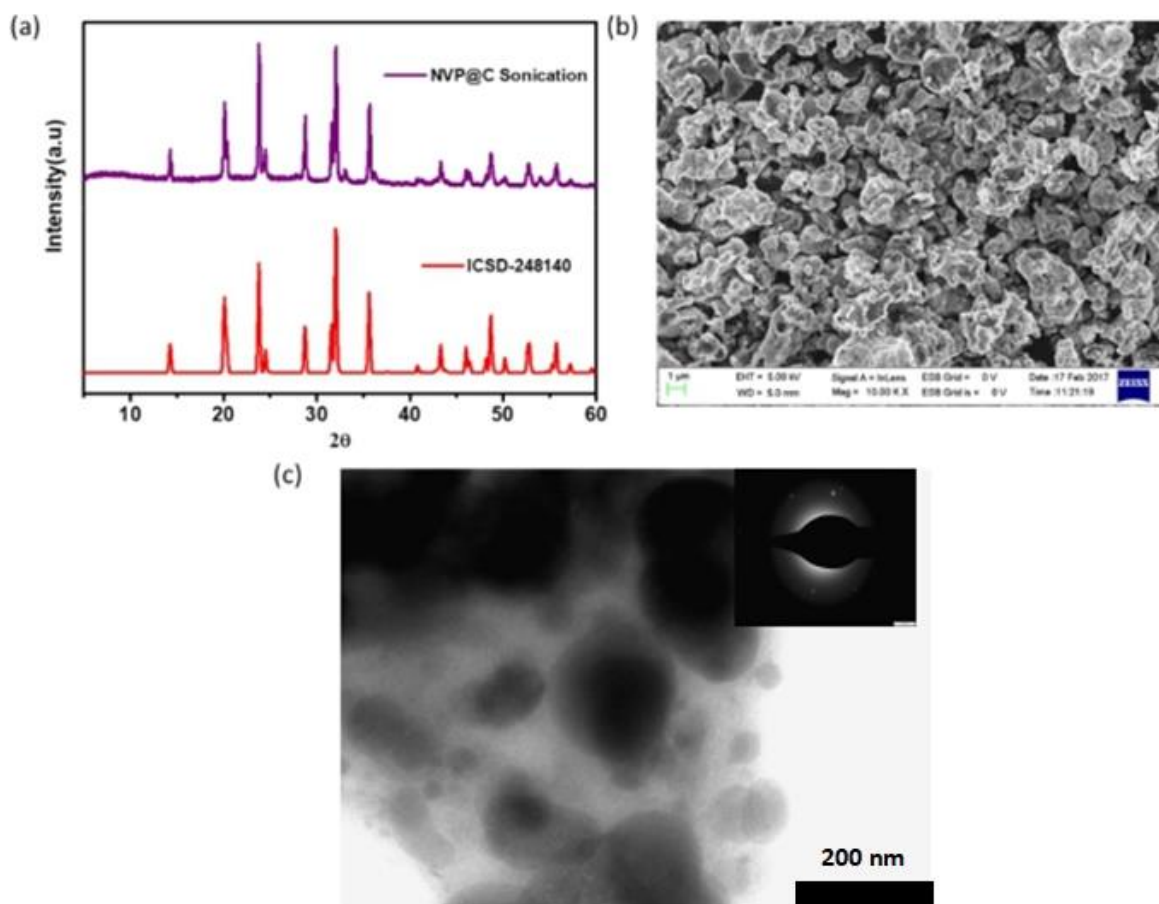


Figure 7. 5:: NVP@C cathode material structural and morphology analysis by: (a) XRD, (b) SEM, and (c) TEM.

Figure 7.5a shows the XRD pattern of the as-prepared NVP@C material by simple sonication method. The diffraction pattern matches well with the NASICON-framework NVP with $R\bar{3}C$ space group (ICSDS data card no-248410), which is in good agreement with previous reports¹⁶⁷. In figure 7.5b the SEM image of the as-prepared NVP@C powder is displayed, the cathode material shows micron-sized particles while the TEM image in Figure 7.5c shows that the NVP@C particles are fully covered with amorphous carbon

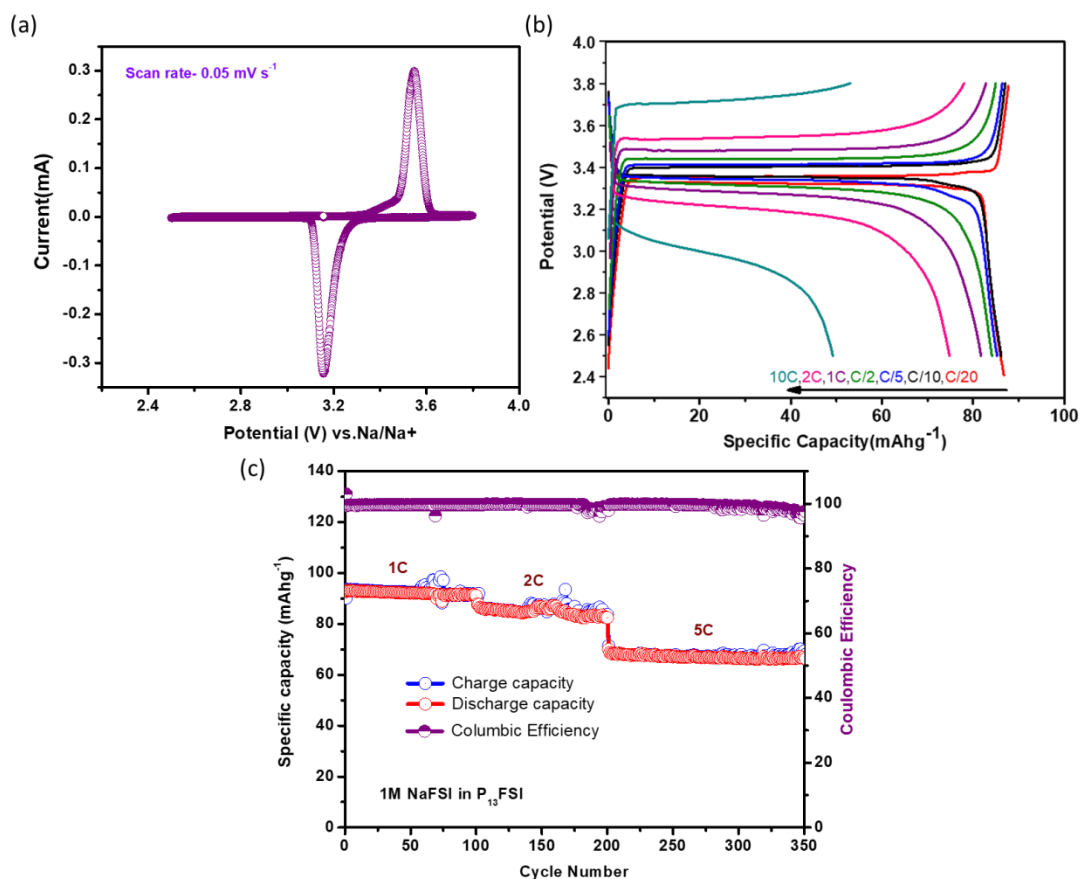


Figure 7. 6: Electrochemical characterization of NVP@C cathode material with ionic liquid electrolyte (a) Cyclic voltammetry performed at a scan rate of 0.05 mVs⁻¹, (b) Potential vs. Specific capacity curves obtained at different current density rates for NVP@C/IL/ Na cell, and (c) Charge-discharge cycling performance at different current density rates (1C, 2C and 5C) for 350 cycles.

The cyclic voltammetry of NVP@C cathode material in 1M NaFSI/C₃mpyrFSI electrolyte showed reversible oxidation and reduction of V³⁺/V⁴⁺ at 3.53 V (oxidation) and 3.21 V (reduction) vs. Na/Na⁺ at a scan rate of 0.05 mVs⁻¹ (Figure 7.6a). Figure 7.6b shows the charge-discharge profiles, obtained at different rates in a NVP@C |IL electrolyte| Na half-cell configuration. The discharge capacity values were 92, 88, 85, 83, 81, 78 and 50 mAhg⁻¹ at C/20, C/10, C/5, C/2, 1C, 2C, and 10C, respectively. The cell capacity values are smaller than expected, this is mainly ascribed to high values of charge-transfer resistance between the ionic liquid electrolyte and sodium metal (IL| Na metal) in half-cell (Cathode |IL |Na metal) configurations with some of the cathode

materials during charge-discharge cycling performance in sodium battery at room temperature¹¹⁷. The NVP@C |IL|Na foil-cell system was subjected to extend cycling for a total of 350 cycles: at rates of 1C (for 100 cycles), 2C (for 100 cycles), and 5C (for 150 cycles). This material displayed excellent reversibility and consistent capacity values, with an impressive 99% coulombic efficiency, even after 350 cycles (Figure 7.6c).

7.3 Electrochemical characterization of NVP@C|IL|HC full cell sodium ion battery:

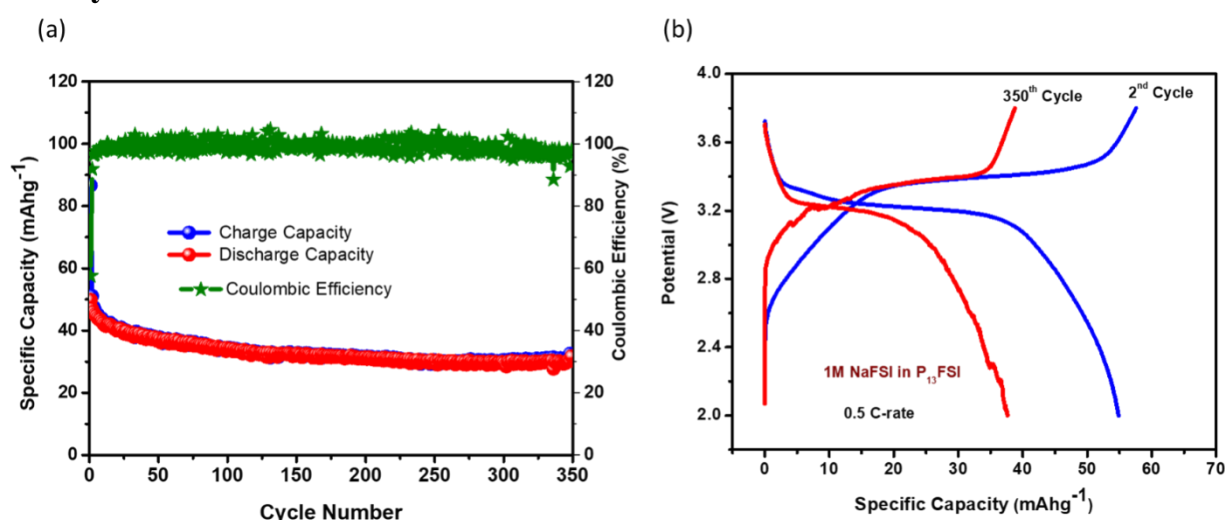


Figure 7. 7: Electrochemical characterization of NVP@C|IL|HC cell (a) Charge-discharge cycling performance at the 0.5C rate for 350 cycles, and (b) Potential vs. specific capacity curves at second and 350th cycles, at the 0.5C-rate.

To assemble the full cell sodium-ion battery, the as-prepared hard carbon was used as anode and NVP@C was applied as cathode material. These electrodes are balanced against each with areal capacities before cycling performance of the full cell sodium ion battery. Figure 7.7a shows the charge-discharge cycling performance and coulombic efficiency of the full Na-ion cell (HC|1M NaFSI / C₃mpyrFSI|NVP@C), cycled at a rate of C/2. The cell shows a capacity retention value of 96% (from 20th cycle to 350th cycle), and a coulombic efficiency of 99% up to 350 cycles. The discharge capacity values

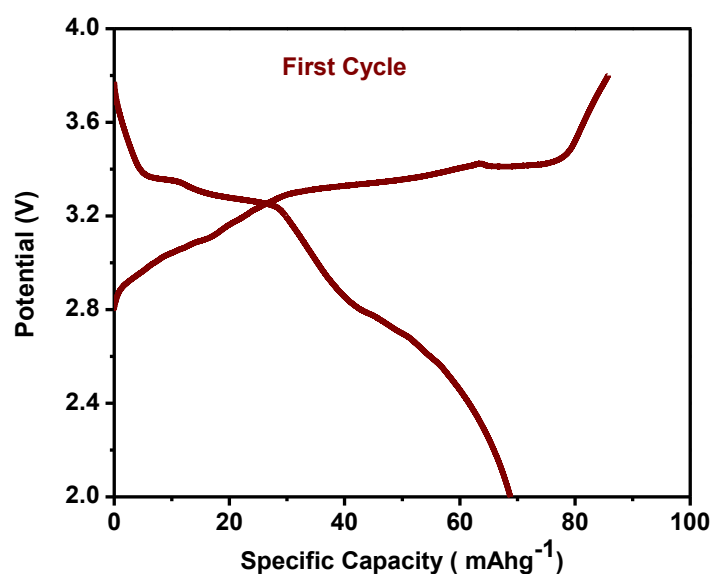


Figure 7. 8: Potential vs Specific capacity curve for (HC|1M NaFSI in C3mpyrFSI|NVP@C) cell at first cycle with 0.5 C current rate.

(Based on the active material of both electrodes) are 55mAh.g⁻¹ and 39mAh.g⁻¹ at the 2nd and at the 350th cycle, respectively. The potential versus capacity plot shows a small polarization effect as the cycle number increased (Figure 7.7), this effect is possibly due to the greater SEI layer formation and the irreversible sodium insertion during the first cycles on the hard carbon electrode (Figure 7.8). This behaviour has also been observed in other full cell sodium ion batteries.^{135, 190, 203, 221}

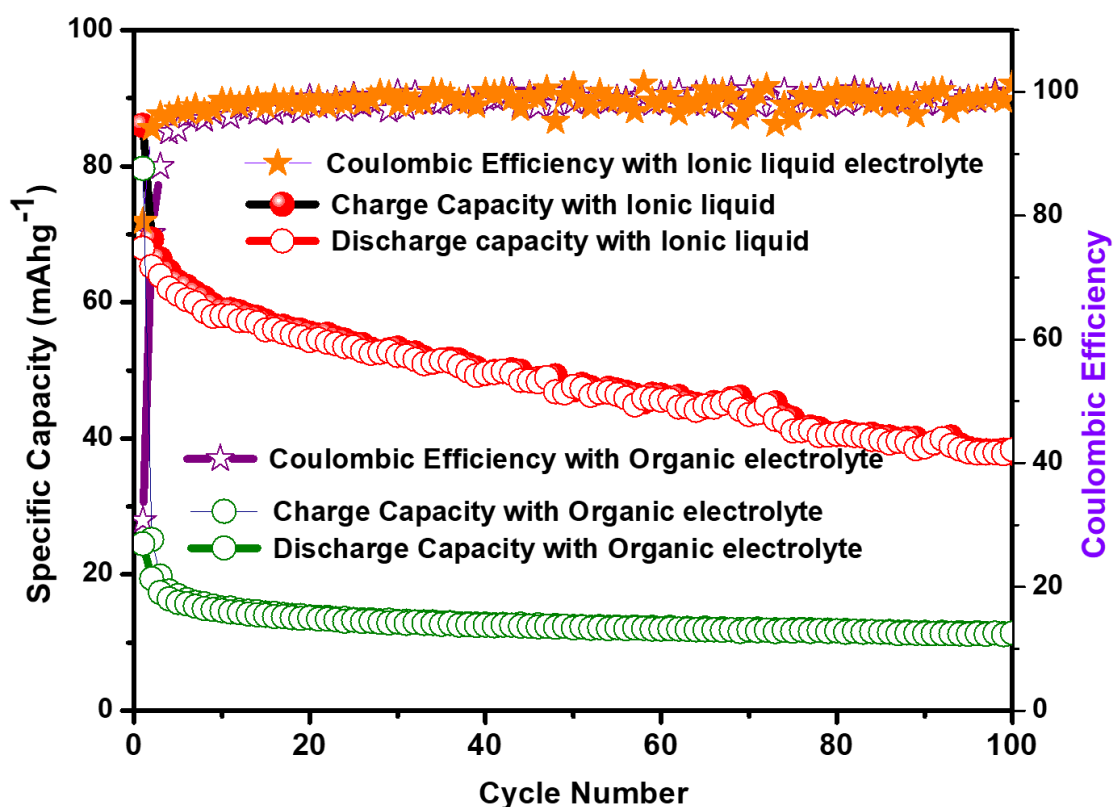


Figure 7. 9: Cycling performance of (HC|1M NaFSI in C3mpyrFSI|NVP@C) cell with organic and ionic liquid electrolyte for 100 cycles at 0.5C rate.

In order to assess the reliability of the ionic liquid-based electrolyte used in this work, we also compared the performance of our full cells by assembling cells with traditional carbonate-based electrolytes (1M NaClO₄ in EC :PC (1:1)v/v + 5wt% FEC. As shown in Figure 7.9 (cycling at 0.5C-rate for 100 cycles), the IL-based electrolyte shows a superior performance at room temperature when compared to the organic one. Moreover, the IL-based electrolyte is non-flammable, this feature reinforces the superiority of the sodium ion battery presented here, leading to a safe energy storage device.

Both bio-derived hard carbon anode material and a simple sonication-derived NVP@C cathode material showed an excellent electrochemical performance with the ionic liquid-based electrolyte, ensuring a cost-effective full cell sodium-ion battery

which can be used in practical energy-storage applications, including large-scale grid storages.

7.4 Summary:

Almond shell-bio-derived hard carbon material was successfully synthesized and applied as an anode material for sodium-ion batteries. This anode material showed a stable reversible capacity of 150mAhg^{-1} for 1000 cycles and retained 99% of capacity at 1C-rate by using a non-flammable ionic liquid-based electrolyte. As a cathode material to further assemble a full sodium-ion battery, NVP@C was synthesized by a facile and straight forward sonication method. In a half cell configuration, the NVP@C cathode material exhibited a stable and reliable electrochemical performance, with capacity values of 90mAhg^{-1} , 85mAhg^{-1} , and 70mAhg^{-1} for 1C, 2C and 5C rates, respectively. The full cell NVP@C |IL| bio-derived-HC displayed a good reversible capacity value of 39mAhg^{-1} for 350th cycle at C/2 rate with the ionic liquid-based electrolyte. Almond-shell based bio-derived hard carbon anode material may enable a commercial low-cost sodium-ion battery for practical applications.

Chapter 8

Concluding remarks and Future scope

8.1 Concluding Remarks:

Sodium source is available in abundance, and cost-effective with alternative sustainable material as compared to lithium. Sodium ion batteries are required low-cost electrode materials and high thermal stable electrolytes for large-scale energy storage applications. a lot of Na source cathode material studies are being done in sodium ion battery literatures; For our electrolyte optimization studies, we have chosen a NASICON type sodium vanadium phosphate cathode material because it has a high potential plateau (3.4 V), high rate cycling performance with good rate capability to act as a both anode and cathode material based on their operating potential window versus sodium in sodium ion batteries.

To further research on the highly safer electrolytes, we have chosen ionic liquid as the main solvent in sodium electrolytes. Firstly this ionic liquid is introduced as an additive to the conventional electrolyte and the optimization studies are being conducted, by varying the concentration of IL content from 0-12%. These additive optimization studies are performed with the NVP/C cathode Material based on cathode material cycling performance.

The results show that 5 wt% of IL additive electrolyte is one of the best of all the compositions in the conventional electrolyte. To further validate our findings SEI characterization studies are performed by post mortem analysis of HR-TEM, Raman, SEM, EDX, XPS analysis and in-situ impedance are conducted on the surface of NVP@C electrodes in sodium ion battery. SEI characterization studies are also supported that 5wt% IL electrolyte forms a stable passivation layer as compared to the conventional electrolyte (without IL). The objective is to achieve the excellent cycling performance and the high thermal stability of electrolyte, due to the smaller concentration of 5 wt% IL no significant thermal stability changes observed in additive electrolytes. Hence, we needed to conduct a more studies towards to optimize the composition

which could get higher thermal stability electrolytes and cycling performance for sodium ion batteries.

Further studies towards to achieve the high thermal stability electrolyte and excellent cycling performance of sodium ion batteries. We introduced a hybrid electrolyte as electrolytes for sodium ion batteries. Hybrid electrolyte is a mixture of organic solvents ((EC-PC) 1:1 v/v ratio) and ionic liquid with dissolved of 1 molar NaFSI salt. Hybrid electrolyte optimization studies are performed based on physical and electrochemical characterization in sodium ion batteries. Our results showed that Hybrid-2 (50volume% of IL) electrolyte composition is the best composition with NVP@C material in sodium ion batteries. Hybrid electrolytes showed a good thermal stability as compared to the conventional electrolyte. However, Hybrid electrolytes have not surpassed the thermal stability capability with pure ionic liquid electrolytes.

Further our thesis work is focused on pure ionic liquid electrolyte for sodium ion battery. However, pure ionic liquid has underlying issue of high charge transfer resistance with Na metal at room temperature. This has been addressed in many sodium -ion battery literatures. To overcome such issues, we have replaced the Na metal with commercial hard carbon as anode in sodium ion battery. Our full cell results showed that excellent cycling performance with good rate capability as compared to the conventional electrolyte at room temperature. From our studies, we concluded that pure ionic liquid electrolyte to be the suitable one to achieve the highly safe sodium ion battery in the large -scale energy storage applications.

Thermal decomposition studies are being performed to analysis the decomposition reactions and traces of electrolytes for all organic, hybrid and pure ionic liquid electrolytes. SEI layer composition studies on NVP@C material & hard carbon is evaluated, to further validate we extended our SEI characterization studies on Na metal surface by FTIR, SEM, EDX studies. From our results, we found that pure ionic liquid electrolyte formed a thick and rough

passivation film on the surface of Na metal as compared to other conventional and hybrid electrolyte. This result is in good agreement with sodium ion battery literature.

After obtaining the suitable electrolyte and electrodes for sodium -ion battery. We focused on cost optimization of sodium ion battery for commercialization solutions. As a part of it, we pursued the bio waste materials derived the hard carbon from the almond shell. Finally, a full cell is built by using the bio derived hard carbon as anode, NVP@C as cathode along with pure ionic liquid electrolyte. These results are found to be impressive and outperformed the other sodium systems. Our full cell system is not having the high cost additives in electrolytes such as FEC, PS, and VC and showed the low cost with good cycling performance as compared to other sodium electrolytes. Our proto type could be considered as highly safe sodium ion battery for commercialization direction in the future.

8.2 Future scope:

Following on from this investigation into hybrid and IL-based electrolytes with NVP@C and hard carbon electrodes in sodium ion batteries, suggested future work includes:

- More additives studies need to pursue for high energy density full cell sodium ion batteries with an ionic liquid and hybrid electrolytes for stabilization of the cycling performances.
- Investigation of a gel polymer electrolyte to enhance the energy density of sodium metal batteries with NVP@C cathode material.

Attempting to prepare a hard carbon that also contains sodium, to decrease the irreversible loss in the initial cycle of a sodium ion battery.

References:

1. B. Dunn, H. Kamath and J.-M. Tarascon, *Science*, 2011, **334**, 928-935.
2. J. Tarascon and M. Armand, in *Materials For Sustainable Energy: A Collection of Peer-Reviewed Research and Review Articles from Nature Publishing Group*, 2011, pp. 171-179.
3. J.-Y. Hwang, S.-T. Myung and Y.-K. Sun, *Chem.Soc.Rev.*, 2017.
4. Z. Yang, J. Zhang, M. C. Kintner-Meyer, X. Lu, D. Choi, J. P. Lemmon and J. Liu, *Chemical reviews*, 2011, **111**, 3577-3613.
5. I. Hadjipaschalis, A. Poullikkas and V. Efthimiou, *Renewable and sustainable energy reviews*, 2009, **13**, 1513-1522.
6. L. P. Wang, L. Yu, X. Wang, M. Srinivasan and Z. J. Xu, *Journal of Materials Chemistry A*, 2015, **3**, 9353-9378.
7. C.-Y. Yu, J.-S. Park, H.-G. Jung, K.-Y. Chung, D. Aurbach, Y.-K. Sun and S.-T. Myung, *Energy & Environmental Science*, 2015, **8**, 2019-2026.
8. M. Dahbi, N. Yabuuchi, K. Kubota, K. Tokiwa and S. Komaba, *PCCP*, 2014, **16**, 15007-15028.
9. D. W. Han, J. H. Ku, R. H. Kim, D. J. Yun, S. S. Lee and S. G. Doo, *ChemSusChem*, 2014, **7**, 1870-1875.
10. C. Glynn and C. O'Dwyer, *Advanced Materials Interfaces*, 2017, **4**.
11. H. Pan, Y.-S. Hu and L. Chen, *Energy & Environmental Science*, 2013, **6**, 2338-2360.
12. Y. You and A. Manthiram, *Advanced Energy Materials*, 2018, **8**, 1701785.
13. J. W. Choi and D. Aurbach, *Nature Reviews Materials*, 2016, **1**, 16013.
14. D. Stevens and J. Dahn, *J. Electro.Chem. Soc.*, 2000, **147**, 1271-1273.
15. M. M. Doeff, Y. Ma, S. J. Visco and L. C. De Jonghe, *Journal of The Electrochemical Society*, 1993, **140**, L169-L170.
16. S. Komaba, W. Murata, T. Ishikawa, N. Yabuuchi, T. Ozeki, T. Nakayama, A. Ogata, K. Gotoh and K. Fujiwara, *Adv.Funct. Mater.*, 2011, **21**, 3859-3867.
17. J. Deng, M. Li and Y. Wang, *Green Chemistry*, 2016, **18**, 4824-4854.
18. K.-l. Hong, L. Qie, R. Zeng, Z.-q. Yi, W. Zhang, D. Wang, W. Yin, C. Wu, Q.-j. Fan and W.-x. Zhang, *J.Mater.Chem.A*, 2014, **2**, 12733-12738.
19. Q. Jiang, Z. Zhang, S. Yin, Z. Guo, S. Wang and C. Feng, *Appl. Surf. Sci.*, 2016, **379**, 73-82.
20. T. C. Mendes, F. Zhou, A. J. Barlow, M. Forsyth, P. C. Howlett and D. R. MacFarlane, *Sustainable Energy & Fuels*, 2018.
21. H. Zhang, I. Hasa and S. Passerini, *Advanced Energy Materials*, 2018, 1702582.
22. Y. Xu, Y. Zhu, Y. Liu and C. Wang, *Advanced Energy Materials*, 2013, **3**, 128-133.
23. V. Chevrier and G. Ceder, *Journal of The Electrochemical Society*, 2011, **158**, A1011-A1014.
24. L. D. Ellis, T. D. Hatchard and M. N. Obrovac, *Journal of the Electrochemical Society*, 2012, **159**, A1801-A1805.
25. L. Baggetto, P. Ganesh, R. P. Meisner, R. R. Unocic, J.-C. Jumas, C. A. Bridges and G. M. Veith, *J. Power Sources*, 2013, **234**, 48-59.
26. P. R. Abel, M. G. Fields, A. Heller and C. B. Mullins, *ACS applied materials & interfaces*, 2014, **6**, 15860-15867.
27. B. Farbod, K. Cui, W. P. Kalisvaart, M. Kupsta, B. Zahiri, A. Kohandehghan, E. M. Lotfabad, Z. Li, E. J. Lubber and D. Mitlin, *ACS nano*, 2014, **8**, 4415-4429.
28. H. Xie, W. P. Kalisvaart, B. C. Olsen, E. J. Lubber, D. Mitlin and J. M. Buriak, *Journal of Materials Chemistry A*, 2017, **5**, 9661-9670.
29. Y. Liu, N. Zhang, L. Jiao and J. Chen, *Advanced Materials*, 2015, **27**, 6702-6707.

30. J. Qian, Y. Chen, L. Wu, Y. Cao, X. Ai and H. Yang, *Chemical Communications*, 2012, **48**, 7070-7072.
31. C. Nithya and S. Gopukumar, *Journal of Materials Chemistry A*, 2014, **2**, 10516-10525.
32. J. Song, Z. Yu, M. L. Gordin, S. Hu, R. Yi, D. Tang, T. Walter, M. Regula, D. Choi and X. Li, *Nano letters*, 2014, **14**, 6329-6335.
33. R. Alcántara, M. Jaraba, P. Lavela and J. Tirado, *Chemistry of Materials*, 2002, **14**, 2847-2848.
34. L. Zhang, H. B. Wu and X. W. D. Lou, *Advanced Energy Materials*, 2014, **4**.
35. M. C. López, P. Lavela, G. F. Ortiz and J. L. Tirado, *Electrochemistry Communications*, 2013, **27**, 152-155.
36. N. Zhang, X. Han, Y. Liu, X. Hu, Q. Zhao and J. Chen, *Advanced Energy Materials*, 2015, **5**.
37. Y. Wang, C. Wang, Y. Wang, H. Liu and Z. Huang, *Journal of Materials Chemistry A*, 2016, **4**, 5428-5435.
38. Z. Liu, T. Lu, T. Song, X.-Y. Yu, X. W. D. Lou and U. Paik, *Energy & Environmental Science*, 2017, **10**, 1576-1580.
39. W. Ren, H. Zhang, C. Guan and C. Cheng, *Advanced Functional Materials*, 2017, **27**.
40. B. Radisavljevic and A. Kis, *Nature materials*, 2013, **12**, 815.
41. P. F. Wang, Y. You, Y. X. Yin and Y. G. Guo, *Advanced Energy Materials*, 2018, **8**, 1701912.
42. Y. Cao, L. Xiao, W. Wang, D. Choi, Z. Nie, J. Yu, L. V. Saraf, Z. Yang and J. Liu, *Advanced Materials*, 2011, **23**, 3155-3160.
43. R. Berthelot, D. Carlier and C. Delmas, *Nature materials*, 2011, **10**, 74.
44. H. Wang, X.-Z. Liao, Y. Yang, X. Yan, Y.-S. He and Z.-F. Ma, *Journal of The Electrochemical Society*, 2016, **163**, A565-A570.
45. L. Mu, S. Xu, Y. Li, Y. S. Hu, H. Li, L. Chen and X. Huang, *Advanced Materials*, 2015, **27**, 6928-6933.
46. P. F. Wang, H. R. Yao, X. Y. Liu, J. N. Zhang, L. Gu, X. Q. Yu, Y. X. Yin and Y. G. Guo, *Advanced Materials*, 2017, **29**.
47. K. Saravanan, C. W. Mason, A. Rudola, K. H. Wong and P. Balaya, *Advanced Energy Materials*, 2013, **3**, 444-450.
48. M. Avdeev, Z. Mohamed, C. D. Ling, J. Lu, M. Tamaru, A. Yamada and P. Barpanda, *Inorganic chemistry*, 2013, **52**, 8685-8693.
49. F. Boucher, J. Gaubicher, M. Cuisinier, D. Guyomard and P. Moreau, *Journal of the American Chemical Society*, 2014, **136**, 9144-9157.
50. S.-M. Oh, S.-T. Myung, J. Hassoun, B. Scrosati and Y.-K. Sun, *Electrochemistry Communications*, 2012, **22**, 149-152.
51. T. Honma, T. Togashi, N. Ito and T. Komatsu, *Journal of the Ceramic Society of Japan*, 2012, **120**, 344-346.
52. P. Barpanda, T. Ye, S.-i. Nishimura, S.-C. Chung, Y. Yamada, M. Okubo, H. Zhou and A. Yamada, *Electrochemistry Communications*, 2012, **24**, 116-119.
53. H. Kim, R. Shakoor, C. Park, S. Y. Lim, J. S. Kim, Y. N. Jo, W. Cho, K. Miyasaka, R. Kahraman and Y. Jung, *Advanced Functional Materials*, 2013, **23**, 1147-1155.
54. B. Zhang, R. Dugas, G. Rousse, P. Rozier, A. M. Abakumov and J.-M. Tarascon, *Nature communications*, 2016, **7**, 10308.
55. S. W. Kim, D. H. Seo, H. Gwon, J. Kim and K. Kang, *Advanced Materials*, 2010, **22**, 5260-5264.
56. I. D. Gocheva, M. Nishijima, T. Doi, S. Okada, J.-i. Yamaki and T. Nishida, *Journal of Power Sources*, 2009, **187**, 247-252.
57. A. Ponrouch, E. Marchante, M. Courty, J.-M. Tarascon and M. R. Palacín, *Energy*

- Environ.Sci.*, 2012, **5**, 8572.
58. A. Ponrouch, D. Monti, A. Boschini, B. Steen, P. Johansson and M. Palacin, *Journal of Materials Chemistry A*, 2015, **3**, 22-42.
 59. H. Che, S. Chen, Y. Xie, H. Wang, K. Amine, X.-Z. Liao and Z.-F. Ma, *Energy Environ.Sci.*, 2017, **10**, 1075-1101.
 60. A. Ponrouch, R. Dedryvère, D. Monti, A. E. Demet, J. M. A. Mba, L. Croguennec, C. Masquelier, P. Johansson and M. R. Palacín, *Energy & Environmental Science*, 2013, **6**, 2361-2369.
 61. G. Kamath, R. W. Cutler, S. A. Deshmukh, M. Shakourian-Fard, R. Parrish, J. Huether, D. P. Butt, H. Xiong and S. K. Sankaranarayanan, *The Journal of Physical Chemistry C*, 2014, **118**, 13406-13416.
 62. M. Goktas, C. Bolli, E. J. Berg, P. Novák, K. Pollok, F. Langenhorst, M. v. Roeder, O. Lenchuk, D. Mollenhauer and P. Adelhelm, *Advanced Energy Materials*, 2018, 1702724.
 63. B. Jache, J. O. Binder, T. Abe and P. Adelhelm, *Phys. Chem. Chem. Phys.*, 2016, **18**, 14299-14316.
 64. H. Kim, J. Hong, Y. U. Park, J. Kim, I. Hwang and K. Kang, *Advanced Functional Materials*, 2015, **25**, 534-541.
 65. B. Zhang, G. Rousse, D. Foix, R. Dugas, D. A. D. Corte and J. M. Tarascon, *Advanced Materials*, 2016, **28**, 9824-9830.
 66. H. Matsumoto, M. Yanagida, K. Tanimoto, M. Nomura, Y. Kitagawa and Y. Miyazaki, *Chem. Lett.*, 2000, **29**, 922-923.
 67. B. Garcia, S. Lavallée, G. Perron, C. Michot and M. Armand, *Electrochim. Acta*, 2004, **49**, 4583-4588.
 68. M. Galiński, A. Lewandowski and I. Stępnia, *Electrochim. Acta*, 2006, **51**, 5567-5580.
 69. A. Lewandowski and A. Świdorska-Mocek, *J. Power Sources*, 2009, **194**, 601-609.
 70. H. Matsumoto, H. Sakaebe and K. Tatsumi, *J. Power Sources*, 2005, **146**, 45-50.
 71. C. Ding, T. Nohira, K. Kuroda, R. Hagiwara, A. Fukunaga, S. Sakai, K. Nitta and S. Inazawa, *J. Power Sources*, 2013, **238**, 296-300.
 72. S. A. Mohd Noor, P. C. Howlett, D. R. MacFarlane and M. Forsyth, *Electrochim. Acta*, 2013, **114**, 766-771.
 73. J. S. Moreno, G. Maresca, S. Panero, B. Scrosati and G. Appetecchi, *Electrochem. Commun.*, 2014, **43**, 1-4.
 74. T. Hosokawa, K. Matsumoto, T. Nohira, R. Hagiwara, A. Fukunaga, S. Sakai and K. Nitta, *The Journal of Physical Chemistry C*, 2016, **120**, 9628-9636.
 75. H. Yoon, H. Zhu, A. Hervault, M. Armand, D. R. MacFarlane and M. Forsyth, *Phys. Chem. Chem. Phys.*, 2014, **16**, 12350-12355.
 76. M. Armand, F. Endres, D. R. MacFarlane, H. Ohno and B. Scrosati, *Nat. Mater.*, 2009, **8**, 621-629.
 77. S. Hashmi, M. Y. Bhat, M. K. Singh, N. K. Sundaram, B. P. Raghupathy and H. Tanaka, *J. Solid State Electrochem.*, 2016, **20**, 2817-2826.
 78. D. Monti, E. Jónsson, M. R. Palacín and P. Johansson, *J. Power Sources*, 2014, **245**, 630-636.
 79. J. G. Huddleston, A. E. Visser, W. M. Reichert, H. D. Willauer, G. A. Broker and R. D. Rogers, *Green Chem.*, 2001, **3**, 156-164.
 80. K. Kreuer, A. Fuchs, M. Ise, M. Spaeth and J. Maier, *Electrochim. Acta*, 1998, **43**, 1281-1288.
 81. P. Bonhôte, A.-P. Dias, N. Papageorgiou, K. Kalyanasundaram and M. Grätzel, *Inorg. Chem.*, 1996, **35**, 1168-1178.
 82. S. Menne, R.-S. Kühnel and A. Balducci, *Electrochim. Acta*, 2013, **90**, 641-648.

83. S. Theivaprakasam, D. R. MacFarlane and S. Mitra, *Electrochim. Acta*, 2015, **180**, 737-745.
84. S. Wilken, S. Xiong, J. Scheers, P. Jacobsson and P. Johansson, *J. Power Sources*, 2015, **275**, 935-942.
85. M. Montanino, M. Moreno, M. Carewska, G. Maresca, E. Simonetti, R. L. Presti, F. Alessandrini and G. Appetecchi, *J. Power Sources*, 2014, **269**, 608-615.
86. T. Vogl, S. Menne and A. Balducci, *Phys. Chem. Chem. Phys.*, 2014, **16**, 25014-25023.
87. D. R. MacFarlane, N. Tachikawa, M. Forsyth, J. M. Pringle, P. C. Howlett, G. D. Elliott, J. H. Davis, M. Watanabe, P. Simon and C. A. Angell, *Energy & Environmental Science*, 2014, **7**, 232-250.
88. W.-J. Li, S.-L. Chou, J.-Z. Wang, H.-K. Liu and S.-X. Dou, *Journal of Materials Chemistry A*, 2016, **4**, 505-511.
89. L. O. Vogt, M. El Kazzi, E. Jämstorp Berg, S. a. Pérez Villar, P. Novák and C. Villevieille, *Chemistry of Materials*, 2015, **27**, 1210-1216.
90. J. Li, R. Lewis and J. Dahn, *Electrochemical and Solid-State Letters*, 2007, **10**, A17-A20.
91. S. Komaba, Y. Matsuura, T. Ishikawa, N. Yabuuchi, W. Murata and S. Kuze, *Electrochemistry Communications*, 2012, **21**, 65-68.
92. K. Dai, H. Zhao, Z. Wang, X. Song, V. Battaglia and G. Liu, *Journal of Power Sources*, 2014, **263**, 276-279.
93. J. Ming, H. Ming, W.-J. Kwak, C. Shin, J. Zheng and Y.-K. Sun, *Chemical Communications*, 2014, **50**, 13307-13310.
94. C.-Y. Chen, K. Matsumoto, T. Nohira, R. Hagiwara, A. Fukunaga, S. Sakai, K. Nitta and S. Inazawa, *J. Power Sources*, 2013, **237**, 52-57.
95. A. Bhide, J. Hofmann, A. K. Durr, J. Janek and P. Adelhelm, *Phys. Chem. Chem. Phys.*, 2014, **16**, 1987-1998.
96. Y. Liu, Y. Xu, Y. Zhu, J. N. Culver, C. A. Lundgren, K. Xu and C. Wang, *Acs Nano*, 2013, **7**, 3627-3634.
97. H. Lee, M. Yanilmaz, O. Toprakci, K. Fu and X. Zhang, *Energy & Environmental Science*, 2014, **7**, 3857-3886.
98. A. Basile, F. Makhlooghiazad, R. Yunis, D. R. MacFarlane, M. Forsyth and P. C. Howlett, *ChemElectroChem*, 2017, **4**, 986-991.
99. M. R. Palacin, *Chem. Soc. Rev.*, 2009, **38**, 2565-2575.
100. M. S. Whittingham, *Prog. Solid State Chem.*, 1978, **12**, 41-99.
101. K. Abraham, *Solid State Ionics*, 1982, **7**, 199-212.
102. S. P. Ong, V. L. Chevrier, G. Hautier, A. Jain, C. Moore, S. Kim, X. Ma and G. Ceder, *Energy Environ. Sci.*, 2011, **4**, 3680-3688.
103. D. Yuan, X. Liang, L. Wu, Y. Cao, X. Ai, J. Feng and H. Yang, *Adv. Mater.*, 2014, **26**, 6301-6306.
104. K. Park, D. Han, J. Shon, S. G. Doo and S. Lee, *RSC Advances*, 2015, **5**, 6340-6344.
105. M. Aryanpour, L. Miara and Y.-G. Ryu, *J. Electrochem. Soc.*, 2015, **162**, A511-A519.
106. L. Wang, J. Song, R. Qiao, L. A. Wray, M. A. Hossain, Y.-D. Chuang, W. Yang, Y. Lu, D. Evans and J.-J. Lee, *J. Am. Chem. Soc.*, 2015, **137**, 2548-2554.
107. J. Song, L. Wang, Y. Lu, J. Liu, B. Guo, P. Xiao, J.-J. Lee, X.-Q. Yang, G. Henkelman and J. B. Goodenough, *J. Am. Chem. Soc.*, 2015, **137**, 2658-2664.
108. C. Bommier, W. Luo, W.-Y. Gao, A. Greaney, S. Ma and X. Ji, *Carbon*, 2014, **76**, 165-174.
109. M. Nose, H. Nakayama, K. Nobuhara, H. Yamaguchi, S. Nakanishi and H. Iba, *J. Power Sources*, 2013, **234**, 175-179.
110. M. Nose, S. Shiotani, H. Nakayama, K. Nobuhara, S. Nakanishi and H. Iba,

- Electrochem. Commun.*, 2013, **34**, 266-269.
111. M. H. Han, E. Gonzalo, G. Singh and T. Rojo, *Energy & Environmental Science*, 2015, **8**, 81-102.
 112. H. Kim, J. Hong, K.-Y. Park, H. Kim, S.-W. Kim and K. Kang, *Chem. Rev.*, 2014, **114**, 11788-11827.
 113. G. G. Eshetu, S. Grugeon, H. Kim, S. Jeong, L. Wu, G. Gachot, S. Laruelle, M. Armand and S. Passerini, *ChemSusChem*, 2016, **9**, 462-471.
 114. N. Wongittharom, T.-C. Lee, C.-H. Wang, Y.-C. Wang and J.-K. Chang, *Journal of Materials Chemistry A*, 2014, **2**, 5655-5661.
 115. L. G. Chagas, D. Buchholz, L. Wu, B. Vortmann and S. Passerini, *J. Power Sources*, 2014, **247**, 377-383.
 116. N. Wongittharom, C.-H. Wang, Y.-C. Wang, C.-H. Yang and J.-K. Chang, *ACS applied materials & interfaces*, 2014, **6**, 17564-17570.
 117. C.-H. Wang, C.-H. Yang and J.-K. Chang, *Chem. Comm.*, 2016, **52**, 10890-10893.
 118. W.-X. Song, H.-S. Hou and X.-B. Ji, *Acta Phys.-Chim. Sin.*, 2017, **33**, 103-129.
 119. Y. Fang, J. Zhang, L. Xiao, X. Ai, Y. Cao and H. Yang, *Adv.Sci.*, 2017.
 120. C. Ding, T. Nohira, R. Hagiwara, A. Fukunaga, S. Sakai and K. Nitta, *Electrochim. Acta*, 2015, **176**, 344-349.
 121. A. Ponrouch, A. Goñi and M. R. Palacín, *Electrochem. Commun.*, 2013, **27**, 85-88.
 122. J. Barker, M. Saidi and J. Swoyer, *Electrochem. Solid-State Lett.*, 2003, **6**, A1-A4.
 123. X. Zhou and Y. G. Guo, *ChemElectroChem*, 2014, **1**, 83-86.
 124. G. Li, D. Jiang, H. Wang, X. Lan, H. Zhong and Y. Jiang, *J.Power Sources*, 2014, **265**, 325-334.
 125. A. Sequeiros, D. A. Gatto, J. Labidi and L. Serrano, *J. Biobased Mater. Bioenergy*, 2014, **8**, 370-376.
 126. B. L. Ellis and L. F. Nazar, *Curr. Opin. Solid State Mater. Sci.*, 2012, **16**, 168-177.
 127. A. Ponrouch, R. Dedryvère, D. Monti, A. E. Demet, J. M. Ateba Mba, L. Croguennec, C. Masquelier, P. Johansson and M. R. Palacín, *Energy Environ.Sci.*, 2013, **6**, 2361.
 128. M. Ue, in *Lithium-ion batteries*, Springer, 2009, pp. 75-115.
 129. R. McMillan, H. Slegr, Z. Shu and W. Wang, *J.Power Sources*, 1999, **81**, 20-26.
 130. K. Xu, *Chem. Rev.*, 2014, **114**, 11503-11618.
 131. K. Shiva, H. B. Rajendra and A. J. Bhattacharyya, *ChemPlusChem*, 2015, **80**, 516-521.
 132. K. Shiva, H. Rajendra, K. Subrahmanyam, A. J. Bhattacharyya and C. Rao, *Chem.Eur. J.*, 2012, **18**, 4489-4494.
 133. Y. Zhu, X. He and Y. Mo, *ACS. Appl. Mater. Interfaces*, 2015, **7**, 23685-23693.
 134. K. Xu, *Chem. Rev.*, 2004, **104**, 4303-4418.
 135. G. L. Xu, R. Amine, A. Abouimrane, H. Che, M. Dahbi, Z. F. Ma, I. Saadoune, J. Alami, W. L. Mattis and F. Pan, *Adv. Energy. Mater.*, 2018, **1702403**.
 136. K. Sato, L. Zhao, S. Okada and J.-i. Yamaki, *J.Power Sources*, 2011, **196**, 5617-5622.
 137. B. S. Lalia, N. Yoshimoto, M. Egashira and M. Morita, *J.Power Sources*, 2010, **195**, 7426-7431.
 138. S. Seki, Y. Kobayashi, H. Miyashiro, Y. Ohno, A. Usami, Y. Mita, N. Kihira, M. Watanabe and N. Terada, *J. Phys.Chem.Lett.*, 2006, **110**, 10228-10230.
 139. S. A. Mohd Noor, P. C. Howlett, D. R. MacFarlane and M. Forsyth, *Electrochim. Acta*, 2013, **114**, 766-771.
 140. M. W. Wagner, C. Liebenow and J. O. Besenhard, *J.Power Sources*, 1997, **68**, 328-332.
 141. N. Wongittharom, C. H. Wang, Y. C. Wang, C. H. Yang and J. K. Chang, *ACS. Appl. Mater. Interfaces*, 2014, **6**, 17564-17570.
 142. K. Matsumoto, R. Taniki, T. Nohira and R. Hagiwara, *J.Electro.Chem.Soc.*, 2015, **162**, A1409-A1414.

143. C. Ding, T. Nohira, K. Kuroda, R. Hagiwara, A. Fukunaga, S. Sakai, K. Nitta and S. Inazawa, *J.Power Sources*, 2013, **238**, 296-300.
144. M. Egashira, T. Asai, N. Yoshimoto and M. Morita, *Electrochim.Acta*, 2011, **58**, 95-98.
145. N. Wongittharom, T.-C. Lee, C.-H. Wang, Y.-C. Wang and J.-K. Chang, *J.Mater.Chem.A*, 2014, **2**, 5655.
146. K. B. Hueso, M. Armand and T. Rojo, *Energy Environ.Sci.*, 2013, **6**, 734.
147. S. Theivaprakasam, D. R. MacFarlane and S. Mitra, *Electrochim.Acta*, 2015, **180**, 737-745.
148. H. Li, Y. Bai, F. Wu, Y. Li and C. Wu, *J.Power Sources*, 2015, **273**, 784-792.
149. H. Wang, D. Jiang, Y. Zhang, G. Li, X. Lan, H. Zhong, Z. Zhang and Y. Jiang, *Electrochim.Acta*, 2015, **155**, 23-28.
150. D. Aurbach, B. Markovsky, G. Salitra, E. Markevich, Y. Talyossef, M. Koltypin, L. Nazar, B. Ellis and D. Kovacheva, *J.Power Sources*, 2007, **165**, 491-499.
151. S. Theivaprakasam, J. Wu, J. C. Pramudita, N. Sharma, D. R. Macfarlane and S. Mitra, *J.Phys.Chem. C*, 2017, **129**, 15630-15638.
152. A. K. R. C V Manohar, Mega Kar, Maria Forsyth, Doug R MacFarlane and Sagar Mitra, *Sustainable energy and fuels*, 2018, **2**, 566-576.
153. J. Xu, R. D. Deshpande, J. Pan, Y.-T. Cheng and V. S. Battaglia, *J.Electro.Chem.Soc.*, 2015, **162**, A2026-A2035.
154. J. Landesfeind, D. Pritzl and H. A. Gasteiger, *J.Electro.Chem.Soc*, 2017, **164**, A1773-A1783.
155. W. Li, A. Dolocan, H. C. Pilgun Oh, S. Park, J. Cho and A. Manthiram, *Nat. Commun.*, 2017, **8**.
156. S. Cull, J. Holbrey, V. Vargas-Mora, K. Seddon and G. Lye, *Biotechnol. Bioeng.*, 2000, **69**, 227-233.
157. G. Nagasubramanian and K. Fenton, *Electrochim.Acta*, 2013, **101**, 3-10.
158. V. Etacheri, R. Marom, R. Elazari, G. Salitra and D. Aurbach, *Energy Environ.Sci.*, 2011, **4**, 3243-3262.
159. S. W. Kim, D. H. Seo, X. Ma, G. Ceder and K. Kang, *Adv. Energy Mater.*, 2012, **2**, 710-721.
160. D. Monti, A. Ponrouch, M. R. Palacín and P. Johansson, *J. Power Sources*, 2016, **324**, 712-721.
161. W. Duan, Z. Zhu, H. Li, Z. Hu, K. Zhang, F. Cheng and J. Chen, *J.Mater.Chem.A*, 2014, **2**, 8668-8675.
162. H. Li, Y. Bai, F. Wu, Y. Li and C. Wu, *J. Power Sources*, 2015, **273**, 784-792.
163. J. Mao, C. Luo, T. Gao, X. Fan and C. Wang, *J. Mater. Chem. A*, 2015, **3**, 10378-10385.
164. H. Wang, D. Jiang, Y. Zhang, G. Li, X. Lan, H. Zhong, Z. Zhang and Y. Jiang, *Electrochim. Acta*, 2015, **155**, 23-28.
165. J. Yang, D.-W. Han, M. R. Jo, K. Song, Y.-I. Kim, S.-L. Chou, H.-K. Liu and Y.-M. Kang, *J. Mater. Chem. A*, 2015, **3**, 1005-1009.
166. X. Zhu, Y. Fang, X. Ai, H. Yang and Y. Cao, *J. Alloys Compd.*, 2015, **646**, 170-174.
167. K. Saravanan, C. W. Mason, A. Rudola, K. H. Wong and P. Balaya, *Adv. Energy Mater.*, 2013, **3**, 444-450.
168. J. Lee, Y. Lee, J. Lee, S.-M. Lee, J.-H. Choi, H. Kim, M.-S. Kwon, K. Kang, K. T. Lee and N.-S. Choi, *ACS Appl. Mater. Interfaces*, 2017.
169. J. Qian, W. A. Henderson, W. Xu, P. Bhattacharya, M. Engelhard, O. Borodin and J.-G. Zhang, *Nat. Commun.*, 2015, **6**.
170. J. Wang, Y. Yamada, K. Sodeyama, C. H. Chiang, Y. Tateyama and A. Yamada, *Nat. Commun.*, 2016, **7**.
171. Z. W. Seh, J. Sun, Y. Sun and Y. Cui, *ACS Cent. Sci.*, 2015, **1**, 449-455.

172. A. Bhide, J. Hofmann, A. K. Durr, J. Janek and P. Adelhelm, *Phys. Chem. Chem. Phys.*, 2014, **16**, 1987-1998.
173. S. Theivaprakasam, J. Wu, J. C. Pramudita, N. Sharma, D. R. Macfarlane and S. Mitra, *The Journal of Physical Chemistry C*, 2017, **129**, 15630-15638.
174. R.-S. Kühnel, N. Böckenfeld, S. Passerini, M. Winter and A. Balducci, *Electrochim. Acta*, 2011, **56**, 4092-4099.
175. S.-M. Oh, S.-T. Myung, C. S. Yoon, J. Lu, J. Hassoun, B. Scrosati, K. Amine and Y.-K. Sun, *Nano letters*, 2014, **14**, 1620-1626.
176. A. Bhide, J. Hofmann, A. K. Dürr, J. Janek and P. Adelhelm, *Phys. Chem. Chem. Phys.*, 2014, **16**, 1987-1998.
177. T. Nohira, T. Ishibashi and R. Hagiwara, *J. Power Sources*, 2012, **205**, 506-509.
178. A. Fukunaga, T. Nohira, Y. Kozawa, R. Hagiwara, S. Sakai, K. Nitta and S. Inazawa, *J. Power Sources*, 2012, **209**, 52-56.
179. R. Dugas, B. Zhang, P. Rozier and J. Tarascon, *J. Electrochem. Soc.*, 2016, **163**, A867-A874.
180. H. Wang, Y. Xiao, C. Sun, C. Lai and X. Ai, *RSC Advances*, 2015, **5**, 106519-106522.
181. Y. Li, S. Xu, X. Wu, J. Yu, Y. Wang, Y.-S. Hu, H. Li, L. Chen and X. Huang, *Journal of Materials Chemistry A*, 2015, **3**, 71-77.
182. K. Chihara, N. Chujo, A. Kitajou and S. Okada, *Electrochim. Acta*, 2013, **110**, 240-246.
183. M. Keller, C. Vaalma, D. Buchholz and S. Passerini, *ChemElectroChem*, 2016, **3**, 1124-1132.
184. S. Xu, Y. Wang, L. Ben, Y. Lyu, N. Song, Z. Yang, Y. Li, L. Mu, H. T. Yang and L. Gu, *Adv. Energy Mater.*, 2015, **5**.
185. D. Kim, E. Lee, M. Slater, W. Lu, S. Rood and C. S. Johnson, *Electrochem. Commun.*, 2012, **18**, 66-69.
186. H. Che, S. Chen, Y. Xie, H. Wang, K. Amine, X.-Z. Liao and Z.-F. Ma, *Energy & Environmental Science*, 2017, **10**, 1075-1101.
187. D. R. M. Manohar venkateswarlu Chinnareddy, Sagar Mitra, Maria Forsyth, Mega Kar and Anish K Raj *Sustainable energy and fuels*, 2018, DOI: 10.1039/C7SE00537G.
188. C.-Y. Chen, K. Matsumoto, T. Nohira and R. Hagiwara, *J. Electrochem. Soc.*, 2015, **162**, A176-A180.
189. M. Forsyth, H. Yoon, F. Chen, H. Zhu, D. R. MacFarlane, M. Armand and P. C. Howlett, *The Journal of Physical Chemistry C*, 2016, **120**, 4276-4286.
190. W. Ren, X. Yao, C. Niu, Z. Zheng, K. Zhao, Q. An, Q. Wei, M. Yan, L. Zhang and L. Mai, *Nano Energy*, 2016, **28**, 216-223.
191. K. C. Klavetter, S. Garcia, N. Dahal, J. L. Snider, J. P. de Souza, M. A. Cassara, A. Heller, S. M. Humphrey and C. B. Mullins, *Journal of Materials Chemistry A*, 2014, **2**, 14209-14221.
192. Y. Li, Z. Yang, S. Xu, L. Mu, L. Gu, Y. S. Hu, H. Li and L. Chen, *Advanced Science*, 2015, **2**.
193. L. Liang, Y. Xu, C. Wang, L. Wen, Y. Fang, Y. Mi, M. Zhou, H. Zhao and Y. Lei, *Energy & Environmental Science*, 2015, **8**, 2954-2962.
194. I. Hasa, X. Dou, D. Buchholz, Y. Shao-Horn, J. Hassoun, S. Passerini and B. Scrosati, *J. Power Sources*, 2016, **310**, 26-31.
195. Y. Wang, R. Xiao, Y.-S. Hu, M. Avdeev and L. Chen, *Nature communications*, 2015, **6**.
196. P. Han, X. Han, J. Yao, Z. Liu, X. Cao and G. Cui, *Electrochem. Commun.*, 2015, **61**, 84-88.
197. J. Ming, H. Ming, W. Yang, W.-J. Kwak, J.-B. Park, J. Zheng and Y.-K. Sun, *RSC Advances*, 2015, **5**, 8793-8800.
198. J.-K. Kim, Y. J. Lim, H. Kim, G.-B. Cho and Y. Kim, *Energy & Environmental Science*,

- 2015, **8**, 3589-3596.
199. A. Sarkar, S. Sarkar and S. Mitra, *J.Mater.Chem.A*, 2017, **5**, 24929-24941.
200. I. Hasa, S. Passerini and J. Hassoun, *J.Power Sources*, 2016, **303**, 203-207.
201. M. Forsyth, H. Yoon, F. Chen, H. Zhu, D. R. MacFarlane, M. Armand and P. C. Howlett, *J. Phys. Chem. C*, 2016, **120**, 4276-4286.
202. L. G. Chagas, D. Buchholz, L. Wu, B. Vortmann and S. Passerini, *J.Power Sources*, 2014, **247**, 377-383.
203. M. venkateswarlu Chinnareddy, M. Kar, T. Mendes, D. Wang, C. Xiao, M. Forsyth, S. Mitra and D. MacFarlane, *Chem.Comm*, 2018.
204. C. Bommier and X. Ji, *Small*, 2018, **14**, 1703576.
205. Z. Shadike, E. Zhao, Y. N. Zhou, X. Yu, Y. Yang, E. Hu, S. Bak, L. Gu and X. Q. Yang, *Adv. Energy Mater.*, 2018.
206. A. Guerfi, M. Dontigny, P. Charest, M. Petitclerc, M. Lagacé, A. Vijn and K. Zaghib, *J.Power Sources*, 2010, **195**, 845-852.
207. L. Lombardo, S. Brutti, M. A. Navarra, S. Panero and P. Reale, *J.Power Sources*, 2013, **227**, 8-14.
208. K. Kubota, T. Nohira and R. Hagiwara, *J. Chem. Eng. Data*, 2010, **55**, 3142-3146.
209. K. Kubota, T. Nohira, T. Goto and R. Hagiwara, *Electrochem. Commun.*, 2008, **10**, 1886-1888.
210. M. Forsyth, G. Girard, A. Basile, M. Hilder, D. MacFarlane, F. Chen and P. Howlett, *Electrochim.Acta*, 2016, **220**, 609-617.
211. M. Dahbi, N. Yabuuchi, K. Kubota, K. Tokiwa and S. Komaba, *Physical chemistry chemical physics : PCCP*, 2014, **16**, 15007-15028.
212. E. Yoo, J. Kim, E. Hosono, H.-s. Zhou, T. Kudo and I. Honma, *Nano Lett*, 2008, **8**, 2277-2282.
213. B. Jache and P. Adelhelm, *Angew. Chem. Int. Ed.*, 2014, **53**, 10169-10173.
214. Y. Wen, K. He, Y. Zhu, F. Han, Y. Xu, I. Matsuda, Y. Ishii, J. Cumings and C. Wang, *Nat. Commun.*, 2014, **5**, 4033.
215. R. Raccichini, A. Varzi, S. Passerini and B. Scrosati, *Nat Mater.*, 2015, **14**, 271.
216. E. Irisarri, A. Ponrouch and M. Palacin, *J. Electro.Chem. Soc*, 2015, **162**, A2476-A2482.
217. Y. Bai, Z. Wang, C. Wu, R. Xu, F. Wu, Y. Liu, H. Li, Y. Li, J. Lu and K. Amine, *ACS applied materials & interfaces*, 2015, **7**, 5598-5604.
218. J. Deng, M. Li and Y. Wang, *Green Chem.*, 2016, **18**, 4824-4854.
219. E. M. Lotfabad, J. Ding, K. Cui, A. Kohandehghan, W. P. Kalisvaart, M. Hazelton and D. Mitlin, *ACS Nano*, 2014, **8**, 7115-7129.
220. W. Lv, F. Wen, J. Xiang, J. Zhao, L. Li, L. Wang, Z. Liu and Y. Tian, *Electrochim.Acta*, 2015, **176**, 533-541.
221. L. Wu, D. Buchholz, C. Vaalma, G. A. Giffin and S. Passerini, *ChemElectroChem*, 2016, **3**, 292-298.
222. X. Zhu, X. Jiang, X. Liu, L. Xiao and Y. Cao, *Green Energy.Environ*, 2017, **2**, 310-315.
223. Y. Zheng, Y. Wang, Y. Lu, Y.-S. Hu and J. Li, *Nano Energy*, 2017, **39**, 489-498.
224. P. Wang, X. Zhu, Q. Wang, X. Xu, X. Zhou and J. Bao, *J.Mater.Chem.A*, 2017, **5**, 5761-5769.
225. J. Xiang, W. Lv, C. Mu, J. Zhao and B. Wang, *J Alloys Compd.*, 2017, **701**, 870-874.
226. X. Dou, I. Hasa, M. Hekmatfar, T. Diemant, R. J. Behm, D. Buchholz and S. Passerini, *ChemSusChem*, 2017, **10**, 2668-2676.

Publications:

1. C V Manohar, Anish Raj K, Mega Kar, Maria Forsyth, Douglas R. MacFarlane, Sagar Mitra, ***Stability enhancing ionic liquid hybrid electrolyte for NVP@C cathode based sodium batteries***, *Sustainable energy and fuels*, 2018, **2**, 566-576. (RSC publisher)
2. C V Manohar, Maria Forsyth, Douglas R. MacFarlane, Sagar Mitra, ***Role of N-Propyl- N-Methyl Pyrrolidinium bis(trifluoromethanesulfonyl)imide as an Electrolyte Additive in Sodium Battery Electrochemistry***, *Energy Technology (Wiley publisher)* (Accepted-2018).
3. C V Manohar, Tiago Correia Mendes, Mega Kar, Maria Forsyth, Sagar Mitra, Douglas R. MacFarlane ***Ionic liquid electrolytes supporting high energy density in sodium-ion batteries based sodium vanadium phosphate composites***, *Chem. Commun.*, 2018, **54**, 3500-3503. (RSC publisher)
4. C V Manohar, Tiago Correia Mendes, Mega Kar, Maria Forsyth, Sagar Mitra, Douglas R. MacFarlane, ***Ionic liquid added electrolytes improved the Physio-chemical properties and stabilizes the SEI layer on electrode materials in sodium batteries***, (Under the review).
5. C V Manohar, Tiago Correia Mendes, Mega Kar, Maria Forsyth, Sagar Mitra, Douglas R. MacFarlane, ***Commercial direction of Low cost full cell sodium ion battery based on almond shell based hard carbon with NVP@C electrode material***, (Under the review).

Conferences:

1. C V Manohar, Maria Forsyth, Douglas Macfarlane, Sagar Mitra, ***Ionic liquid as an additive in sodium ion battery and suppression the polarization loss of NVP/C cathode material***, Indo-US Workshop on Recent Advances in Multiscale, Multiphysics Analysis of Energy Conversion in Li-ion Batteries, IIT Bombay, Powai, Mumbai June9-11, 2016.

2. C V Manohar, Maria Forsyth, Douglas Macfarlane, Sagar Mitra, **NVP@C as a cathode material for hybrid electrolyte sodium batteries**, Nature conference, Shenzhen, China January 12-15,2018.

Awards:

*- Best Presenter award at the **Diamond Jubilee Energy Day 2018** organized by the Department of Energy science and Engg, IIT Bombay on 7th April 2018*

Acknowledgements

I would like to express my sincere gratitude to Prof. Douglas R Macfarlane and Prof. Sagar Mitra for the immeasurable amount of support and guidance he has provided throughout this study. I would also like to thank my research progress committee members Prof. Maria Forsyth and Prof. Ajay Panwar Singh who have given me support and provided me with much assistance and encouragement throughout my time. I thank my Monash collaborators Dr. Mega Kar, Dr. Vijay Ranganathan and Dr. Tiago C Mendes for their guidance and support of my ionic liquid and sodium ion battery full cell work. I would like to thank Dr. Katherine Nairn for her great support of my thesis proof reading and technical writing suggestions.

I would like to thank my seniors Dr. Sudeep Sarkar, Dr. Alok Mani Tripathi, Dr. Uttam Kumar Sen, Dr Pavan Srinivas, Dr Shivani Singh, Dr Sowmiya Theivaprakasam and my colleagues Ananta Sarkar, Divya Mahalakshmi, Md Furquan, Anish K Raj, Prasit Kumar Dutt, Ajit Kumar, Arnab Ghosh, Manas Ranjan Panda, Amlon Roy, Md Adil, Colin, Dabin wang, Changlong Xiao, Dr. Bryan, Dr. Zheng Ma, Dr. Diago Cabrial, Vilas Rao for their support and encouragement throughout my time.

I also would like to thank SAIF IIT Bombay, NCPRE-IIT Bombay for providing infrastructural and instrumental facilities to carry my research work.

I would like to thank IITB-Monash Research Academy for providing great collaboration work and infrastructure to pursue my research work at IIT Bombay and Monash University.

I am especially grateful to my family for encouraging me to follow my dreams and their support to make them a reality.

